Copyright

by

Jonghoon Baek

2006

The Dissertation Committee for Jonghoon Baek
Certifies that this is the approved version of the following dissertation:

FABRICATION AND CHARACTERIZATION OF THIN FILMS AND OPTICAL NANOCOMPOSITES

Committee:

____
Michael F. Becker, Supervisor

____
John W. Keto

____
Desiderio Kovar

____
Edward J. Powers

____
Gary A. Hallock

FABRICATION AND CHARACTERIZATION OF THIN FILMS AND OPTICAL NANOCOMPOSITES

by

JONGHOON BAEK, B.S.; M.S.

DISSERTATION

Presented to the Faculty of the Graduate School of
the University of Texas at Austin
in Partial Fulfillment
of the Requirements
for the Degree of
Doctor of Philosophy

The University Of Texas at Austin
May 2006

Dedication

To my parents and my wife

Acknowledgements

During my time at the University of Texas at Austin, I benefited from interactions with numerous individuals. I would like to thank my advisor Dr. Michael Becker for his inspiration. He gave me an incredible motivation, energy and the instruction about performing scientific research. Without his support, none of the works in this dissertation could be done. I am also thankful to Dr. Desiderio Kovar and Dr. John Keto for their support, advice and mentoring over the years. In many ways, they were my second advisors.

I appreciate the professional and personal support I received from my colleagues, both past and present. They are James Ma, Daniel T. O'Brien, Dr. William T. Nichols, Dr. Gokul Malyavanatham, Dr. Weijie Wang, Chong Huang, Changyi Lai, Andre Albert. They always encouraged and supported me.

I would like to thank my parents who have been my biggest champions throughout my life. They have given me unconditional love, support, and trust.

Last but not least, I am grateful to my wife Minhee for her self-sacrificing love for me.

FABRICATION AND CHARACTERIZATION OF THIN FILMS AND OPTICAL NANOCOMPOSITES

Publication No. __________

Jonghoon Baek, Ph.D.
The University of Texas at Austin, 2006

Supervisor: Michael F. Becker

Aluminum nitride thin films were fabricated and characterized using Pulsed Laser Deposition with varying processing conditions in order to exploit the feasibility as an encapsulating matrix for nonlinear nanocomposites. We have studied the dependence of optical properties, structural properties and their correlations for these AlN films. Low optical absorption, textured polycrystalline AlN films can be produced by PLD on sapphire substrates using a background nitrogen pressure of 4.5×10^{-4} Torr at 99.9% purity.

In order to accurately extract optical properties of non-uniform films, we have developed and successfully applied the Optimum Parameter Extraction (OPE) numerical method. The OPE method can accommodate films with two-dimensional thickness variation. Previous methods rendered significant errors in values of refractive index and film thickness when applied to absorbing and wedged films.

GaN nanocomposite coated with AlN film and silver nanocomposite coated with $NdAlO_3$ were successfully synthesized and their nonlinear optical properties were characterized by ultrafast laser. The enhancement of THG in GaN nanocomposite did not occur because the LAM process would change crystalline GaN feedstock into semi-amorphous GaN nanoparticles. The THG signal was enhanced in bare silver nanopaprticles due to the plasmon resonance. On the contrary, in the case of Ag NPs coated with $NdAlO_3$ the THG intensity was decreased by 40% at intermediate fields because the plasmon resonance wavelength was redshifted and moved off the two-photon resonance wavelength of the laser.

Table of Contents

List of Tables

List of Figures

1
Introduction

The general focus of this dissertation is the fabrication and characterization of thin films for optical nanocomposites. Nanometer-sized metal and semiconductor particles and their nanometer-sized composites exhibit truly unique, novel, and tunable properties that are nonexistent in their bulk counterparts because of the transition of material properties from the bulk to molecular-like clusters. For example, as a direct result of quantum confinement phenomena, nanosized semiconductor particles experience widening of their bandgap energy as the material dimension reduces. They also change their density of state function from continuous to discrete energy levels and cause blue shifts in optical spectra[1,2]. In addition, reductions in particle dimensions result in enhanced oscillator strength and shift the onset of absorption spectra towards higher energy. Besides the changes of the electronic structure, a large percentage of the atoms are on the surface. This enhanced surface to volume ratio also has a huge influence over physical and chemical properties of various materials.[3] Nanoparticle applications cover a wide range of areas. Specially, the enhancement of optical nonlinearity due to nanosized material can play a major role in the development of high speed data-processing and communication.

The synthesis and processing techniques of this fascinating class of materials has come a long way. Methods are now relatively well established for obtaining high quality mono-disperse nanocrystals of various different semiconducting and metallic materials. The next crucial step towards device fabrication is without a doubt the formation of nanomaterials into functional nanostructures without suppression of their unique properties. In order to make use of unprecedented physical and chemical characteristics of nanomaterials for optoelectronic and photonic devices, it may often be necessary to affix them on surfaces or arrange them in an organized network. The inherent advantage of nanosized materials can be augmented by combing two phases with distinct attributes, resulting in so-called nanocomposites. Such composites suited for important optical applications may be created by encapsulating nanoparticles of optically functional phases, in a processable matrix. The small particle size enhances the optical properties while the matrix material stabilizes and protects them. The properties of nanocomposites depend, with a reasonable approximation, on the linear combination of the individual characteristics of the two phases and are largely governed by the interfacial interactions between the two components. This design creates novel optical materials that do not occur naturally. Recent reports on nanocomposite systems have shown that the matrix materials not only act as a passive host in sustaining and protecting the nanocrystallites but also provide a special environment to the inclusion material.[4,5,6,7] For example, the change of the emission peak observed in the CdSe/$BaTiO_3$ composite system has been attributed to the dielectric environments effect of the matrix on the electronic structure of the embedded CdSe quantum dots. As optical nanocomposite applications are expanding, the need for novel functional and transparent matrixes increases. Fabrication of transparent matrices with embedded nanoparticles by various forms has become an important area in nanomaterials synthesis.

Semiconductor fabrication process will help develop new ways of creating create highly sensitive, accurate and practical nonocomposite devices in various applications. As such, thin films are of great interest as the final form of these novel materials.

The general principles in the construction of nanocomposites involve the intimate mixing of functional materials within a processable matrix. Matrix materials can be polymers, polymer blends, glasses, ceramics or semiconductors. Optical transparency is the one of the most important characteristic for optoelectronic and photonic applications because it is directly related to optical loss.

In this context, aluminum nitride (AlN) is an excellent material for making thin films of optical nanocomposites due to its unique properties. AlN has a wide band gap, 6.2 eV, and a small extinction coefficient which makes it ideal for the application in the ultra-violet (UV) domain. It also has a high surface acoustic velocity, large dielectric constant, high temperature stability. In addition, it is chemically inert and exhibits high hardness even at extreme temperature which makes it ideal for high power optoelectronic devices and insulating, wear-resistant coatings. AlN also is a strong potential candidate for use in the fabrication of blue light emitting diodes(LED) because it can be alloyed with GaN to create AlGaN based optical devices. The combination of these characteristics of AlN makes its thin film a suitable candidate for protective optical coatings and surface passivating layers of nanocomposite.

The main objective of this work has been to systematically fabricate and characterize thin films for high quality optical nanocomposites. We focused on the optical properties of the films such as extinction coefficient and refractive index because these are of practical importance for the enhancement of nonlinearity of nanocomposites. The extinction coefficient of a thin film is directly related to the optical device efficiency. Engineering of the refractive index and the extinction coefficient plays a key role in the enhancement of optical nonlinearity, especially in metal nanocomposites.[8] In order to explore the feasibility of thin films for nonlinear nanocomposites, semiconductor and metal nanocomposites were synthesized using a LAM process and PLD technique and their nonlinear properties were explored by high intensity laser excitation.

In this dissertation, a series of experiments were performed with the aim of elucidating the critical processing parameters that influence the crystal texture and optical properties of AlN films deposited by PLD (Pulsed Laser Deposition). To accurately determine optical properties of our wedged thin films, a novel numerical method was developed and successfully applied. However, all thin film samples fabricated by PLD in our lab have thickness variation and most of the published techniques and commercial thin film analyzing codes do not consider monotonic variations in thickness (wedge) or periodic non-uniformities in thickness (irregularities) that usually occur in thin films. The presence of thickness variations drastically changes data acquired by both ellipsometry and spectrophotometry and thus the analyses used for uniform smooth films are no longer valid because the interference structure of the spectra becomes quite distorted. This leads to significant errors in the derived determination of optical constants measured using these methods. In order to accurately extract optical properties of non-uniform films, a novel numerical method and efficient constitutive relations were developed that can determine film properties from just the transmission spectrum. This Optimum Parameter Extraction (OPE) method was applied and accurate optical information of our thin films were successfully extracted. In addition, the dependence of AlN thin film quality and their characteristics as a function of various processing parameters were investigated.

The LAM process and PLD techniques were used to synthesize optical nanocomposites. A gallium nitride nanocomposite coated by an AlN film and a silver nanocomposite coated by a $NdAlO_3$ film were synthesized and their nonlinear properties such as second harmonic generation (SHG) and third harmonic generation (THG) were characterized by ultra fast laser excitation.

The organization of this dissertation is as follows. The nanocopmosites fabrication methods, LAM and PLD, are summarized in chapter 2. In the LAM section, we discuss the generation of microparticle aerosols and their ablation in two separate chambers: the electrostatic cell and the supersonic cell. In the second section, PLD methods for fabricating single thin films and nanocomposite coatings are described. Chapter 3 describes the OPE method which was developed by our group. This discussion includes theoretical background of the OPE method, the simulation results from application to various model thin film systems and experimental results of actual AlN films fabricated in our lab by PLD. The goal for this method is to accurately determine optical information from the thin films even when the films exhibit absorption and thickness variations. Correlations between optical properties, microstructure, and processing conditions of AlN thin films fabricated by PLD are then discussed in chapter 4. Here, we aim to elucidate the critical processing parameters that influence the crystal texture and optical properties of AlN films deposited by PLD. Films have been deposited by varying processing parameters including laser fluence, substrate temperature, and gas pressure. The films were then examined using various characterization techniques such as scanning electron microscopy, x-ray diffraction, atomic force microscopy (AFM), mechanical profilametry and UV-VIS spectroscopy. Chapter 5 addresses optical nonlinearity such as second harmonic generation (SHG) and third harmonic generation (THG) of GaN and Ag nanocomposites.

---

[1] A A Seraphin, E. Werwa and K. D. Kolenbrander , J. Mater. Res. **12,** 3386 (1997)

[2] C. B. Murray, D. J. Norris and M. G. Bawendi , J. Am. Chem.Soc. **115,** 8706 (1993)

[3] G.M. Whitesides, J.P. Mathias, C.T. Seto. Science **254**,1312 (1991)

[4] M. Fujii,A. Mimura, S. Hayashi, K. Yamamoto. Appl. Phys.Lett., **75**, 184 (1999)

[5] S.K. Bera, S. Chaudhuri, A. K. Pal, J. Phys. D: Appl. Phys., **33**, 2326 (2000)

[6] J. Zhou; L. Li, Z. Gui, S. Buddhudu, Y. Zhou, Appl. Phys. Lett., **76**, 1540 (2000)

[7] C.M Bender, J. M. Burtlich, D. Barber, C. Pollock, Chem. Mater., **12**, 1969 (2000)

[8] C. Bohren and D. Huffmann, *Absorption and Scattering of Light by Small Particles* (John Wiley, New-York, 1983).

2

Laser Ablation of Microparticles process and Pulsed Laser Deposition

In order to synthesize efficient nonlinear optical nanocomposites, two material phases are necessary; nonlinear nanoparticles and functional transparent thin films encapsulating them without suppression or with enhancement of their nonlinear properties. In first part of this chapter, we describe the methods for obtaining high quality mono-disperse nanoparticles of various semiconducting and metallic materials using a laser ablation process named Laser Ablation of Microparticles (LAM). The next step towards synthesizing nanocomposites is the formation of nanomaterials into the encapsulating layer. Pulsed laser deposition (PLD) was chosen for this purpose due to its many unique advantages. The principles and advantages of the LAM process and the PLD technique will be discussed in detail in this chapter.

2.1 Laser Ablation of Microparticles (LAM)

Over the past twenty years, extensive research has been carried out to synthesize nanoparticles. Synthesis methods include: gas evaporation, colloidal processing, mechanical attrition, and laser ablation. Each method has its own advantages and disadvantages. In order to take full advantage of the unique properties of nanoparticles for further application, pure nanoparticles are required. Most of other nanoparticle formation methods involve chemical reagents in solution. On the other hand, the laser ablation technique uses no chemical reagents in solutions. The only components in the laser ablation process are the feedstock and the inert buffer gas. Laser ablation has other advantages such as 1) preservation of stoichiometry 2) a wide variety of materials amenable to ablation. Also many types of materials such as metals, semiconductors, ceramics, magnetic and nonmagnetic alloys can be synthesized with the same apparatus. 3) In addition, this method is capable of both in situ and ex situ processing of the nanoparticles. Laser ablation was chosen as our synthesis method due to the reasons above.

Laser ablation has been long established as a technique for offering unique characteristics in both research and industry. Very early it was realized that high laser intensities result in unique interactions with material. The ablation mechanism by high intensity lasers is significantly different when compared to thermal mechanisms such as melting, evaporation or boiling. It was found that above a critical laser intensity a plasma breakdown is initiated. The resulting shock wave is strong enough to vaporize the entire particle.[1,2] In the low pressure region behind the shock wave, conditions are favorable for the nucleation and growth of small (nanometer-sized) particles. This technique can be used to produce nanoparticles from virtually any material that can be made into micron sized particles. If the microparticles are entrained as an aerosol prior to ablation, the nanoparticle production is a continuous process making it a potentially attractive industrial process for mass production of nanoparticles. This idea was demonstrated at the University of Texas at Austin by Becker et al.[3] and this process was named the Laser Ablation of Microparticles (LAM) process. Thereafter, the Laser Ablation of Microparticles (LAM) process has been used to prepare nanoparticles from various materials such as metals, ceramics, and semiconductors.[4,5] This technique of nanoparticle production coupled with two types of collection mechanisms for nanoparticles, discussed in detail in next section, has significant applications in materials processing. Collection of nanoparticles, either as dispersions in surfactants or as thin deposited films, provides flexibility to the LAM process to access a wide range of applications.

Although the LAM process looks similar to the flat target laser ablation, it is different in a number of aspects. First of all, for a given material, a decreased threshold for plasma formation is observed when the material is in microparticulate form. In addition, because the volume of a microparticle is substantially less than that of a solid surface, a concentration of shock-wave heating occurs. In the LAM process, plane waves from a laser irradiate individual microparticles which are suspended in an aerosol. The ablation process for a single microparticle is shown schematically in figure 2.1. The ultraviolet laser rapidly heats and ionizes the microparticle until the breakdown threshold is exceeded. Breakdown is initiated near the front edge of the microparticle. A shock wave, which burns its way through the particle, is launched from the point of breakdown. Observation and simulation both suggest that the traveling shock wave compresses and heats the feedstock material far above its critical point[6]. Condensation occurs rapidly in a low pressure region directly behind the shock wave. The material coalesces quickly and condenses into nanoparticles. Depending on process conditions, e.g. laser fluence, initial feedstock microparticle size, and background gas pressure, nanoparticles of metals, (silver, gold, copper and tungsten), semiconductors (silicon, cadmium selenide, gallium nitride) and dielectrics (tungsten carbide, SiO_2) have been successfully synthesized and studied extensively by this method”[7]. Nanoparticles of metals and semiconductor synthesized using this method have been shown to have mean diameters in the 5-100 nm range and narrow size distributions.

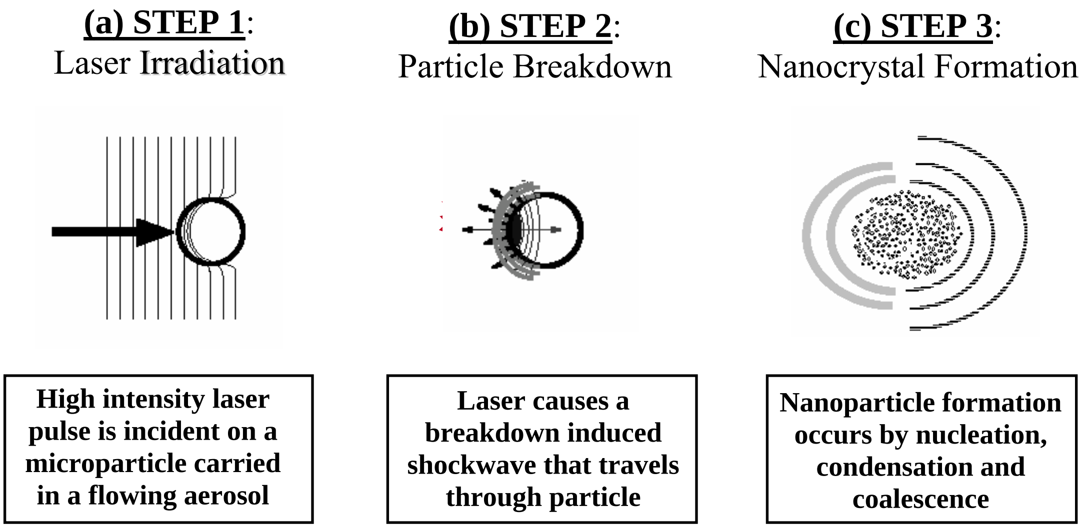

Figure 2.1 A simplified illustration of the different stages of silver microparticle breakdown after laser irradiation. (a) plane wave illumination and skin depth absorption (b) plasma explosion at front surface and the launching of a shockwave through the particle (c) expansion of initially evaporated material from the front of the microparticle, nanoparticle condensation behind the shockwave, and exit of shock from initial particle.

2.2 Nanoparticle collection

Collection of aerosolized nanoparticles is another research area. This is not an easy task because they have such small mass and large surface area, the gas around them appears very viscous and the nanoparticles tend to follow gas stream lines around objects. Gravity has a negligible effect on the motion of the nanoparticles because the drag force of the gas is much greater.

Two different collection schemes were employed for the collection of nanoparticles; electrostatic collection of the highly charged nanoparticles and virtual impactor collection were developed in our group. As the title indicates, the collection principles of two systems are quite different from each other. Each method has its own advantages. The electrostatic cell has two advantages. First, it has the capability to size select the nanoparticles in situ for subsequent supersonic deposition (Nichols et al., 2001). Second, it provides a more sensitive control of the nanoparticle density for use in nanocomposites. On the other hand, the collection efficiency of virtual impactors has been shown to be much better than that of the electrostatic because it takes advantage of the difference of the inertia between nanoparticles and microparticles. The trade-off is that there is no size selection.

2.2.1 Electrostatic collection

The electrostatic collection system takes advantage of the charging effect to collect the nanoparticles. Fig 2.2 shows a cross section of the electrostatic cell used for collection of nanoparticles. Our group found that metal nanoparticles generated by the LAM process were electrically charged as a result of ejection of electrons from within a skin depth (~ few micro meters) by single or multi photon photonization. Electrons not ejected spread out their excess energy as heat through electron-electron and electron-phonon scattering. Since the quantum efficiency for photoelectron production in metals is of the order of 10^{-4}, only a very small fraction of electrons are emitted as photoelectrons. Hot nanoparticles also lose electrons by thermionic emission. Hence nanoparticles are photoionized and thermally ionized during their formation. The resulting charged nanoparticle stream remains unagglomerated and is collected electrostatically using a static electric field. By taking advantage of this charged particle phenomenon, narrowly distributed nanoparticles collection was demonstrated by exposing them to an electric field that is perpendicular to the flow of the aerosol flow. The electric field was adjusted by biasing two electrodes with a 300 - 1000 V potential difference.

As mentioned above, using the electrostatic cell has two advantages; size-selectivity and a more sensitive control of the density of nanoparticles for use in nanocomposites. For the synthesis of GaN nanoparticles, the electrostatic cell was used because a large nonlinear optical susceptibility enhancement in semiconductor nanoparticles will be expected only in the case of an extremely narrow size distribution.[8]

A visible experiment verifying the charging nanoparticles was successfully conducted by Henneke[9]. A He-Ne laser (633nm) beam was used to illuminate silver microparticles as they were ablated. By using a He-Ne bandpass filter on a digital camcorder, a video of the ablation and electrostatic collection process was obtained. The voltage was varied between 0 to 2,000 volts. As the voltage was increased, the curvature of the aerosol stream increased. Comparing video frames taken at different field strengths, the difference of curvature was clearly observed between 0 V, 1000 V, 2000 V. The deflected stream is composed of charged nanoparticles and microparticles affected by turbulence in hydrodynamic flow. A typical figure showing deflection of the aerosol stream after breakdown in a 2000V electric field is shown in Fig 2.3.

The charging of semiconductor nanoparticles using the electrostatic cell is different from silver metal nanoparticles and this was extensively studied by Nichols (2002) [10]. From his study, it was seen that semiconductor nanoparticles forms with a bi-polar charge. This is in contrast with silver which was found to be strictly positively charged. Oppositely charged particles result in significant chaining of semiconductor nanoparticles under most operating conditions. Chaining was found to be reduced when turbulence is minimized through low microparticle density and low collection voltage.

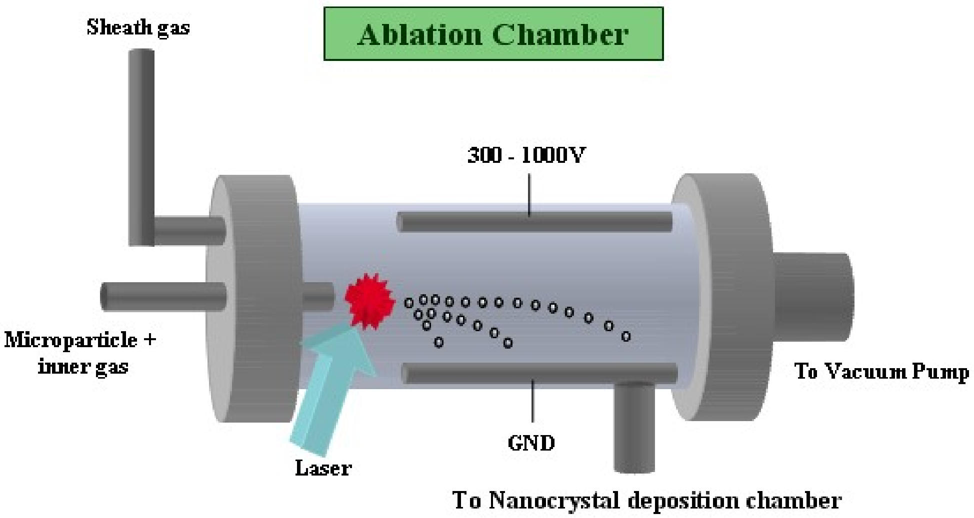

Figure 2.2 Schematic of the electrostatic cell.

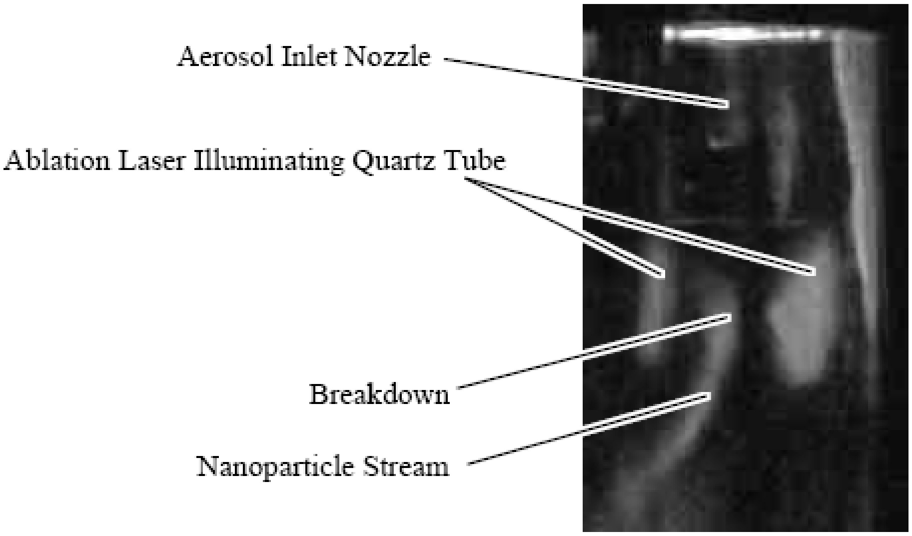

Figure 2.3 Deflection of aerosol stream after breakdown on application of electric field, voltage set to 2000 Volts.

2.2.2 Virtual impactor collection

Although the gas velocity and the number of microparticles in the aerosol stream are adjusted so that all of the microparticles should be ablated, there will always be some microparticles which were unablated. To make pure nanocomposites, microparticles should be removed and only nano-sized materials should be deposited on the substrate. The concept to sort nanoparticles from microparticles in an aerosol is a relatively simple one. The difference of the inertia between nanoparticles and micorparticles is so large that it causes the unablated particles to cross the gas streamlines and strike an virtual impactor. Here, a virtual impactor is used as a stagnant gas region to collect large microparticles. In contrast, nanoparticles tend to stay in the gas flow and be deposited on the substrate. The general system is shown schematically in Fig. 2.4. The ablated nanoparticles in the stream are drawn away from the flow axis into the collection chamber while the heavier partially ablated and unablated microparticles (≥300 nm) diverge from the axis less strongly and are collected inside of the virtual impactor and removed to microparticle outlet. The collection efficiency of virtual impactors has been shown to be strongly dependent on the density of the material being ablated and weakly dependent on the gas type by Henneke et al. Another advantage of the virtual impactor is that it can be operated without build-up of material and hence the nanoparticle generator can be operated over longer periods. Therefore, to make thick nanoparticle dispersions or films, the virtual impactor collecting system is more appropriate than the electrostatic system if narrowly distributed nanoparticles are not essential.

For the synthesis of silver nanoparticles, the virtual impactor collection system was used because size-selectivity appears to be relatively less important for the enhancement of the nonlinearity in metal nanoparticles.

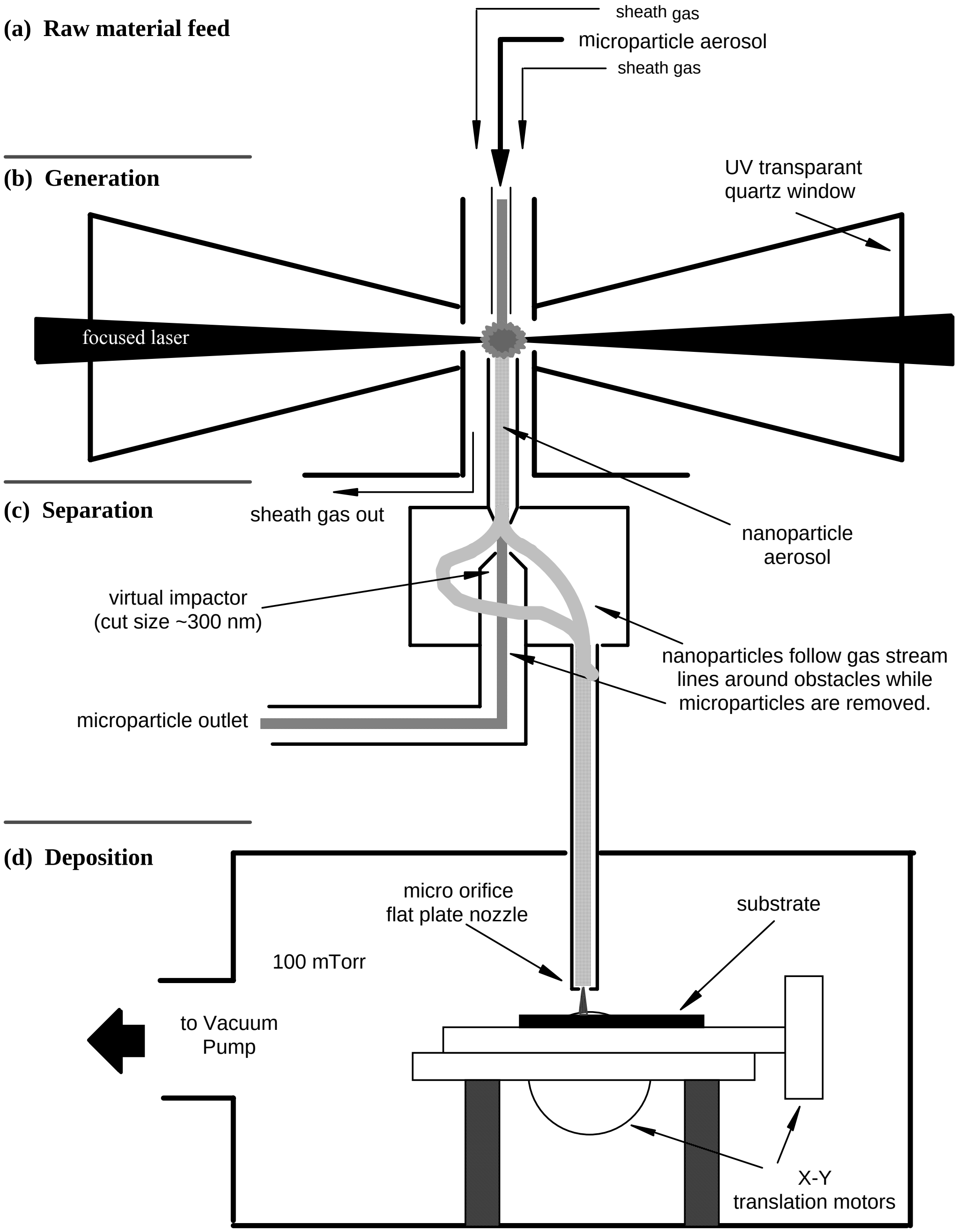

Figure 2.4 Schematic of the LAM system for nanoparticle production and deposition of nanoparticulate films.[11]

2.3 Pulse Laser Deposition

There are many material growth techniques. Physical vapor deposition of thin films takes many experimental forms. Pulsed laser deposition is often used as the method of synthesis for nanocomposites due to its success in depositing materials of complex stoichiometry. For example, AlN thin films are extremely absorptive when the stoichiometry is broken[12]. In other words, nitrogen deficiency degrades the AlN film transparency, and it cannot be used as the encapsulating layer for optical devices. The transparency of $NdAlO_3$ is guaranteed only when oxygen deficiency does not occur. In this context, PLD is the most appropriate technique for encapsulating nanoparticles into nanocomposites without suppression or with enhancement of their nonlinear optical properties.

Although the actual physical processes of material removal are quite complex, PLD is a conceptually simple technique, probably the simplest among all thin film growth techniques. It consists of a target holder and a substrate holder housed in a vacuum chamber. A laser beam vaporizes a target surface, producing a film with the same composition as the target. PLD was the first technique used to successfully deposit a superconducting $YBa_2Cu_3O_7$ thin film[13]. Since that time, many materials that are normally difficult to deposit by other methods, especially multi-element oxides, have been successfully deposited by PLD. Besides being a straight forward process, the main advantage of PLD derives from the laser material removal mechanism. PLD relies on a photon interaction to create and eject plumes of material from a target. The vapor (plume) is collected on a substrate placed a short distance from the target. Unlike thermal evaporation, which produces a vapor composition dependent on the vapor pressures of different elements in the target material, the laser-induced expulsion produces a plume of material with stoichiometry similar to the target. It is generally easier to obtain the desired film stoichiometry for multi-element materials e.g. high-temperature superconductors, piezoelectric and ferroelectric materials with perovskite structure using PLD than with other many deposition technologies. Stoichiometry transfer between target and substrate is not easy with evaporation or (magnetron) sputtering because in general the partial vapor pressures and sputtering yields of the components are different from each other. This causes a different composition of the thin film on the substrate. However, in the case of PLD, the quick and intense heating of the target surface by the high energy laser (typically up to temperatures of more than 5000 K within a few ns) ensures that all target material components irrespective of their partial binding energies evaporate at the same rate. When the ablation rate is sufficiently high (which normally is the case at laser fluences well above the breakdown threshold), a so-called Knudsen layer is formed.[14] Further heating creates a high-temperature plasma[15] , which then adiabatically expands in a direction perpendicular to the target surface. Consequently, during PLD, the material transfer between target and substrate occurs in a material package, where the separation of the species is relatively small. Additionally, PLD is considered to have other advantages; 1) The energy of the ablated species may enhance the quality of film growth; 2) PLD is highly pure. It does not require hot filaments that increase the partial pressure of reactive gases in the chamber during deposition. 3) Versatile. Many different materials can be deposited with a wide variety of gases over a broad range of gas pressures. 4) Cost-effective. One laser can serve many vacuum systems. 5) Film growth is fast. High quality samples can be grown reliably in 10 or 15 minutes 6) PLD can be done on small targets. Preparing samples for research purposes or for application tests, even when the sample is one component, can be extremely expensive or difficult to prepare with other techniques.

The principle of pulsed laser deposition, in contrast to the simplicity of the system set-up, is a very complex physical phenomenon. It involves the physical process of the laser-material interaction from high-power pulsed radiation on a solid target, the formation plasma plume dynamics with high energetic species and the transfer of the ablated material through the plasma plume onto the heated substrate surface.

Using the PLD as described in chapter 4, we have deposited AlN films with varying conditions on sapphire substrates to perform a series of experiments aimed at elucidating the critical processing parameters that influence the optical properties, crystal texture, and their correlation. In addition, we synthesized semiconductor and metal nanocomposites by depositing highly efficient and transparent AlN coatings on GaN nanoparticles and $AlNdO_3$ coatings on silver nanoparticles to exploit the their feasibility for nonlinear nanocomposites such as second harmonic generation (SHG) and third harmonic generation (THG). This will be described in chapter 5.

---

[1] J.C. Carls and J.R. Brock , Opt. Lett., **13**, 273 (1988).

[2] J.C. Carls. and J.R. Brock, Opt. Lett., **13**, 919 (1988).

[3] M. F. Becker, J.R. Brock & J.W. Keto, U.S. Patent No. 5,585,020. (1996).

[4] W.T. Nichols , G. Malyavanatham, D.E. Henneke, J.R. Brock, M.F. Becker, J.W. Keto and H.D. Glicksman, J. Nanoparticle Res. **2**, 141 (2000).

[5] W.T. Nichols, J.W. Keto, D.E. Henneke, J.R. Brock, G. Malyavanatham, M.F. Becker and H.D. Glicksman, Appl. Phys. Lett, **78**, 1128 (2001).

[6] J. Lee, M. F. Becker, J. W. Keto, J. Appl. Phys., **89**, 8146 (2001).

[7] W. T. Nichols, G. Malyavanatham, D. E. Henneke, J. R. Brock, M. F. Becker, J. W. Keto, J. Nanoparticle Research, **4**, 423 (2002).

[8] L Banyai, Y. Z. Hu, M. Lindberg and S. W. Koch, Phys. Rev. B **38**, 8142 (1988)

[9] D.E. Henneke. “Nanoparticles produced via laser ablation of microparticles” Dissertation, The University of Texas at Austin (2001).

[10] W. T. Nichols, “Production and controlled collection of nanoparticles; toward manufacturing of nanostructured materials” Dissertation, The University of Texas at Austin (2002).

[11] D. T. O’Brien, “Deposition and Characterization of Nanostructured Silver Thick Films”, Thesis, The University of Texas at Austin (2003).

---

[12] C. Ristoscu, I. N. Mihailescu, M. Velegrakis, M. Massaouti, A. Klini, and C. Fotakis, J. Appl. Phys. **4**, 2244 (2003).

[13] D. Dijkkamp, T. Venkatesan, X. D.Wu, S . A. S hareen, N. Jiswari, Y. H. Min-Lee, W. L. McLean, and M. Croft, Appl. Phys. Lett. **51**, 619 (1987).

[14] R. Kelly, and J. E. Rothenberg, Nucl. Instrum. Methods Phys. Res. B **7/8**, 755 (1985).

[15] C. R. Phipps, T. P. Turner, R. F. Harrison, G. W. York, W. S. Osborne, G. K. Anderson, X. F. Corlis,, L. C. Haynes, H. S. Steele, K. C. Spicochi, and T. R. King, J. Appl. Phys. **64**, 1083 (1988)

3

Optimum Parameter Extraction Method

3.1 Motivation

Thin films are widely used to improve the performance of optical components and to form optical waveguides for integrated optics. They also are used in various applications in semiconductor components. As mentioned in chapter 1, thin films are important for the performance of nanocomposites not only as passive host in sustaining and protecting the nanocrystallites but also in providing a special environment for the inclusion material.[1,2,3,4] Especially, for nonlinear applications, it is important to characterize the films' accurate optical constants (the refractive index, n, and the extinction coefficient, k), and to determine their thickness, d, since the refractive index is a function of dielectric constant and the dielectric constant of a thin film is directly correlated to the enhancement of nonlinearity.[5,6,7] Extinction coefficient is a critical factor for the efficiency of optical components and optical waveguides for integrated optics. In physics and engineering accurate determination of the values of the wavelength-dependent optical constants is also very useful because it gives fundamental information about the optical band gap, defect levels, oscillator energy and oscillator strength, etc. Moreover, optical constants are believed to be strongly correlated to the film microstructure so that it is possible to ascertain information about film microstructure by investigating optical properties.[8,9,10]

Various methods have been employed for determining the real and imaginary parts of the refractive index. They can be classified into two general categories:

(1) Virtual calculation of transmission (or reflection) spectra based on spectral envelopes[11]

(2) Fitting (optimization) methods using parameterized dispersion relations[12,13]

Spectral envelope methods determine film parameters from functions describing the locus of interference maxima and minima in the transmittance or reflectance spectrum. On the other hand, optimization methods use the full spectral interference pattern to fit an exact, but parameterized, model to the data.

Regrettably, as introduced in chapter 2, the films by PLD tend to have a lack of uniformity over a large area due to a narrow angular distribution of the plume. Our group used an eccentric rotating lens to direct each pulse to a fresh location on a 1.5 mm by 3 mm oval so as to achieve as consistent ablation as possible. However, it increased the non-uniformity of the films, which was verified by mechanical profilametry. Most of the published literature does not consider the wedge and non-uniformity in thickness of the films that occur in many practical instances. The presence of thickness variations can drastically distort the transmission spectra, and thus the formulae used for uniform smooth films are no longer valid. In general as thickness variations increase, visibility of the interference fringes is decreased, i.e. the transmission maxima decrease and the transmission minima increase, and the envelope of the spectrum shrinks. The determination of optical constants using conventional methods results in an overestimate of the thickness and an erroneous refractive index dispersion, especially in the short-wavelength region of the spectrum[14].

Marquez et al.[15,16] have developed and applied a physically appealing procedure first proposed by Swanepoel to calculate the average thickness, thickness variation, refractive index, and extinction coefficient of wedge-shaped films. (From now on we refer to this method as the wedge-shaped envelope method.) Unfortunately, this method suffers from a critical disadvantage: it assumes that the film is transparent in the long-wavelength region, which is not true in many cases. One would expect that the error resulting from this assumption would increase as the extinction coefficient of the film increases. This will be verified in section 3.3.2.1.

In this chapter, a novel, physically attractive and simple numerical method that considers non-uniformity in thickness of the film is presented. The method is based on Swanepoel's calculation of wedged film transmission through a finite aperture, but utilizes a fitting method so that it can be applied accurately to absorptive and wedged films. Our Optimum Parameter Extraction (OPE) method allows the calculation of film thickness, thickness variation, refractive index, and extinction coefficient from only a transmission spectrum. We also obtain optical constants using the wedge-shaped envelope method and the conventional envelope method for comparison, and the differences are discussed. We compare results for test cases and for actual AlN thin films fabricated in our laboratory. The AlN thin films were deposited on sapphire (0001) substrates using PLD (Pulsed Laser Deposition) at different temperatures and laser fluences.

3.2 Overview of theoretical background

In this section, the film on substrate system is investigated from first principles and exact numerical expressions for the transmittance and reflectance of various situations are presented without any approximation.

3.2.1 Transmission by an ambient-film-substrate system

The general case of an absorbing film with thickness d_1 on an absorbing substrate with thickness d_2 is shown in Fig 3.1. It is assumed that both film and substrate are uniform (i.e. no thickness variation), homogeneous and isotropic. The system is surrounded by air with a refractive index, $n_0 = 1$. We start by assuming normal incidence ($\Phi_0 = \Phi_1 = \Phi_2 = 0$). All formulae will be generalized to the case of oblique incidence with substitutions of some equations. However, it will not be described in this work.

Each layer is characterized by its complex refractive index. The film layer has a uniform thickness, d_1, refractive index, n_1, and extinction coefficient, k_1 (complex refractive index, $\widetilde{n}_1 = n_1 - ik_1$), and the substrate layer has a uniform thickness, d_2, refractive index, n_2, and extinction coefficient, k_2 (complex refractive index, $\widetilde{n}_2 = n_2 - ik_2$).

Before acquiring a specific transmission and reflection of the two-layer system shown in Fig. 3.1, finding a generalized transmission and reflection expression is more valuable because the two-layer system is the subset of this general expression.

The overall transmission and reflection properties of a multiple stratified structure are represented by a complex **scattering matrix S**[17] which is expressed as a product of interface matrices (I) and layer matrices (L), taken in the proper order, as follows:

$$S = \boldsymbol{I}_{01}\boldsymbol{L}_1\boldsymbol{I}_{12}\boldsymbol{L}_2\ldots\boldsymbol{I}_{(i-1)}\boldsymbol{L}_j\ldots\boldsymbol{L}_m\boldsymbol{I}_{m(m+1)} \tag{3.1}$$

Where,

$$I_{ab} = \begin{pmatrix} 1/\widetilde{\tau}_{ab} & \widetilde{r}_{ab}/\widetilde{\tau}_{ab} \\ \widetilde{r}_{ab}/\widetilde{\tau}_{ab} & 1/\widetilde{\tau}_{ab} \end{pmatrix} = \left(\frac{1}{\widetilde{\tau}_{ab}}\right)\begin{pmatrix} 1 & \widetilde{r}_{ab} \\ \widetilde{r}_{ab} & 1 \end{pmatrix},$$

$$(3.2)$$

$$L_a = \begin{pmatrix} e^{j\widetilde{\beta}_a} & 0 \\ 0 & e^{-j\widetilde{\beta}_a} \end{pmatrix},$$

$$\widetilde{r}_{ab} = \frac{\widetilde{n}_a - \widetilde{n}_b}{\widetilde{n}_a + \widetilde{n}_b} = r_{ab} + ir'_{ab},$$

$$r_{ab} = \frac{({n_a}^2 - {n_b}^2) + ({k_a}^2 - {k_b}^2)}{(n_a + n_b)^2 + (k_a + k_b)^2},$$

$$r'_{ab} = \frac{2(n_a k_b - n_b k_a)}{(n_a + n_b)^2 + (k_a + k_b)^2},$$

$$\tilde{\tau}_{ab} = 1 + \tilde{r}_{ab}$$

$$\tilde{\beta}_b = \frac{\varphi_b}{2} - i\frac{\alpha_b d_b}{2},$$
$$\varphi_b = 4\pi n_b d_b / \lambda,$$
$$\chi_b = \exp(-\alpha_b d_b),$$
$$\alpha_b = 4\pi k_b / \lambda$$

In the last second line, χ_b will be referred to as “film transmittance” since it is the internal transmittance of the film.[18]

The transmission, T_{italic} and reflection, R_{italic} are now given by

$$T_{italic} = \left|\frac{1}{S_{11}}\right|^2, \tag{3.3}$$

$$R_{italic} = \left|\frac{S_{12}}{S_{11}}\right|^2. \tag{3.4}$$

The more specific derived processes are described in the book “Ellipsometry and Polarized Light”(North-Holland Publishing Co., 1977) by Azzam et al.

Accordingly, for the two-layer system shown in Fig. 3.1, the scattering matrix is

$$S = [\frac{1}{(1+\tilde{r}_{01})(1+\tilde{r}_{12})(1+\tilde{r}_{20})}]\begin{pmatrix} 1 & \tilde{r}_{01} \\ \tilde{r}_{01} & 1 \end{pmatrix}\begin{pmatrix} e^{j\tilde{\beta}_1} & 0 \\ 0 & e^{-j\tilde{\beta}_1} \end{pmatrix}\begin{pmatrix} 1 & \tilde{r}_{12} \\ \tilde{r}_{12} & 1 \end{pmatrix} \times \begin{pmatrix} e^{j\tilde{\beta}_2} & 0 \\ 0 & e^{-j\tilde{\beta}_2} \end{pmatrix}\begin{pmatrix} 1 & \tilde{r}_{20} \\ \tilde{r}_{20} & 1 \end{pmatrix} \tag{3.5}$$

The values of T_{italic} and R_{italic} can be computed numerically from eq (3.3) and eq (3.4). However, they do not seem to be practical expressions because transmittance and reflectance from eq (3.3) and eq (3.4) are not likely to be matched with the experimentally measured data due to the imperfect monochromatic light source. The distance between two neighboring extrema (i.e between two consecutive maxima and minima) of the transmission or/and reflection spectrum of the interference pattern by a thick substrate is $\Delta\lambda_e \sim \lambda/(4st)$, where s is the refractive index of substrate and t is thickness of the substrate. The typical thickness of the substrate is ~ 1 mm which results in $\Delta\lambda_e << 1$nm. However, most of the spectrophotometer radiation is not perfectly monochromatic, having, instead, an energetic distribution with a spectral half-width $\Delta\lambda$ (typically, ~1nm), around the mean wavelength λ. That means that the spectrophotometer cannot resolve the interference fringes of the spectrum. This lack of interference resolution is mathematically performed as an integration of transmittance and/or reflectance over substrate phase φ_2 in equations (3.3) and (3.4). This method is exactly applicable for the case of a non-uniform substrate where the multiple reflections in the substrate combine incoherently. Final (practical) transmission and reflection of the thick substrate is

$$T = \int_0^{2\pi} T_{italic}\, d\varphi_2 \,, \tag{3.6}$$

$$R = \int_0^{2\pi} R_{italic}\, d\varphi_2 \tag{3.7}$$

Equations (3.6) and (3.7) are now the desired equations for the practical case of a uniform, homogenous and absorbing film on a thick substrate. The equations are exact, contain no approximations and are valid for all values of *n, k* and *d* irrespective of the absorbance of film and substrate.

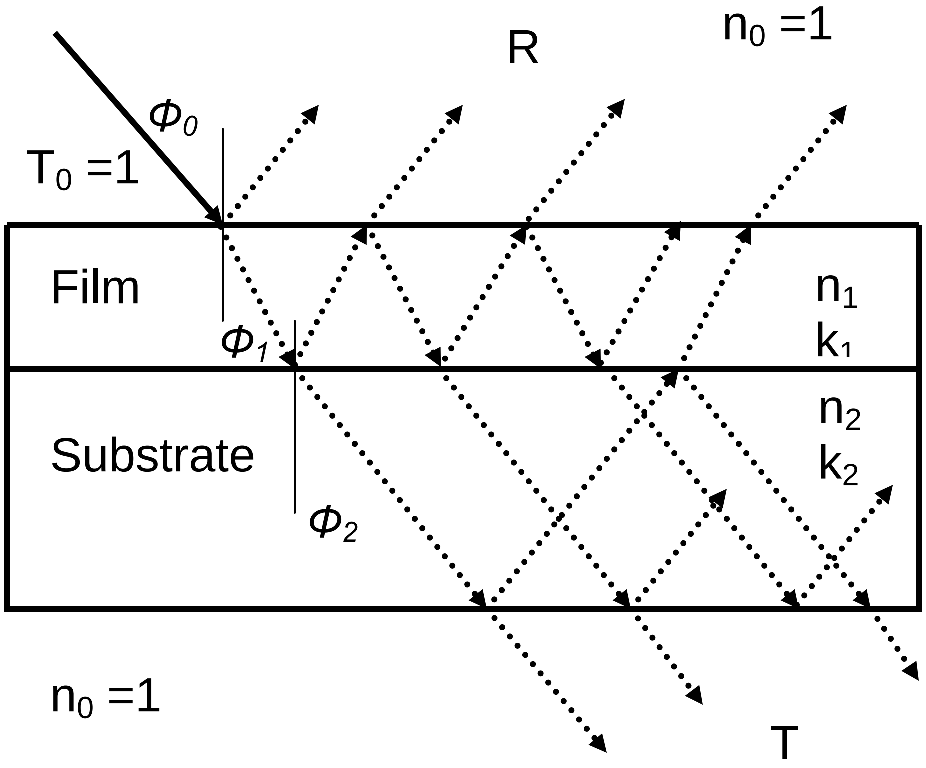

Figure 3.1. Transmission and reflection of the ambient-film-substrate system.

3.2.2 Transmission by a single film or single substrate system

The transmission and reflection of a single film can also be expressed simply by just modifying equation (3.3), (3.4) a little bit. We have only to make the following substitutions;

$$\tilde{r}_{20} = 0, \tag{3.8}$$

$$\tilde{r}_{12} = -\tilde{r}_{01}, \tag{3.9}$$

$$\chi_2 = 1. \tag{3.10}$$

Again, the interference pattern disappears when a single film or single substrate is thick enough for $\Delta\lambda_e < \Delta\lambda$. The transmittance and reflectance expression will be equation (3.6) and (3.7) with substitutions of (3.8), (3.9), (3.10). In this case, the final transmission and reflection spectrum are functions of wavelength λ, refractive index (n), transmittance (χ) and thickness d of single film (substrate). The thickness of a thick substrate can usually be easily determined on the micrometer scale, then the refractive index (n) and film transmittance (χ) (or extinction coefficient) can be calculated by measuring both transmission and reflectance simultaneously.

$$T(\lambda)_{\text{measured}} = T(\lambda; n_{\text{sub}}, \chi_{\text{sub}}), \tag{3.11}$$

$$R(\lambda)_{\text{measured}} = R(\lambda; n_{\text{sub}}, \chi_{\text{sub}}). \tag{3.12}$$

Provided the substrate is transparent, then one of the two above equations is enough to obtain the refractive index (n_{sub}) easily. The equations become;

$$T = \frac{2n_{sub}}{1 + n_{sub}^{\ 2}} \tag{3.13}$$

$$R = \frac{(1-n_{sub})^2}{1+n_{sub}^{\;2}} \tag{3.14}$$

3.2.3 Transmission by heterogeneous films on a substrate system.

It is clear that in the field of III-V devices buffer layers are necessary and are of crucial importance these days to the controlled manufacture of devices.[19,20] In the hetero-structured film case, the transmission and reflection spectrum is greatly changed compared to the single film case. Practical transmittance (no effect of substrate interference) can be easily generated by equations (3.1), (3.2) and (3.3). In the case of two films on a substrate, the scattering matrix S is as follows.

$$S = \boldsymbol{I_{01}L_1I_{12}L_2\,I_{23}L_3\,I_{30}} \tag{3.15}$$

For example, let's assume AlN is deposited on a GaN buffer layer on a sapphire substrate. The refractive indexes of AlN, GaN and sapphire were obtained from manufacturers.[21] But for simplicity, extinction coefficients of all layer are assumed to be zero. Fig. 3.2(a) displays the calulated transmission when d_{AlN} = 800 nm and d_{GaN} = 400nm.(The thickness of substrate has no effect on transmission because it is too thick as describe above assuming it is transparent). For comparison, single films of AlN (thickness : 1200nm) and GaN(thickness : 1200nm) on a sapphire substrate are illustrated in Fig. 3.2 (b) and 3.2 (c) respectively. As Fig 3.2 (a) shows, clear differences can be observed in the case of hetero-structurs. In the single film case, there are no big fluctuations on the maxima and minima envelope. However, in the hetero-structured case, big fluctuations can be observed. From this transmission, we can say that *n*, *k*, and the film thickness of each layer directly determine the shape of the transmission (or reflection) spectrum over a wide wavelength range.

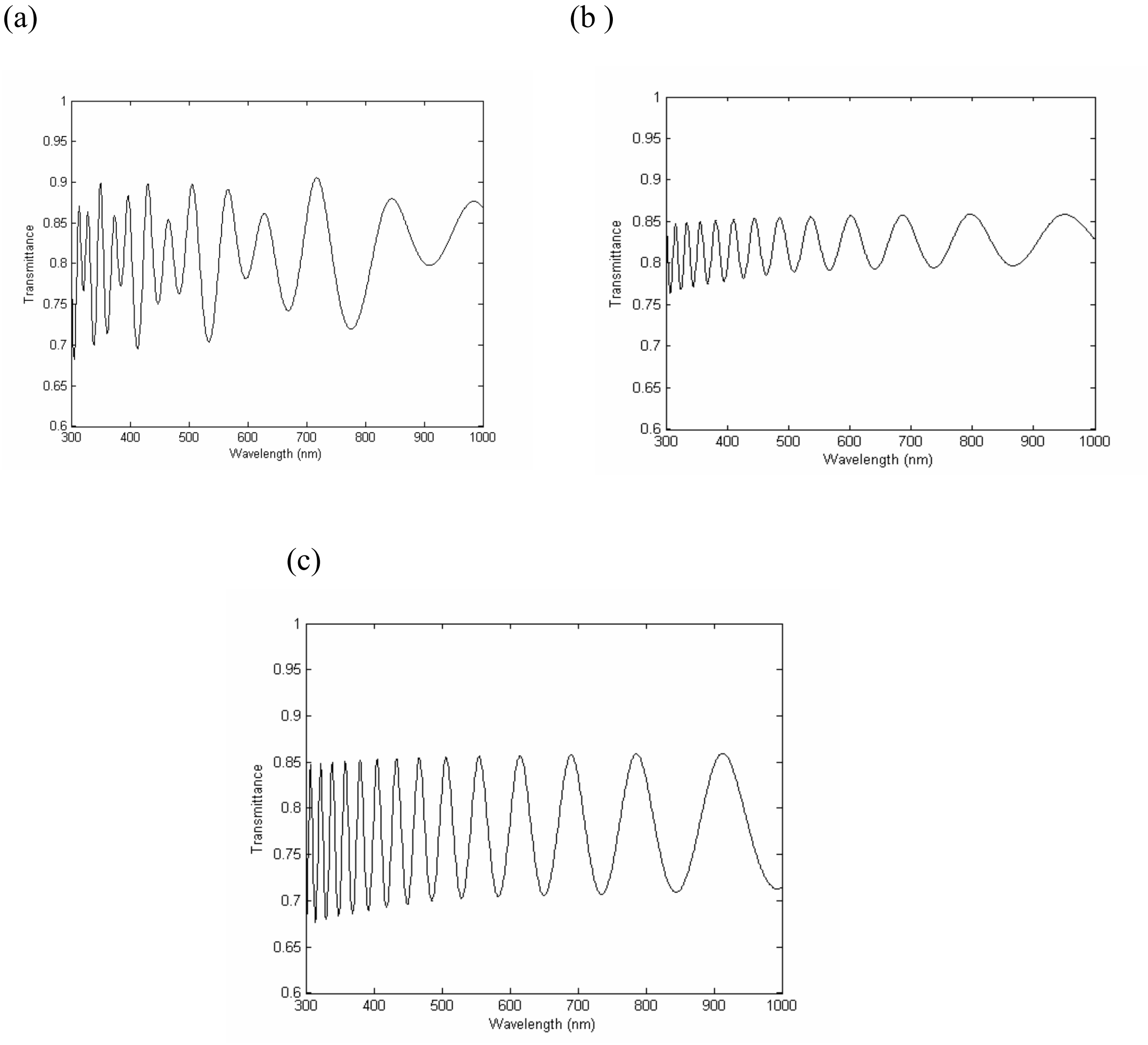

Figure 3.2 (a). Simulated transmission of the hetro-structure AlN (800 nm)-GaN (400 nm) on a thick sapphire substrate. (b). Transmission of AlN (1200 nm) on a sapphire substrate. (c). Transmission of GaN (1200 nm) on a sapphire substrate

3.3 Non-uniformity in film thickness

3.3.1 Background

We have studied the uniform film case so far. As mentioned previously, non-uniformity in thickness of thin films can severely distort their transmission and reflection spectra as compared to those of flat, smooth films. In this section, we will show how non-uniformity distorts the transmission and how we can get exact optical information of those non-uniform films from distorted spectra. From now on, only transmition will be investigated unless specifically stated because reflection can be explained in exact same way.

We start by considering a homogeneous thin film of uniform thickness, d, refractive index, n, and extinction coefficient, k (complex refractive index, $\tilde{n} = n - ik$) again. For practical cases, the film is on a transparent substrate with refractive index, s. The substrate is considered to be perfectly smooth, but thick enough so that interference effects due to the substrate are neglected as described in section 3.2.1. The system is surrounded by air with a refractive index, $n_0 = 1$. Taking all the multiple reflections at the three interfaces into account, we can get an exact expression from equations (3.3) and (3.5) numerically. However, Swanepoel[11] derived the following simple analytical expression without any approximations.

The value of the optical transmission, T, for normal incidence that is given by

$$T = \frac{A\chi}{B - C\chi + D\chi^2} \tag{3.16}$$

where

$$\begin{aligned}
A &= 16s(n^2+k^2) \\
B &= [(n+1)^2 + k^2][(n+1)(n+s^2) + k^2] \\
C &= [(n^2-1+k^2)(n^2-s^2+k^2) - 2k^2(s^2+1)]2\cos\varphi \\
&\quad - k[2(n^2-s^2+k^2) + (s^2+1)(n^2-1+k^2)]2\sin\varphi \\
D &= [(n-1)^2+k^2][(n-1)(n-s^2)+k^2] \\
\varphi &= 4\pi nd/\lambda,\ \chi = \exp(-\alpha d),\ \alpha = 4\pi k/\lambda
\end{aligned} \tag{3.17}$$

It should be noted that these formulae are valid only for smooth films with uniform thickness.

The case now considered is shown schematically in Fig. 3.3(a). It is assumed that the film is wedged so that the thickness varies linearly over the long dimension (x-direction) of the illuminated area so that the thickness can be expressed in the following form;

$$d = \bar{d} + \beta\ \Delta d, \tag{3.18}$$

where $\beta = 2x/L \quad (-1 \le \beta \le 1)$, (3.19)

Δd is the local deviation in thickness from the average thickness $\bar{d}$, and x is the position across the aperture as shown in the Fig. 3.3(a). The OPE method was derived to be applied to films with a 1-D linear variation in d as shown in Fig. 3.3 (a). We show that the OPE method can be extended to cases where there is a transverse linear thickness variation or where several 2-D irregularities occur over the illuminated area in section 3.3.2.2. Fig. 3.3 (b-d) show examples of triangular, rectangular and sinusoidal surface irregularities.

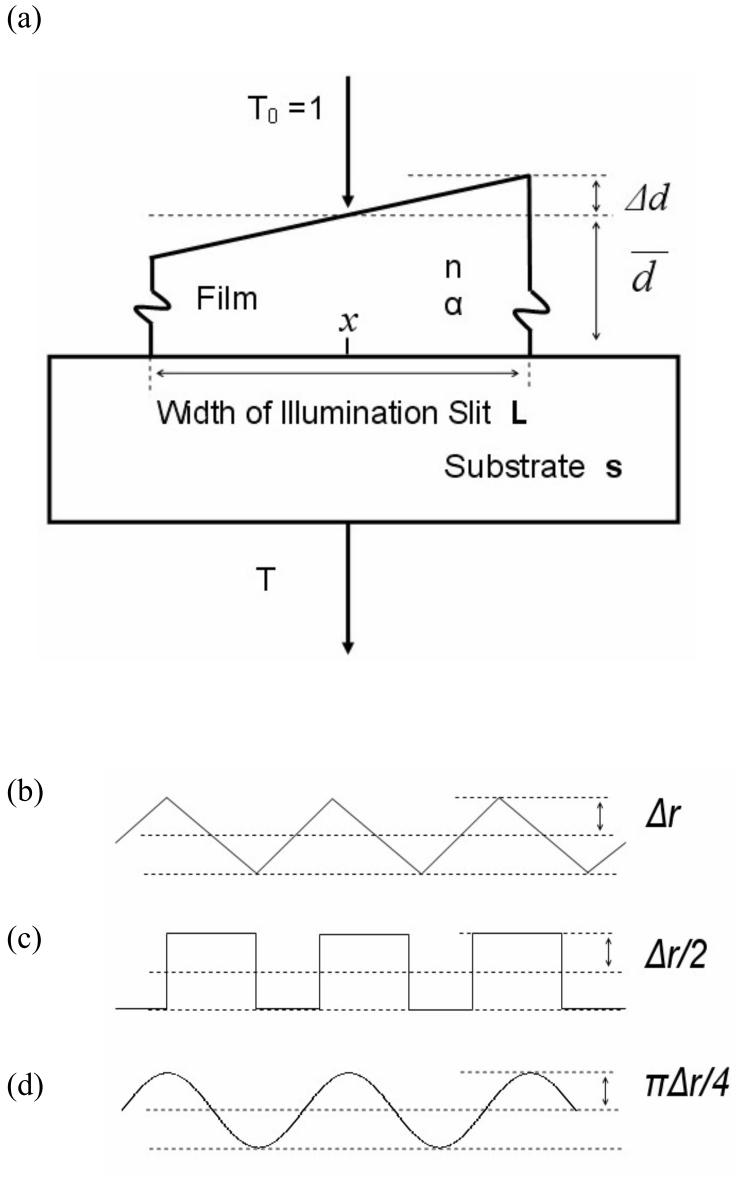

Figure 3.3 (a) An absorbing thin film with a variation in thickness on a thick finite transparent substrate, (b) triangular surface irregularities, (c) rectangular surface irregularities, and (d) sinusoidal surface irregularities.

The meaning of Δr is indicated in the figures. The triangular, rectangular, and sinusoidal variations have calibration factors of 1, 1/2, π/4, but other periodic surface irregularities could be considered by applying an appropriate calibration factor. Recently, J. M. Gonzalez-Leal et al.[22] applied their wedge-shaped envelope method to low-loss films having 2-D surface irregularity parameterized by a single Δd, and no wedge.

The transmission $T_{\Delta d}$ at a specific wavelength for the case of 1-D non-uniform thickness can be obtained by integrating Eq. (3.16) over *d*, *n* and *k*. However, this is prohibitively difficult analytically, and a simplifying assumption is to use an average value of *n* and *k* over the range of integration over thickness. This approximation is excellent provided $\Delta d \ll \overline{d}$. Thus, the expression for the transmission $T_{\Delta d}$ is

$$T_{\Delta d} = \frac{1}{\varphi_2 - \varphi_1} \int_{\varphi_1}^{\varphi_2} \frac{A\chi}{B - C\chi + D\chi^2} d\varphi \tag{3.20}$$

where $\varphi_1 = (\overline{d} - \Delta d)/\lambda$ and $\varphi_2 = (\overline{d} + \Delta d)/\lambda$.

The integral can easily be converted mathematically to the following simpler form that parameterizes the non-uniformity using the non-dimensional parameter β.

$$T_{\Delta d} = \frac{1}{2} \int_{-1}^{1} \frac{A\chi}{B - C\chi + D\chi^2} d\beta \tag{3.21}$$

where $d = \overline{d} + \beta \Delta d$ and $-1 \le \beta \le 1$ over the length of the measurement beam, *L*.

We now extend this concept to the case of 2-D wedge and thickness variation simultaneously to arrive at a case that will be close to the worst-case for real-world samples. In this case, the thickness can be expressed in the following form,

$$d = \overline{d} + \beta \Delta d_x + \gamma \Delta d_y + \delta \Delta r_x + \varepsilon \Delta r_y \tag{3.22}$$

where $-1 \leq \beta, \gamma, \delta, \varepsilon \leq 1$, and Δd_x and Δd_y are the variations in film thickness due to the wedge in the x and y directions respectively. Similarly, Δr_x, Δr_y are the other thickness variations. The integral expression for the optical transmission of this wedged and non-uniform film becomes

$$T_{\Delta d} = \frac{1}{2}\cdot\frac{1}{2}\cdot\frac{1}{2}\cdot\frac{1}{2}\int_{-1}^{1}\int_{-1}^{1}\int_{-1}^{1}\int_{-1}^{1} \frac{A\chi}{B - C\chi + D\chi^2}\, d\beta\ d\gamma\ d\delta\ d\varepsilon \tag{3.23}$$

Equation (3.23) is valuable when the illumination is a 2-D rectangular area rather than 1-D line, and it includes the effects of both wedge and other variations simultaneously. In this paper, the illumination area is confined to 1-D by putting a long narrow slit in front of the light source so that we have only to consider 1-D non-uniformity. We will evaluate the error introduced by this assumption in section 3.3.2.2. Usually, thin films have sufficiently small thickness non-uniformity that the wedge dominates. Our numerical fitting of the films' optical constants will be conducted assuming such a 1-D wedged smooth film.

The reliability of fitting methods for determining film properties depends mainly on the dispersion model that is employed; often this is a more or less empirical choice. Fitting methods and dispersion equations are used in several commercial thin optical design and analysis software packages such as TFcalc[23] and Film Wizard[24]. The dispersions equations that are generally used are the Cauchy equation[25], the Sellmeier equation[26], the Foroughi-Bloomer equation[27] and the Drude equation[28]. Any of these dispersion equations can give very good results for a large number of materials over quite a wide range of wavelengths. A particular dispersion model is applicable if there is a good fit between experimental transmission spectrum and the one calculated using that equation. Certainly, all of these dispersion equations are slowly varying functions of wavelength and it is very unlikely to produce a good fit over a wide wavelength range if the values of n, and k are incorrect. This is due to the fact that n, k, and the film thickness directly determine the form of the transmission (or reflection) spectrum. From the point of view of the fitting routine, a simpler dispersion expression with fewer adjustable parameters is more efficient and effective for fitting measured data. To accelerate the fitting routine and to avoid finding local minima instead of the global minimum, we propose a packing-density model for refractive index. In this model, refractive index has one fitted parameter, the packing density, p. That is,

$$n(\lambda) = p\,(n_{ref}(\lambda) - 1) + 1 \quad , \tag{3.24}$$

where $n_{\mathrm{ref}}(\lambda)$ is the reference refractive index that has previously been measured or tabulated for a similar thin-film or bulk material. In other words, $n(\lambda)$ is free to increase or decrease, but not change its frequency-dependent shape. Provided that we know the film material and that the change of the film refractive index dispersion due to experimental factors is not large, this packing-density model is very accurate. This technique is particularly effective for very thin, strongly absorbing and/or severely wedged films, since the OPE method can give a unique solution no matter how small or few are the interference fringes in the transmission spectrum. Conventional models tend to suffer from multiple solutions in these cases.

The second dispersion parameter is the extinction coefficient. We have chosen the exponential form,

$$k(\lambda) = A exp(B/\lambda). \tag{3.25}$$

where A and B are fitted constants. This exponential model is the simplest among several common models, very effective because a large number of thin-film materials show an exponential UV absorption edge[29, 30, 31, 32], and widely adopted in other thin-film models. There are two more unknown parameters needed for determining film transmission: average thickness, $\overline{d}$, and non-uniformity, Δd. Implicit in this definition is a length of the measured area, L, or alternatively a wedge angle, $\theta = \tan^{-1}(\frac{2\Delta d}{L}) \approx \frac{2\Delta d}{L}$, for the film surface (see Eqs. (3-18), (3-19) and Fig. 3.3(a)). Using this set of parameters, the transmission of a 1-D wedge-shaped thin film can be determined from Eq. (3.21).

Our OPE method minimizes the difference between the measured spectrum and the simulated one with optimized values of dispersion constants, thickness and non-uniformity. This difference or cost function is defined as

$$Cost = [\frac{1}{m}\sum_{j=1}^{m}((T_{ex,j} - T_{fit,j}) \cdot W_j)^2]^{1/2} \tag{3.26}$$

where m is the number of optimization targets (spectral measurement positions), $T_{ex,j}$ and $T_{fit,j}$ are respectively the experimental and fitted transmission values at the j-th wavelength, and W is a weighting factor for each wavelength. Cost is the quantity that the optimization process attempts to minimize. To minimize the cost, we utilized the sequential quadratic programming (SQP) method[33, 34] implemented in Matlab. In the SQP method, a quadratic programming (QP) sub-problem is solved for each iteration. Optimization variables may all be varied simultaneously, but this may cause convergence to multiple local minima and make it difficult to find the global minimum (best solution). This problem is partially alleviated by reducing the number of optimization variables by employing the packing-density model for the refractive index and the 2-variable exponential model for the extinction coefficient. To further reduce the likelihood of converging to a local minimum, appropriate initial values that are practical and reasonable are essential. Constraints can also be used to limit the parameters found by optimization to save time and avoid unreasonable values. Although uniform weighting is normally used, we can use appropriate weighting factors in the cost. For example, when only the optical information at the long wavelength region is required, larger weighting factors can be used for the long wavelength terms in the cost. This gives better agreement between experimental data and simulated data in the long wavelength region. Care must be exercised however when using weighting factors in this way because disagreement can increase in the short-wavelength region depending on the dispersion model used.

3.3.2 Model Films

Model films are useful in testing film parameter computation techniques such as the OPE method since the transmission (or reflection) spectra can be calculated exactly and the exact starting film parameters are known so that they can be compared to the extracted parameters for error analysis. A much wider range of test cases are also possible since the films do not have to be actually fabricated. The method can be tested for convergence to the correct solution and its absolute accuracy. Finally, the additional uncertainty of making a physical measurement of the fabricated film parameters is eliminated. For this investigation, we have studied both model films (this section) and actual deposited AlN films (section 3.3.3.) to test the OPE method.

As mentioned above, the only practical method that can be currently used to correctly extract optical constants for non-uniform thin films is the wedge-shaped envelope method. However, this method is accurate only when the absorption of the film at long wavelengths is very small. In the first part of this section, we will show how a large error can result when applying the wedge-shaped envelope method to absorptive wedge-shaped model films. We also apply our OPE method for comparison. In addition, the advantages and disadvantages of these methods are discussed.

In the second part of this section, we investigate how much error occurs using the OPE method, but fitting only 1-D non-uniformity in film thickness. Due to a finite illumination slit width, transmission spectra exhibit the effects of 2-D non-uniformity in both thickness and roughness. In principle, we can get more accurate information by considering all these effects in the OPE fitting procedure. However, there is a practical difficulty in considering all of them simultaneously because the cost function, Eq. (3.26), will have many more local minima around the global minimum; thus making it impossible or extremely time consuming to converge to the global minimum with our algorithm. We will demonstrate that the reduction of the OPE method to 1-D for practical apertures is a good approximation, even when the films exhibit some 2-D non-uniformity.

3.3.2.1 Limitations of wedge-shaped envelope method

To check the reliability of the wedge-shaped envelope method for absorbing films, various simulated transmission spectra with 1-D non-uniformity in thickness were generated from Eq. (3.21) by postulating values for refractive index, extinction coefficient, thickness, and non-uniformity. Both the wedge-shaped envelope method cited in the references[35, 36, 37, 38] and the OPE method were used to extract optical properties from the transmission spectra, and these values were compared with the true values.

The following is a brief description of the wedge-shaped envelope method. Analytical expressions for the envelopes around the interference maxima and minima of the transmission spectrum are derived by solving Eq. (3.20) with the assumption that the absorption is approximately zero in the long-wavelength region. The optical properties are obtained by solving those equations given the experimental envelopes. Upper and lower experimental envelopes are computationally derived from the measured transmission spectrum using the algorithm suggested by McClain et al.[39]

For these test cases, the refractive index of the films is assumed to be that of bulk AlN as reported by manufacturers,[40] and it is shown in Table 3.1. The packing-density model with $p = 1$ is used with this form of $n(\lambda)$. The extinction coefficient, k, is assumed to be constant over the range of wavelengths from 200 to 1200 nm. Thickness non-uniformity, Δd, is assumed to be 40 nm for all cases. The results computed by the wedge-shaped envelope method for two film thicknesses and four different extinction values are shown in Table 3.2. Fig. 3.4 plots these errors in thickness, $\overline{d}$, and non-uniformity, Δd, versus film transmittance, $\chi = e^{-\alpha \cdot d}$, for a 2000 nm thick film at a wavelength of 633 nm. Note that film transmittance varies opposite to both extinction coefficient and absorption coefficient, α. These data clearly show that the error increases as extinction coefficient increases (film transmittance decreases). The computed value of film thickness is always less than the true value, thus leading to an overestimate of the refractive index. The error in Δd is even more sensitive to the extinction coefficient. When using the wedge-shaped envelope method, errors of less than 5% in $\overline{d}$ are only obtained when the film transmittance is greater than 0.98. Therefore, large errors are possible when the wedge-shaped envelope method is applied to absorbing films. Indeed, some extinction coefficients reported previously for various arsenic sulfide films were negative for some wavelengths and transmission values were larger than the substrate transmission when the wedge-shaped envelope method was used. These results are clearly unphysical. Even for less extreme cases, this method leads to an overestimate of the refractive index and an underestimate of the film thickness.

In contrast, our OPE method uses an exact equation for the transmission spectra without any mathematical approximations. The values for all of the parameters determined by the OPE method matched exactly with their actual values in the model films (with < 0.1% error). Moreover, the OPE method has the following advantages over other methods:

1. The ranges of refractive index and extinction coefficient that may be computed are larger than any other envelope method.
2. The packing-density model works well regardless of the number of interference fringes in the transmission spectrum; other methods (both fitting methods using other dispersion models and other envelope methods) require a minimum number of interference fringes to produce accurate results. Accordingly, other methods require moderate film thickness, low absorption, and minimal non-uniformity.
3. It is robust with respect to the signal-to-noise ratio of the data. In the envelope methods, small errors in transmission due to noise result in quite large errors in the determination of thin-film parameters.

The OPE method also has limitations; one has to know (or estimate) the dispersion of the refractive index for the film material before starting the fitting procedure when using the packing-density model. Usually, it is sufficient to know $n(\lambda)$ for the compound in the bulk or thin-film form. We discuss an alternative dispersion model in section 3.3.3.4 if $n(\lambda)$ is totally unknown. If the model is not appropriate, then the disagreement between the measured (or simulated) transmission spectrum and the fitted one is usually quite large.

Wavelength (nm)	Refractive index
200.00	2.492
248.00	2.310
275.56	2.220
310.00	2.160
354.29	2.110
413.33	2.078
496.00	2.050
620.00	2.020
836.67	2.005
1240.00	1.990

Table 3.1. The refractive index of bulk AlN.

We assumed packing density, $p = 1$, thickness variation, $\Delta d = 40$ nm, extinction coefficient, k was constant versus wavelength for all films in the table. Film transmittance ($\chi = e^{-\alpha \cdot d}$) at a wavelength of 633 nm was calculated for each film.

d (nm)	1000			2000			
k	10^{-4}	5×10^{-4}	10×10^{-4}	0	1×10^{-4}	5×10^{-4}	10×10^{-4}
χ at 633nm	0.998	0.990	0.980	1.000	0.996	0.980	0.961
Error (%) of d	- 1.5	- 2.8	- 4.2	- 0.1	- 1.1	- 4.8	- 17.4
Error (%) of Δd	5.5	8.1	12.7	1.1	5.8	18.9	31.8
Error (%) of n	1.5	2.9	4.4	0.0	1.1	5.0	11.5

Table 3.2. Error % for thickness, $\overline{d}$, non-uniformity, Δd, and index of refraction, n, due to non-zero extinction coefficient using the wedge-shaped envelope method.

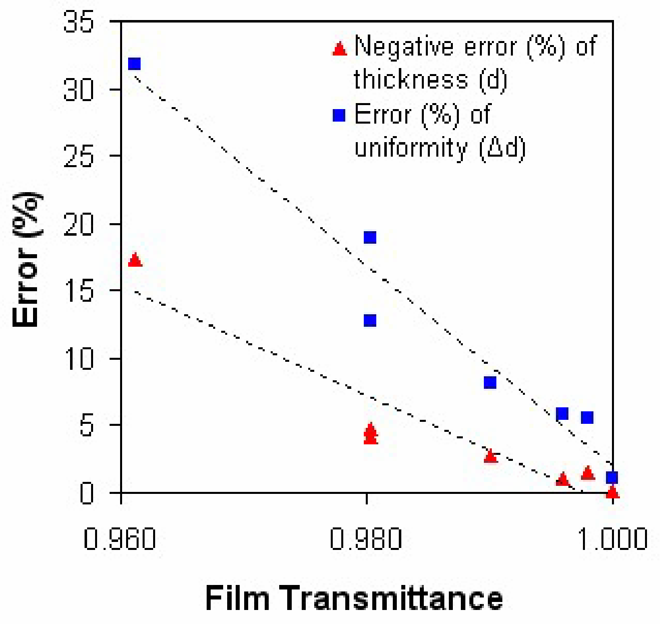

Figure 3.4. Plot of the error of thickness, $\overline{d}$, and non-uniformity, Δ*d*, versus film transmittance ($\chi = e^{-\alpha \cdot d}$) at 633 nm using the wedge-shaped envelope method. The simulated film had a thickness of 2000 nm and Δ*d* = 40 nm. The dotted lines are a guide to the eye.

3.3.2.2 Model system with 2-D non-uniformity

Why do we consider only one dimensional wedge even though two dimensional wedges and other thickness variations exist? Considering both dimensions including the x-directional wedge ($\Delta d_x, \Delta d_y$) and non-uniformity ($\Delta r_x, \Delta r_y$), don't we get more accurate information than considering only one-dimensional wedge information (by putting a long narrow slit)? The answer to this question is Yes and No. If we consider all thickness variations to simulation parameters, it will produce a good fit over a wide wavelength range in principle. However, practically it is impossible with respect to optimization. From the model film simulations, considering all thickness variations to simulation parameters, the cost function, Eq. (3.26), turns out to have many more local minima around the global minimum from the model film simulations; thus making it impossible to converge to the global minimum (best solution) with our algorithm.

The error of the one dimensional assumption can be alleviated by putting a long narrow slit before the light source. Because transmission spectra are in practice acquired using a finite aperture width, one might still worry about the errors caused by this technique. We devised several simulations to ascertain how large these effects are on the extracted optical parameters, and to check for convergence and absolute accuracy of the OPE method. First, to determine the effect of linear thickness variations transverse to the aperture axis and of other thickness non-uniformity (Δr) on transmission spectra, we simulated the transmission spectra with the standard AlN refractive index ($p = 1$), a constant extinction coefficient over the whole wavelength range ($k = 1\times10^{-3}$), and a 2000 nm thick film. Transmission was calculated using Eq. (3.23) while simultaneously including 2-D wedge and non-uniformity. The four cases generated were $T\,(\Delta d_{\mathrm{x}}= \Delta d_{\mathrm{y}}= \Delta r_{\mathrm{x}} = 0)$, $T(\Delta d_{\mathrm{x}}= 40)$, $T\,(\Delta d_{\mathrm{x}}= 40, \Delta d_{\mathrm{y}}= 20)$, and $T\,(\Delta d_{\mathrm{x}}= 40, \Delta d_{\mathrm{y}}= 20, \Delta r_{\mathrm{x}} = 10)$.

The transmission spectra for these cases are shown in Fig. 3.5. In Fig. 3.5(b), the wavelength range of 355-375 nm is magnified to show the effects on the interference ripples. As is expected, the envelope for $T\,(\Delta d_{\mathrm{x}}= 40)$ is severely decreased compared to $T\,(\Delta d_{\mathrm{x}}= \Delta d_{\mathrm{y}}= \Delta r_{\mathrm{x}} = 0)$ (Fig. 3(a)). $T\,(\Delta d_{\mathrm{x}}= 40)$, $T\,(\Delta d_{\mathrm{x}}= 40, \Delta d_{\mathrm{y}}= 20)$ and $T\,(\Delta d_{\mathrm{x}}= 40, \Delta d_{\mathrm{y}}= 20, \Delta r_{\mathrm{x}} = 10)$ are indistinguishable in Fig. 3.5(a). Fig. 3.5(b) shows that the envelopes for the cases with a transverse thickness variation and non-uniformity are further reduced. From these test cases, it appears that envelope distortion depends mainly on the wedge parallel to the aperture and less on transverse variations. This severe change in the transmission spectra envelopes explains why the conventional envelope method can fail for wedge-shaped films. Furthermore, it gives an indication that not considering transverse thickness variations in a fitting method can still give good estimates of film properties. This is considered next.

To check the ability of the OPE method to derive optical constants of absorbing samples that have some transverse non-uniformity in the spectrometer aperture, several simulated transmission spectra were generated by postulating the refractive index, extinction coefficient, thickness, wedge and non-uniformity values shown in Table 3.3 for eight cases for 2000 nm thick films. Again, the refractive index of all films was assumed to be AlN ($p = 1$), and the extinction coefficient was assumed to be constant ($k = 1\times10^{-3}$) over the entire wavelength range. Transverse non-uniformity (Δr_y) was assumed to be zero, but the cases included longitudinal non-uniformity (in addition to wedge) and transverse wedge. The 1-D OPE method that considers only longitudinal wedge was applied to extract the optical constants, and we compared these values with actual values input into the transmission spectrum calculation. The fitted parameters and error percentages for the eight cases are shown in Table 3.3. From this data it is apparent that the error for refractive index and film thickness are less than 1%; even for the cases where the deviation transverse to the slit is as large as the thickness variation longitudinal to the measurement slit. Errors for k were less than 5%, but errors for Δd were much larger. The effects of transverse thickness variation and surface roughness were interpreted by the OPE method, when restricted to 1-D variation, as an increase in the value of Δd_x. By far, transverse thickness makes the largest contribution to this error; but it only generates an error of 8.2% in Δd_x when $\Delta d_y = \Delta d_x/2 = 20$ nm.

Fig. 3.6 shows the simulated transmission spectrum generated for the case ($\Delta d_x = 40, \Delta d_y = 20, \Delta r_x = 10, \Delta r_y = 0$) and the transmission spectrum derived from the fitted parameters using the OPE method. Fig. 4(a) shows the whole spectrum while Fig. 4(b) magnifies the range of wavelengths from 360-480 nm. The OPE method overestimates the non-uniformity in thickness by 4 nm (44 instead of 40 nm), which leads to disagreement in the spectra at short wavelengths. The transmission envelope of the film with Δd_x = 44 nm decreases faster as wavelength decreases than the envelope generated with both 2-D wedge and non-uniformity ($\Delta d_x = 40, \Delta d_y = 20, \Delta r_x = 10, \Delta r_y = 0$). As Table 3.3 indicates, the errors caused by assuming only a 1-D wedge and perfect smoothness is less than 0.7% and 0.36% in refractive index and thickness, respectively, even in the most extreme case shown. The largest errors result when square illumination is used and the thickness variation is equal in both dimensions. However, even in this case, T (Δd_x= 40, Δd_y= 40), the OPE method accurately predicts n, k, and $\overline{d}$. We conclude that one can apply the OPE method, considering only 1-D non-uniformity, to determine n, k, and $\overline{d}$ accurately from spectra obtained with modest rectangular slit illumination without regard to sample wedge or orientation. Furthermore, if the transverse variation within the illumination slit is less than 25% of the longitudinal variation, then Δd_x can be determined accurately as well.

(a)

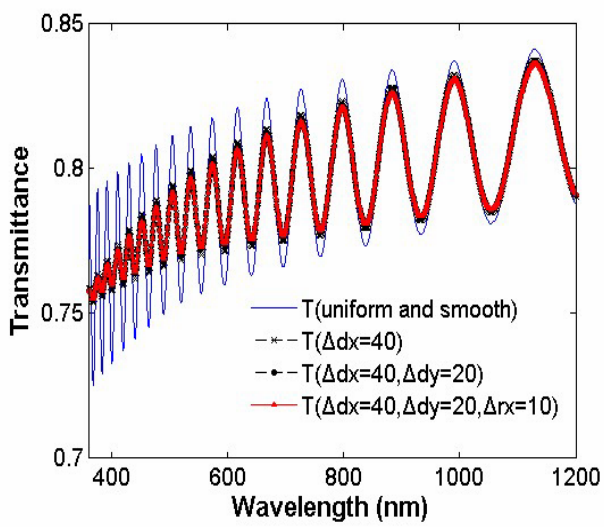

(b)

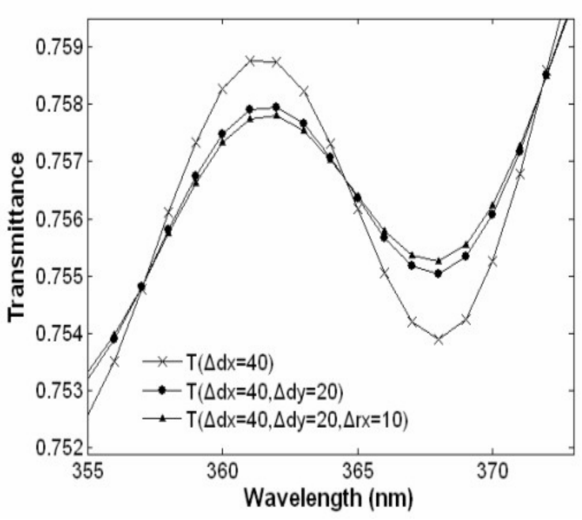

Figure 3.5 (a) Simulated transmission spectra for an absorbing film with uniform thickness and perfect smoothness compared to films with T (Δd_x= 40), T (Δd_x= 40, Δd_y= 20) and T (Δd_x= 40, Δd_y= 20, Δr_x = 10). At this scale T (Δd_x= 40), T (Δd_x= 40, Δd_y= 20), and T (Δd_x= 40, Δd_y= 20, Δr_x = 10) are indistinguishable from each other. (b) Magnified section of (a) over the wavelength range 355-375 nm.

(a)

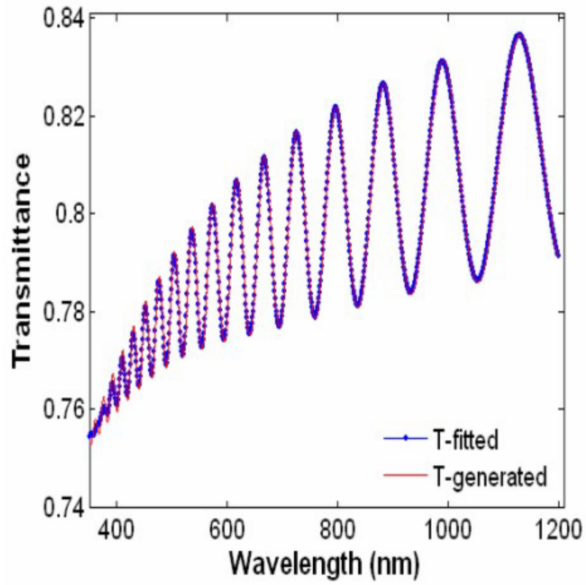

(b)

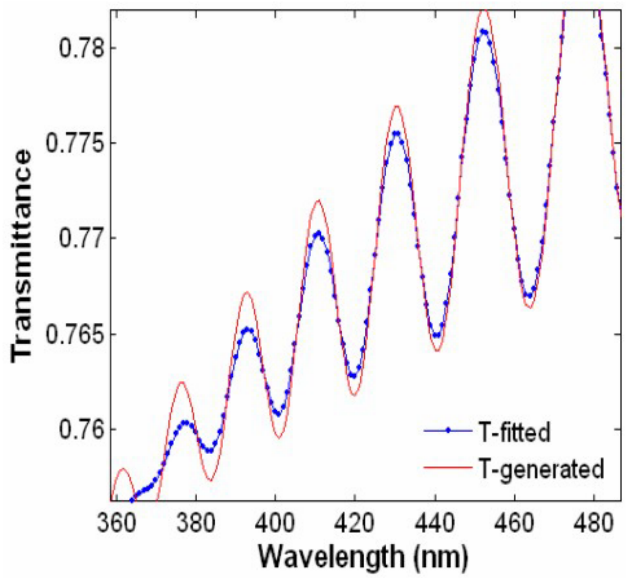

Figure 3.6 (a) Simulated transmission spectrum for an absorbing film with non-uniform thickness and surface roughness (Δd_x= 40, Δd_y= 20 Δr_x = 10) (T-generated), and the transmission spectrum derived by applying our OPE method to this data (T-fitted) using only 1-D non-uniformity (Δd_x). (b) Magnified section of (a) over the wavelength range 360-480 nm.

Table 3.3 Optical parameters and error considering only 1-D thickness non-uniformity using our OPE method.

non-	Δd_x= 40	Δd_y = 10	Δd_x= 40	Δd_y = 10	Δd_x= 40	Δd_y = 20	Δd_x= 40	Δd_y = 20
uniformity	Δr_x = 0	Δr_y = 0	Δr_x = 5	Δr_y = 0	Δr_x = 0	Δr_y = 0	Δr_x = 10	Δr_y = 0
	Fitted Parameter	Error (%)	Fitted Parameter	Error (%)	Fitted Parameter	Error (%)	Fitted Parameter	Error (%)
p	0.999	- 0.1%	0.999	- 0.1%	0.998	- 0.2%	0.997	- 0.3%
k (×10^{-4})	10.30	3.0%	10.03	0.3%	10.11	1.1%	10.14	1.4%
Δd (nm)	40.8	2.0%	41.1	2.6%	43.3	8.2%	44.0	10.1%
d (nm)	2000.6	0.03%	2000.7	0.03%	2002.2	0.11%	2002.7	0.14%

non-	Δd_x= 40	Δd_y = 30	Δd_x= 40	Δd_y = 30	Δd_x= 40	Δd_y = 40	Δd_x= 40	Δd_y = 40
uniformity	Δr_x = 0	Δr_y = 0	Δr_x = 20	Δr_y = 0	Δr_x = 0	Δr_y = 0	Δr_x = 10	Δr_y = 0
	Fitted Parameter	Error (%)	Fitted Parameter	Error (%)	Fitted Parameter	Error (%)	Fitted Parameter	Error (%)
p	0.996	- 0.4%	0.994	- 0.6%	0.993	- 0.7%	0.993	- 0.7%
k (×10^{-4})	10.22	2.2%	10.30	3.0%	10.35	3.5%	10.36	3.6%
d (nm)	2004.4	0.22%	2006.2	0.31%	2006.9	0.34%	2007.2	0.36%
Δd (nm)	47.3	18.1%	50.0	25.0%	52.8	31.9%	53.4	33.4%

Notes: The values used to simulate the spectra were: packing density, $p = 1$, extinction coefficient, $k = 10\times10^{-4}$ for all wavelengths, and average thickness $\bar{d}$ = 2000 nm. Wedges and other non-uniformity are as indicated in the table.

3.3.3. Experimental results

AlN films were grown using Pulsed Laser Deposition (PLD)[41] which was described in Chapter 2 in detail with different substrate temperatures and laser fluences. We applied our OPE method to the transmission spectra of these AlN films to determine their optical properties.

3.3.3.1 Deposition of AlN thin films

The AlN films were deposited inside a UHV vacuum system evacuated by a turbo-molecular pump to a base pressure of 1×10^{-8} Torr (1.3×10^{-6} Pa) using PLD from an AlN target. A schematic diagram of the PLD system is shown in Fig. 3.7. A Lumonics PM-848 KrF excimer laser, $\lambda = 248$ nm, PRF = 30 Hz, and $\tau = 14$ ns, was used to ablate the AlN target. The laser output was rectangular, 30 mm by 10 mm, and we used an eccentric rotating 32 cm focal-length lens to direct each pulse to a fresh location on a 1.5 mm by 3 mm oval so as to achieve as consistent ablation as possible. The target was a rectangular, stoichiometric AlN slab with a purity of 99.99% fabricated by Sputtering Materials Inc. using the pressure-assisted densification process. The target was irradiated by the laser through a UV-fused silica window at an angle of 60º to the target surface normal. The ablated material was then allowed to condense onto the heated substrate that was parallel to the target surface at a distance of 5.1 cm. Commercial sapphire (0001) substrates were first degreased with acetone and methanol in an ultrasonic bath and then were heated to 900ºC in vacuum for 45 min. prior to deposition. The depositions were carried out at different substrate temperatures varying from 100 to 800ºC for 25 min or 50 min. Ultrahigh purity nitrogen was introduced into the PLD chamber at 4.5 $\times 10^{-4}$ Torr (6.0 $\times 10^{-2}$ Pa) during deposition. The eccentric rotation of the focusing lens resulted in a factor of 3 variation in fluence around the oval path on the target (1-3 J/cm^2 and 4-12 J/cm^2 to achieve low-fluence and high-fluence sputtering regimes, respectively). Furthermore, the fluence at the sputtering target decreased slowly due to deposition on the chamber window. For all the deposition runs, the window was cleaned after a fluence drop of 25-30%. The thicknesses of the deposited films ranged from 1500 to 2300 nm for high laser fluence and from 400 to 600 nm for low fluence. The films had non-uniformity in thickness but minimal short-period surface roughness; these characteristics were verified by mechanical profilometry, Atomic Force Microscopy (AFM), and cross-section electron microscopy (SEM).

Optical transmission spectra of the films were acquired over the 200 nm to 1000 nm spectral region (1.2 to 6.2 eV) by UV-VIS spectroscopy. To mask the sample and define the illumination region, we constructed a 4 mm by 1 mm aperture, so that only 1-D non-uniformity was considered.

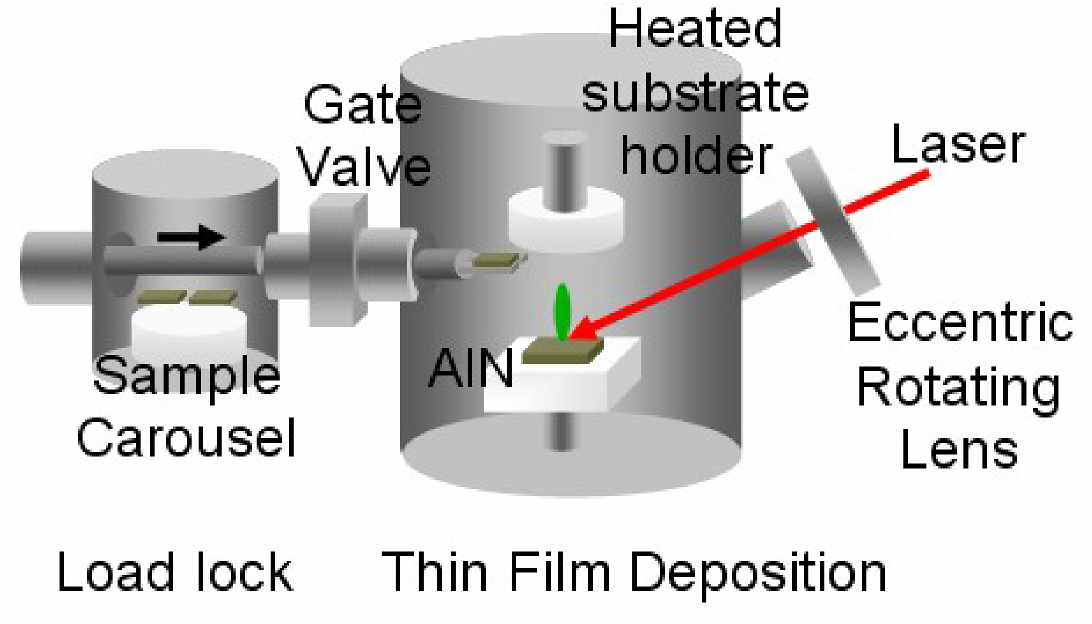

Figure 3.7 Diagram of the UHV system used for AlN film deposition with PLD.

3.3.3.2 Non-uniformity in the thickness of the film deposited by Pulsed Laser Deposition.

To check the non-uniformity of the film by PLD in the chamber, we deposited gold on a wide silicon substrate (10 cm × 10cm) at base pressure for one hour with high fluence (~25 J/cm). To measure the thickness, we put flat masks at every the 1 cm along the x axis and the y axis on the silicon substrate. Thickness measurement was performed by mechanical profilametry. The thickness distribution is shown in Fig. 3.8. One immediately observes that the film has severe non-uniformity over a wide area. Although gold thin film was deposited in this case, we can presume that similar non-uniformity in thickness in any other thin films would be expected unavoidably in our PLD technique.

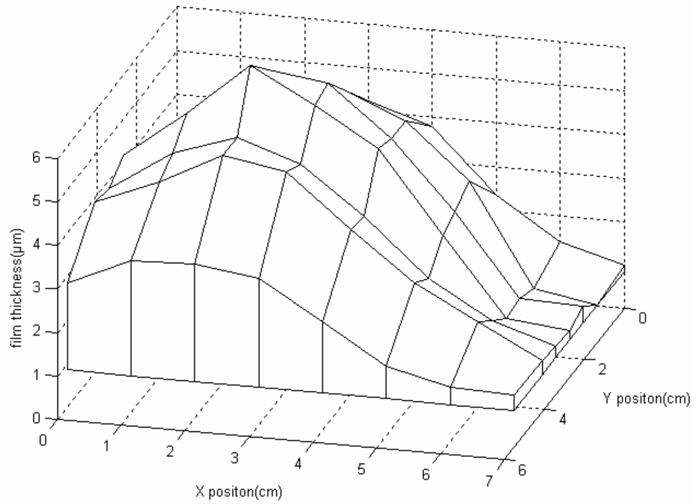

Figure 3.8 The thickness distribution of Au thin film deposited on silicon substrate for 1 hr.

3.3.3.3 The effect of non-uniformity on transmission and the convergence of the OPE method.

In section 3.3.2.2, we devised several simulations to ascertain how large the effects of nonuniformity are on the extracted optical parameters, and to check for convergence and absolute accuracy of the OPE method through a thin film model. This section will show experimental results corresponding to this simulation.

We measured the transmission spectrum for selected AlN films with and without the slit aperture to check the effect of the slit aperture. First, we measured the transmission spectra without aperture, in which case the illumination area was 12.56 mm^2. We put a 2 mm by 0.5 mm small aperture and measured the same spot again. Fig 3.9 and 3.10 shows the results for a AlN film deposited at high fluence and a 300ºC substrate temperature and a AlN film deposited at high fluence and a 500ºC substrate temperature respectively. As we expected, the envelopes without the slit decreased compared to those with the slit in both cases. The wavelengths of the maximum peak and minimum peak were virtually unchanged but the distance between maxima and minima decreased faster in the no-aperture case at short wavelength. It clearly confirmed the simulation results and showed how large effect the non-uniformity has on the transmission spectra. The Spectrum for theAlN film deposited at high fluence and a 300ºC substrate is especially interesting. The non-uniformity of this film was so severe that the interference pattern was minimized at some wavelength (around 650nm) and it began to increase gradually above this wavelength. Above this critical point, the maxima and minima have switched compared to transmission with the slit, where a maximum peak in the slit case and minimum peak in the no-slit case coexist at the same wavelength and vice versa. But those decreased again due to the inherent absorption of film at short wavelength and disappeared completely. This phenomenon can be explained clearly only by the non-uniformity of the film. We can expect the conversion point is changeable according to the illumination area and the non-uniformity in the film.

To check for the convergence and absolute accuracy of the OPE method, We applied the OPE method to the transmission with and without the slit. The measured spectral transmittance and the transmittance calculated from the parameters derived using the OPE method for the two films selected are shown in Figs. 3.11, 3.12, 3.13, 3.14. Figs 3.11 and 3.12 shows the experimentally measured and fitted transmittance (OPE method) for an AlN film deposited at high fluence and a 300ºC substrate with the slit and without the slit respectively. Figs 3.13 and 3.14 shows the experimentally measured and fitted transmittance (OPE method) for an AlN film deposited at high fluence and a 500ºC substrate with the slit and without the slit respectively. The fitted curves exactly agree with the experimental data at long wavelengths and deviate only slightly at short wavelengths in all cases. The reason for a little mismatch at short wavelengths was transverse wedge in the illuminated area as explained in detail in section 3.3.2.2. The transmittances without the slit decrease faster at short wavelengths than those without slit in both cases. This clearly shows why the generated transmission spectra for the no slit case had more mismatch at short wavelength. As described from previous simulation results, the effects of transverse thickness variation and longitudinal non-uniformity were interpreted by the OPE method, when restricted to 1-D wedge, as an increase in the value of Δd_x. The results of the OPE method was shown previously in table 3.4.

As shown in Table 3.4, differences in the refractive index, extinction coefficient and thickness is -0.3 % , 2.5% and 0.2% respectively for the AlN film deposited at high fluence and a 300ºC substrate. The difference in refractive index, extinction coefficient and thickness is -0.4 % , 3.8 % and 0.6 % respectively for the AlN film deposited at high fluence and a 500ºC substrate. It shows the convergence and robustness of the OPE method. In other words, we can conclude this Optimum Parameter Extraction (OPE) method can accommodate films with two-dimensional thickness variation with 1D aperture although the value of Δd_x is overestimated.

(a)

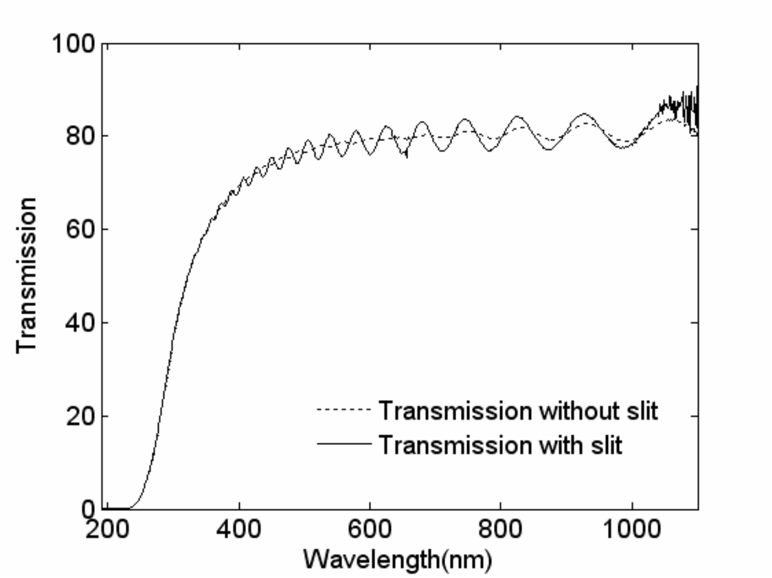

(b)

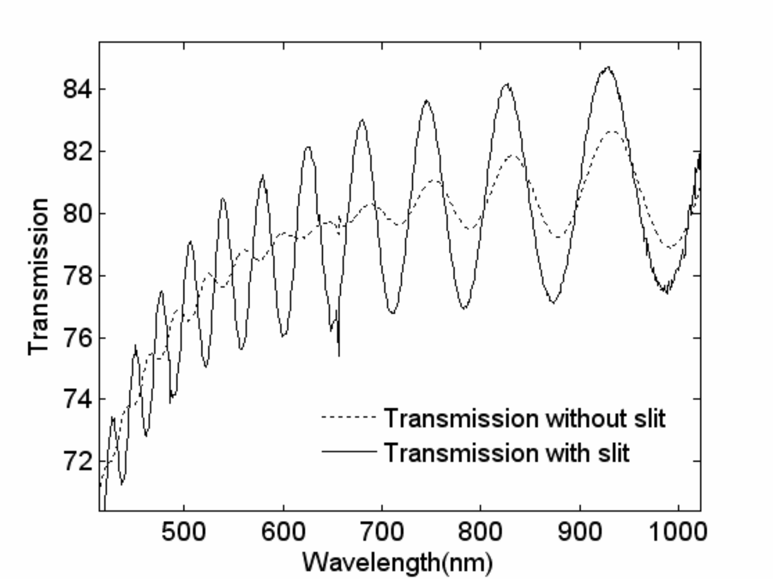

Figure 3.9. (a) Measured transmittance of an AlN film deposited at high fluence and 300ºC substrate temperature with and without slit (b) Magnified section of (a) over the wavelength range 400 -1050 (nm).

(a)

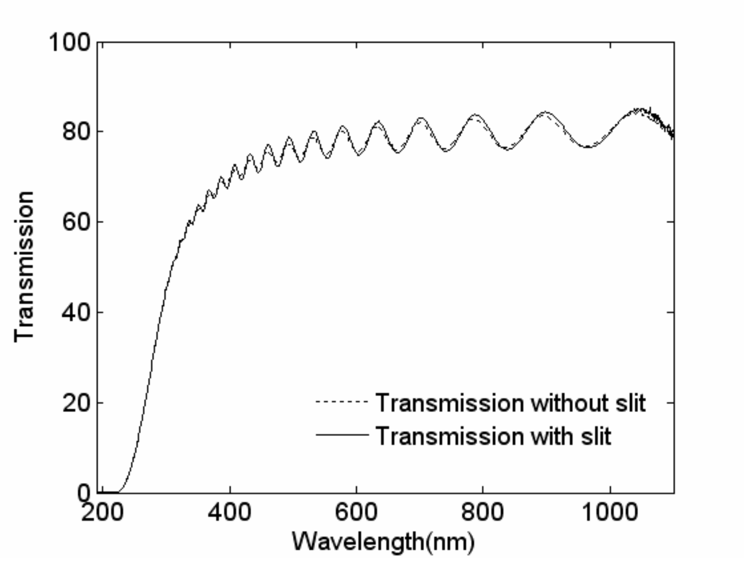

(b)

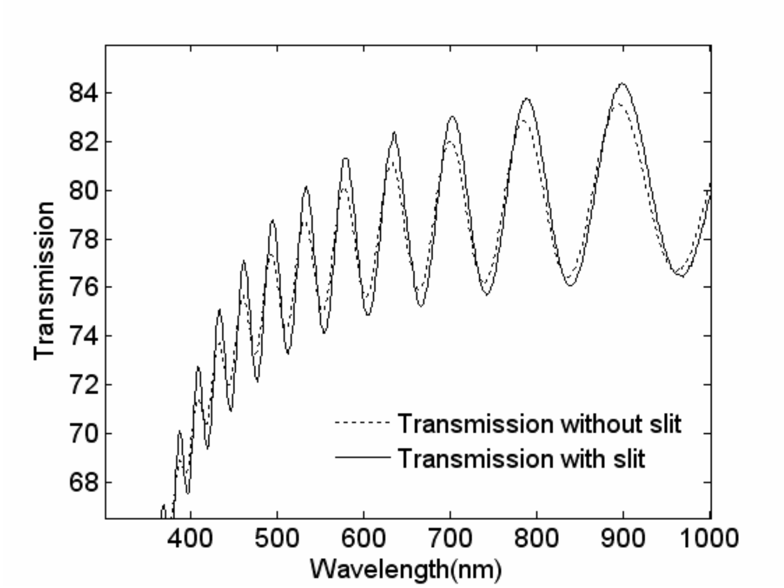

Figure 3.10 (a) Transmittance of an AlN film deposited at high fluence and 500ºC substrate temperature with and without slit (b) Magnified section of (a) over the wavelength range 300 -1000 (nm).

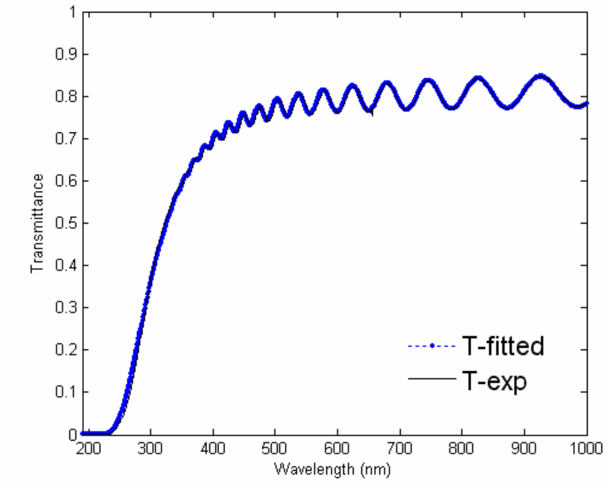

Figure 3.11 Experimental transmittance and fitted transmittance using OPE method of an AlN film deposited at high fluence and 300ºC substrate temperature (with slit). Notation in the legends: exp (experimental measurement); fitted (the OPE method).

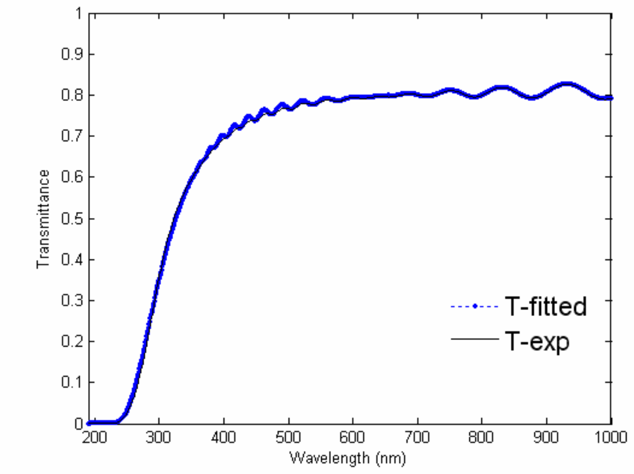

Figure 3.12 Experimental transmittance and fitted transmittance using OPE method of an AlN film deposited at high fluence and 300ºC substrate temperature (without slit). Notation in the legends: exp (experimental measurement); fitted (the OPE method).

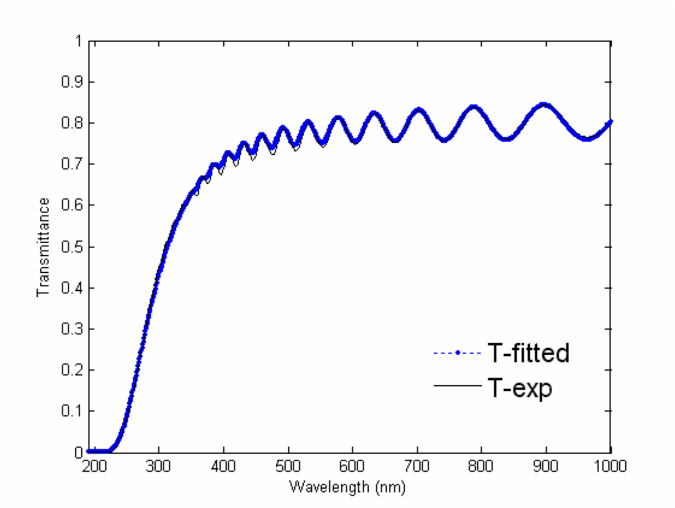

Figure 3.13 Experimental transmittance and fitted transmittance using OPE method of an AlN film deposited at high fluence and 500ºC substrate temperature (with slit). Notation in the legends: exp (experimental measurement); fitted (the OPE method).

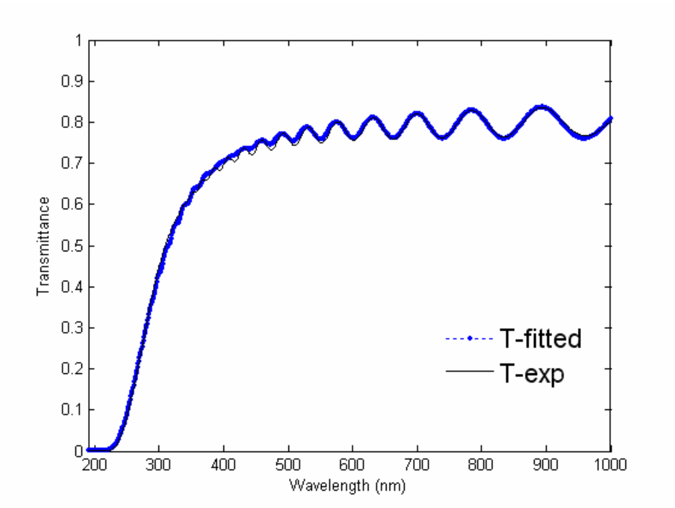

Figure 3.14 (a) Experimental transmittance and fitted transmittance using OPE method of an AlN film deposited at high fluence and 500ºC substrate temperature (without slit) Notation in the legends: exp (experimental measurement); fitted (the OPE method).

Table 3.4. Properties of AlN films with and without slit by the OPE method.

Sample	300°C			500°C		
	Without slit	With slit	Difference (%)	Without slit	With slit	Difference (%)
n at 633nm	2.093	2.099	-0.3%	2.095	2.103	-0.4%
k at 633nm($\times 10^{-4}$)	4.77	4.65	2.5%	5.04	4.85	3.8%
d(nm)	1784	1781	0.2%	1460	1451	0.6%
Δd(nm)	75	35	72.7%	52	23	77.3%

3.3.3.4 Optical properties of AlN thin films

We show here the result of applying our OPE method to all films. We utilized a 4 mm by 1 mm aperture as described in section 3.3.3.1. A subset was chosen for detailed analysis of how the various methods for extracting the optical parameters from the transmission spectra performed. Complete characterization of the films' optical and physical properties versus deposition conditions will be reported in chapter 4. The refractive index, $n(\lambda)$, extinction coefficient, $k(\lambda)$, average thickness, $\bar{d}$, and thickness variation, Δd, of our films were obtained using the OPE method. We also applied the wedge-shaped envelope method and the conventional envelope method to the two films selected for comparison. The upper and lower envelopes of the spectra were acquired using McCalain's algorithm as noted previously.

Typical results are presented in Fig. 3.15 and Fig. 3.16 for representative films deposited at high and low laser fluence. The measured spectral transmittance and the transmittance calculated from the parameters derived using the OPE method for the two films selected are shown in Figs. 3.15 (a) and 3.16 (a). The fitted curves exactly agree with the experimental data at long wavelengths and deviate only slightly at short wavelengths. Again, two possible reasons may be postulated for this deviation: 1) transverse wedge and thickness variation in the illuminated area (explained in the previous section) and 2) the single-parameter, packing-density dispersion model for refractive index did not have enough parameters to fit the short-wavelength region (300-400 nm). To check the accuracy of our dispersion model, we also applied our method substituting the Sellmeier equation to model refractive index dispersion. In this case, the derived parameters are virtually unchanged (less than 1% in refractive index and thickness), and the differences between the measured and fitted transmission spectra at short wavelengths are also similar. From this we conclude that the OPE method is robust and the small spectral difference is due mainly to thickness variation in the transverse direction in addition to 1-D wedge.

Figs 3.15 (b), (c) and 3.16 (b), (c) show refractive index (b) and extinction coefficient (c) versus wavelength derived using all three methods: the OPE method, the wedge-shaped envelope method, and the conventional envelope method. Calculated data for for these two films at a wavelength of 633 nm are shown in Table 3.5.

First, we consider which of these parameters calculated by the OPE method can be verified by physical measurements. Film thickness and thickness variation are the most amenable to direct measurement, so several types of measurements were made to document the film thickness and thickness non-uniformity. To bracket the film thickness, $\overline{d}$, a mechanical profilometer was used to measure thickness steps near both edges of each film. For all films, these measurements bracketed the OPE thickness and wedge values. A second measurement was made by scribing and fracturing a film along the center axis of the optical transmission aperture. A number of cross-section SEM micrographs were recorded along the fracture surface, and both short-range and long-range thickness variations were determined. A representative cross-section SEM micrograph is shown in Fig. 3.17 for the AlN film deposited at high fluence and a 100°C substrate temperature. One immediately observes that the film is smooth on a micron scale. Based on this and the AFM measurements of RMS surface roughness (all films < 3 nm as shown in Table 3.6), we conclude that the films do not have sufficient surface roughness to significantly scatter light or disrupt the optical interference. The long-range thickness variation of this film is plotted in Fig. 3.18. The 4 mm long aperture is centered at 40.4 mm (± 1 mm). The inset in Fig. 3.18 shows this region of the aperture and a linear least-squares fit to the data. This fit results in a center thickness of 2273 nm (± 32 nm) and a thickness variation, Δd, of 65 nm (±10 nm). The corresponding OPE derived parameters, $\overline{d}$ and Δd, are 2264 and 73 nm respectively. These are in agreement with the direct measurements, well within their accuracy.

Next, we consider parameters extracted by the wedge-shaped envelope method. For both the high-fluence and low-fluence cases, this method results in values of thickness, $\overline{d}$, that are around 3% lower and values of refractive index, n, that are correspondingly 3% higher than for the OPE method. Considering that the film transmittance is between 0.98 and 0.99 for both cases, this agrees with our previous result for model films that indicated that the wedge-shaped envelope method gives errors of less than 5%. The film transmittance is still large enough for the extinction coefficient to be accurately estimated by this method. The extinction coefficient is found to be negative over most of the wavelength region and diverges further at short wavelengths. The thickness variation, Δd, has larger and more erratic errors. For the film deposited at high fluence where the wedge is significant, the error in estimating Δd is +25% for the wedge-shaped envelope method. For the film deposited at low fluence, the smaller $\overline{d}$ contributes to greatly increased error for Δd.

Finally, fitting the film parameters using the conventional envelope method results in thickness errors of +35% and +2% compared to the OPE method for the films deposited at high-fluence and low-fluence, respectively. For the two films considered, the variation in thickness for the high-fluence film is much greater than that of the low-fluence film. The conventional envelope method is not expected to be able to account for wedged samples properly. It is relatively more successful in estimating the extinction coefficient; however, it consistently predicts that the shrinkage of the transmission spectrum envelope is caused by absorption rather than by thickness variation, which can also reduce the transmission spectrum envelope. The result is an overestimate of the extinction coefficient as shown in Figs. 3.15(c) and 3.16(c). In general, when the non-uniformity is small, say about less than 20 nm, the conventional envelope method gives similar results to the OPE method.

Results for all the films tested are tabulated in Table 3.6 and the following is a summary of the relation of film parameters to deposition conditions. Refractive index does not show any specific trend with substrate temperature. But low laser fluence always produces films with a higher refractive index. The smallest extinction coefficient is 4.55×10^{-4} and is obtained at high laser fluence and a 300ºC substrate temperature. In general, low substrate temperatures produce smaller extinction coefficients. Increased film thickness naturally leads to larger non-uniformity that in turn results in reduced transmission spectra envelopes. The direct bandgaps of the AlN films were derived by fitting the derived absorption coefficient to the relation $\alpha h\nu = A(h\nu - E_g)^{1/2}$ and are shown in Table 3.6. High temperature and low fluence deposition give the largest bandgap energy that is close to that of bulk AlN (6.2 eV). This might imply that high substrate temperature and low laser fluence (low deposition rate) favor fewer defects in the film crystal structure. These aspects of film structure and properties will be addressed in a subsequent chapter.

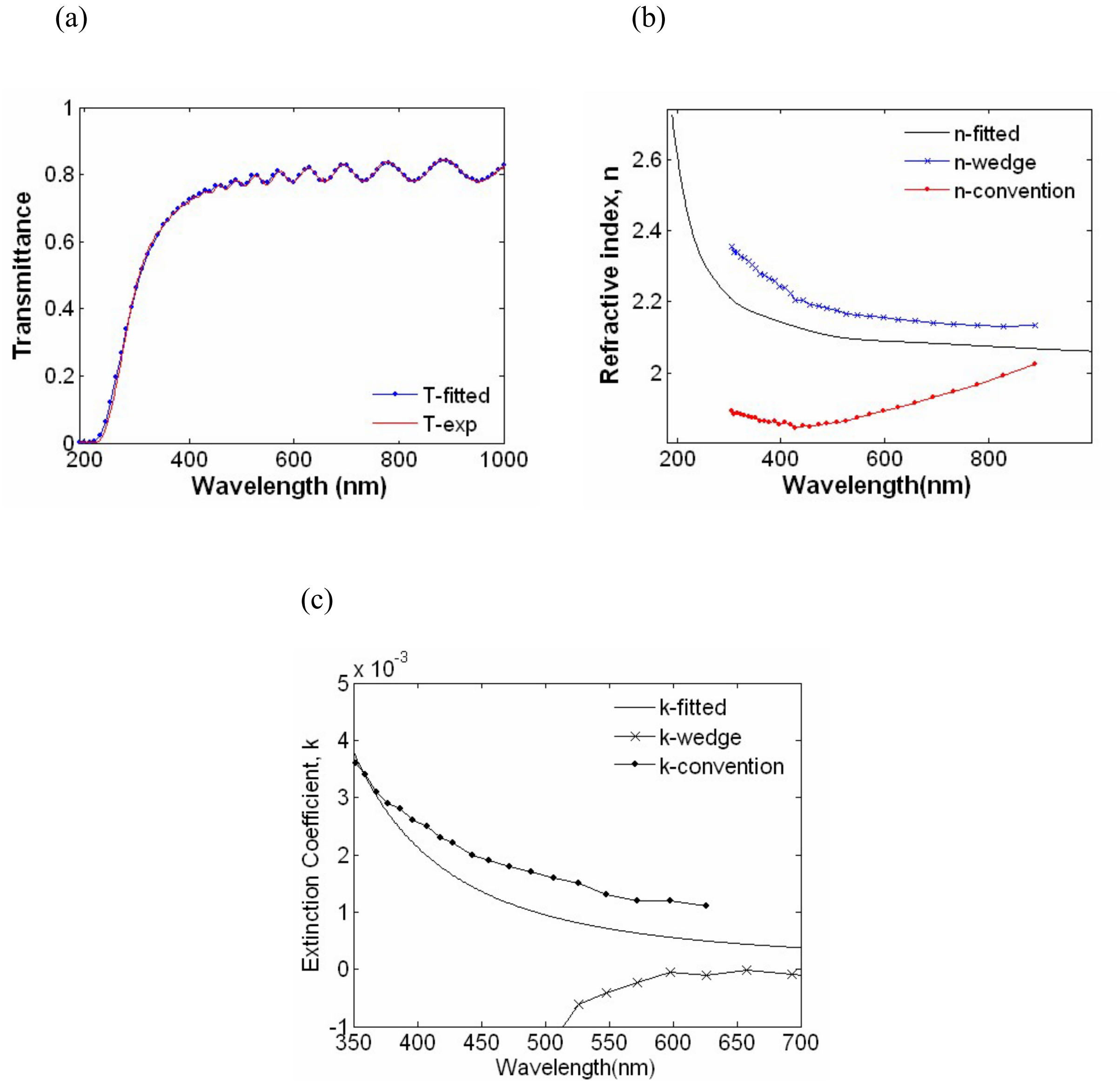

Figure 3.15. Optical properties of an AlN film deposited at high fluence and a 500ºC substrate temperature: (a) transmittance, (b) refractive index, and (c) extinction coefficient. Notation in the legends: exp (experimental measurement); fitted (the OPE method); wedge (wedge-shaped envelope method); convention (conventional envelope method).

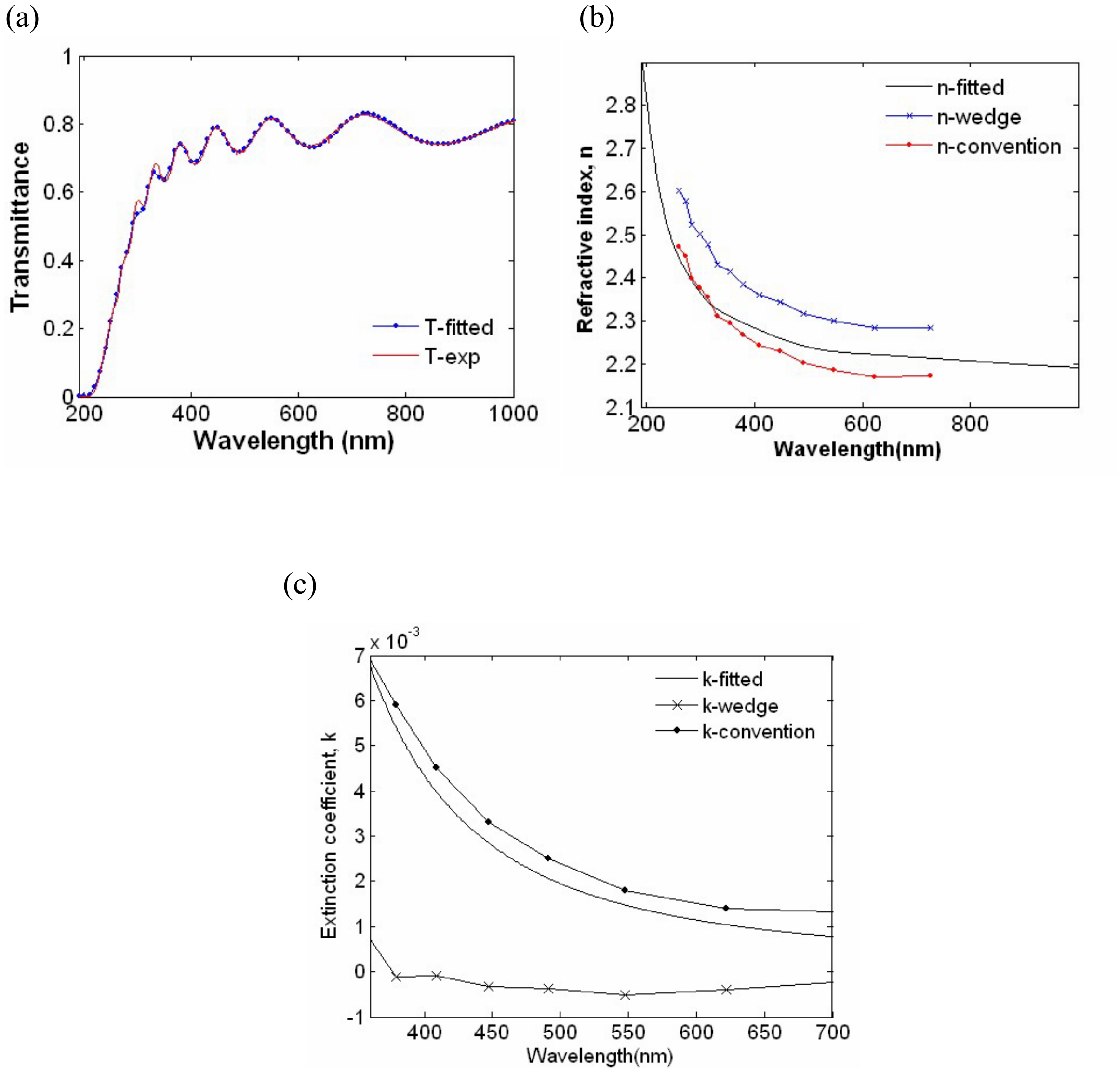

Figure 3.16. Optical properties of an AlN film deposited at low fluence and a 300ºC substrate temperature: (a) transmittance, (b) refractive index, and (c) extinction coefficient. Notation in the legends: exp (experimental measurement); fitted (the OPE method); wedge (wedge-shaped envelope method); convention (conventional envelope method).

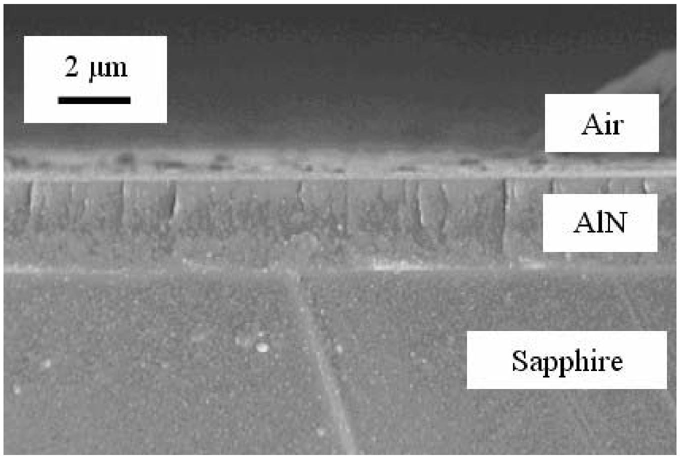

Figure 3.17 Representative cross-section SEM micrograph of an AlN film deposited at high fluence and a 100ºC substrate temperature.

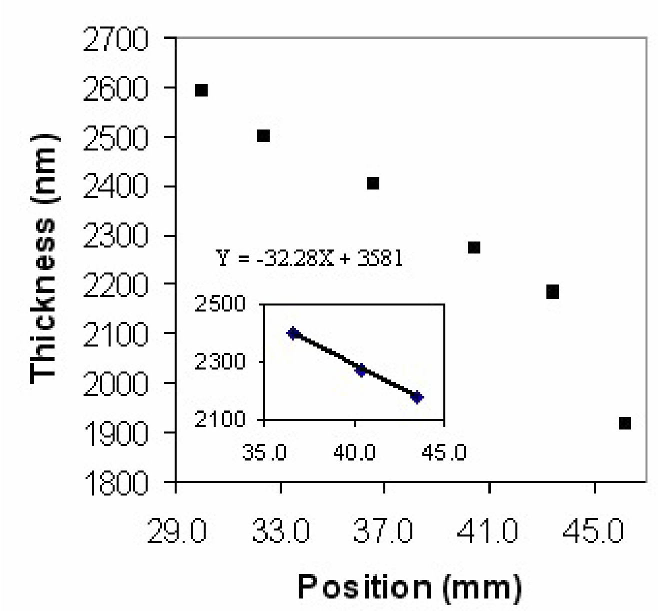

Figure 3.18 Thickness profile along the axis of the aperture for a fractured AlN film deposited at high fluence and a 100ºC substrate temperature. The inset shows the profile in the region of the 4 mm aperture centered at 40.4 mm and the linear regression fit to that data.

Sample	Method	d (nm)	Δd (nm)	n	k ($\times 10^{-4}$)
High fluence, 500°C, $\chi = 0.986$	OPE Method	1499	45	2.09	4.8
	Wedge-shaped method	1456	57	2.15	- 0.9
	Conventional method	1974	N/A	1.91	10.8
Low fluence, 300°C, $\chi = 0.990$	OPE Method	491	13	2.22	9.9
	Wedge-shaped method	477	28	2.28	- 3.9
	Conventional method	502	N/A	2.17	13.9

Table 3.5 Comparison of properties of AlN films determined by the OPE method, the wedge-shaped envelope method, and the conventional envelope method.

Film sample	T (°C)	n at 633 nm	k at 633 nm ($\times 10^{-4}$)	d (nm)	Δd (nm)	RMS meas. (nm)	E_g (ev)
High Fluence (3 – 12 J/cm^2)	100	2.06	6.38	2264	73	1.6	4.40
	300	2.01	4.55	1881	68	2.3	5.05
	500	2.09	4.81	1499	45	1.5	5.21
	700	2.07	8.20	1849	46	2.6	5.23
Low Fluence (0.7 - 3.0 J/cm^2)	300	2.22	9.9	491	13	0.5	5.62
	500	2.15	15.0	575	20	2.5	5.81
	600	2.15	17.9	392	8	1.0	5.88
	800	2.18	22.6	553	15	2.4	5.82

Table 3.6. Properties of AlN films analyzed by the OPE method. RMS surface roughness was measured by AFM as described in the text, and E_g was derived from the spectral dependence of the absorption coefficient.

3.14 Summary

We investigated film on substrate system and derived the numerical expression for the transmittance and reflectance without any approximation. We also have described a new method for extracting properties of wedged and absorbing thin films, including refractive index, extinction coefficient, and thickness, based only on a measurement of the transmission (or reflection) spectrum. This Optimum Parameter Extraction (OPE) method utilizes a combination of numerical optimization, efficient models of dispersive film parameters, and film transmission equations derived for wedged, non-uniformly thick, and absorbing films (having 2-D non-uniformity) measured through a rectangular aperture.

We also introduced a one-parameter, packing-density model for refractive index that requires measurement of the refractive index dispersion of the same or similar material. The Sellmeier equation was also shown to work, but with the disadvantage of having more parameters to fit.

The OPE method was found to accurately predict the values of optical constants for test cases that produced large errors when determined using previous methods. We showed that the OPE method could incorporate only 1-D non-uniformity in thickness and still converge rapidly and predict the values of optical constants accurately when a rectangular illumination area was used to record the transmission spectrum. It is also possible to include both 2-D wedge and non-uniformity in thickness if a stochastic algorithm such as a genetic algorithm were to be employed.

Usually, a hybrid algorithm which combines a stochastic algorithm with a deterministic algorithm is employed when the cost function has numerous local minima around global minimum. In this case, it would take longer to converge. Although we showed our OPE method in the case of transparent substrate and single film on substrate system, It can be generalized to any multiple layers using equation (3.1). The substrate does not have to be transparent and the system could be multi-layer sample. But for high precision, it is desirable that the information of only one layer should be extracted step by step.

A number of AlN films were also tested to compare the performance of the various methods. Using our OPE method, optical properties of AlN thin films were accurately determined, whereas the presence of absorption and thickness non-uniformity in the films resulted in large errors when other methods were used.

---

[1] Fujii, M.; Mimura, A.; Hayashi, S.; Yamamoto, K. Appl. Phys.Lett., **75**, 184 (1999)

[2] Bera, S. K.; Chaudhuri, S.; Pal, A. K. J. Phys. D: Appl. Phys., **33**, 2326 (2000)

[3] Zhou, J.; Li, L.; Gui, Z.; Buddhudu, S.; Zhou, Y. Appl. Phys. Lett., **76**, 1540 (2000)

[4] Bender, C. M.; Burtlich, J. M.; Barber, D.; Pollock, C. Chem. Mater., **12**, 1969 (2000)

[5] Russell J. Gehr, Robert W. Boy, Chem. Mater. **8**, 1807 (1996)

[6] J.E. Sipe and Robert W. Boyd, Physical Review A, **46**(3), 46 (1992)

[7] Robert W. Boy , Russell J. Gehr, Goerge L Fischert and J.E Sipe, Pure Appl. Opt. **5**, 505 (1996)

[8] L.-P. Wang, D. S. Shim, Q. Ma, V.R. Rao, E. Ginsburg, A. Talalyevsky, J. Vac, Sci. Technol. A **23**, 1284 (2005).

[9] Sancho-Parramon, J.; Modreanu, M.; Bassas, J. Proceedings of SPIE-The International Society for Optical Engineering, **5826**, 371(2005)

[10] Tigau, N.; Ciupina, V.; Prodan, G., Journal of Crystal Growth **277**, 529 (2005)

[11] R. J. Swanepoel, Phys. E: Sci. Instrum. **16**, 1214 (1983).

[12] D. E. Aspnes, "The Accurate Determination of Optical Properties by Ellipsometry," in *Handbook of Optical Constants of Solids*, edited by Palik E D (Academic, Orlando, 1985), p.89.

[13] E. A. Irene, Thin Solid Films **233**, 96 (1993).

---

[14] R. J. Swanepoel, Phys. E: Sci. Instrum. **17**, 896 (1984).

[15] E. Marquez, J.B. Ramirez-Malo., J. Fernandez-Pena, P.Villares, R . Jimenez-Garay, P.J.S. Ewen, and A.E. Owen, J. Non-Crystalline Solids **164-166**, 1223 (1993).

[16] E. Marquez, J.B. Ramirez-Malo., J. Fernandez-Pena, P.Villares, R . Jimenez-Garay, P.J.S. Ewen, and A.E. Owen, Optical Materials **2**, 143 (1993).

[17] R. M. A. Azzam and N. M. Bashara, "Ellipsometry and polarized light"(North-Holland Publsighing Co., 1977)

[18] In the literature cited on envelope methods for extracting thin-film parameters, this quantity is often referred to as absorbance. This terminology is not used here to be consistent with more widely used optics terminology and to avoid possible confusion.

[19] Hai Lu, William J. Schaff, Jeonghyun Hwang, Hong Wu, Goutam Koley, and Lester F. Eastman, Applied Physics Letters, Vol. 79, No. 10, pp. 1489–1491

[20] F. Hamdani, A. E. Botchkarev, H. Tang, W. Kim, and H. Morkoc, Appl. Phys. Lett. **71** (21), 311.

[21] Filmetrics Inc., San Diego, CA, USA, www.filmetrics.com.

[22] J. M. Gonzalez-Leal, R. Prieto-Alcon, M. Stuchlik. M. Vlcek. S.R. Elliott, E. Marquez, Optical Materials **27**, 147 (2004).

[23] TFCalc, software Spectra Inc., Portland, OR, USA (2003), www.sspectra.com

[24] Filmwizard, Scientific Computing Inc., Encinitas, CA, USA, www.sci-soft.com

---

[25] F. A. Jenkins and H. E. White, *Fundamentals of Optics* (McGraw-Hill, Auckland, 1981), p.482-6.

[26] B. Titan, Appl. Opt. **23**, 4477-85 (1984).

[27] A. R. Forouhi and I. Bloomer, Phys. Rev. B **34**, 7018 (1986).

[28] N. W. Ashcroft and N. D. Mermin, "The Drude theory of Metals," in *Solid State Physics* (Saunders, Fort worth, 1976), p.16.

[29] S. Cabuk and A. Mamedov, J. Opt. A: Pure Appl. Opt. **1**, 424 (1999).

[30] C. Rincon, S. M. Wasim, and G. Marin, J. Phys.: Condens. Matter **14**, 997 (2002).

[31] D. Brunner, H. Angerer, E. Bustarret, F. Freudenberg, R. Hopler, R. Dimitrov, O. Amvacher, and M. Stutzmann, J. Appl. Phys. **82**, 5090 (1997).

[32] J. I. Pankove, *Optical Process in semiconductors* (Prentice- Hall, Elgewood Cliffs, NJ, 1971), Chap. 3.

[33] R. Fletcher, and M. J. D. Powell, Computer J. **6**, 163 (1963).

[34] D. Goldfarb, Mathematics of Computing, **24**, 23 (1970).

[35] E. Marquez, J. B. Ramirez-Malo, P. Villares, R. Jimenez-Garay, and R. Swanepoel, Thin Solid Films **254**, 83 (1995).

[36] J.B. Ramirez-Malo, E. Marquez, C. Corrales, J. Fernandez-Pena, J. Reyes, P. Villares, and R. Jimenez-Garay, Materials Chem. and Phys.s **44**, 186 (1996).

[37] E. Marquez, J. M. Gonzalez-Leal, R. Jimenez-Garay, S. R. Lukic, and D.M. Perovic, J. Phys. D: Appl. Phys. **30**, 690 (1997).

---

[38] E. Marquez, A.M. Bernal-Oliva, J.M Gonzalez-Leal, R. Prieto-Alcon, A. Ledesma, R. Jimenez-Garay, and I. Martil, Materials Chem. and Phys. **60**, 231 (1999).

[39] M. McClain, A. Feldman, D. Kahaner, and X. Ying, Computers in Phys. **5**, 45 (1991).

[40] Filmetrics Inc., San Diego, CA, USA, www.filmetrics.com.

[41] R. D. Vispute, J. Narayan, H. Wu, and K. Jangannadham, J. Appl. Phys. **77**, 4724 (1995).

4

Fabrication and characterization of aluminum nitride thin films

4.1 Introduction

The construction of nanocomposites involves the intimate mixing of functional materials within a matrix that can be processed. Matrix materials can be polymers, polymer blends, glasses, ceramics or semiconductors. Optical transparency is the one of the most important characteristic for optoelectronic and photonic applications because it is directly related to optical loss. In this context, AlN thin film is an excellent candidate as an encapsulating material for optical nanocomposites due to its various unique properties. First, it has a wide band gap 6.2 eV and a small extinction coefficient which allows it to be used for applications in the ultra-violet (UV), visible and infra-red (IR) domain. In addition, it has high values of surface acoustic velocity, large dielectric constant, high temperature stability, and hardness. These characteristics make it ideally suited for use in a number of structural, optical, and electronic applications.[1, 2, 3, 4, 5, 6, 7] AlN also is a strong potential candidate for use in the fabrication of blue light emitting diodes (LED) because it can be alloyed with GaN to create AlGaN based optical devices. The combination of these characteristics of AlN makes its thin film a suitable candidate for protective optical coatings and surface passivating layers of GaN nanocomposite.

The goal of this chapter is to study correlations between optical properties, structural properties and the processing conditions of AlN films in order to exploit the feasibility of AlN thin film deposited by the PLD technique for nonlinear nanocomposites. Since our main objective was to produce films suited for an encapsulating layer of optical nanocomposites, processing conditions will be focused on producing films with good optical properties.

AlN thin films have been produced using many different methods including metalorganic chemical vapor deposition (MOCVD) [8] plasma-assisted molecular beam epitaxy (MBE) [9], reactive magnetron sputtering(RMS)[10] and pulsed laser deposition (PLD).[11] As described in chapter 2, PLD is particularly well suited to the production of AlN thin films for optical applications because of high deposition rates and efficient fabrication of high-quality, stoichiometric films at low deposition temperatures.[12] Although the influence of PLD processing parameters (laser fluence, substrate temperature, and ambient gas type and pressure) on the microstructure of AlN films have been studied previously, contradictory results have been reported. For example, some authors have reported that the highest quality films are produced under vacuum[13, 14, 15, 16], while others have reported that Al decomposition (nitrogen deficiency) occurs even at low fluence with a low background pressure of N_2 [17, 18, 19, 20, 21]. There are also discrepancies regarding the influence of substrate temperature or/and ambient pressure on deposition rate[22, 23, 24]. Thus, the critical process variables necessary to obtain optical-quality AlN films by PLD remain uncertain.

We have performed a series of experiments aimed at elucidating the critical processing parameters that influence the optical properties, crystal texture, and their correlation for AlN films deposited on sapphire substrates by PLD. AlN Films have been deposited by varying processing parameters including laser fluence, substrate temperature, gas pressure, and deposition rate. The films were then examined using various characterizing techniques.

PLD films are generally non-uniformly thick due to the narrow angular distribution of the plume [25] . This leads to significant errors in the derived determination of optical constants measured using conventional methods[26]. To avoid these errors due to the films' non-uniformity and accurately determine optical properties including extinction coefficient, refractive index and thickness, the spectroscopic results were interpreted using a novel numerical procedure (OPE method) that was explained in chapter 3 and elsewhere[27]. In this chapter, we for the first time, report for the dependence of both optical properties, structural properties, and their correlations for AlN films on sapphire substrates as a function of PLD processing parameters. We also explore the potential causes for discrepancies in results that have been reported previously.

4.2. Experiment

4.2.1 Deposition conditions

AlN films were deposited using a UHV vacuum system evacuated by a turbo-molecular pump to a base pressure of 1.0×10^{-8} Torr (1.3×10^{-6} Pa); a schematic diagram of the PLD system has already been shown in Fig. 3.17 of chapter 3. The PLD target was a rectangular, stoichiometric AlN slab with a purity of 99.99% fabricated by hot pressing (Sputtering Materials Inc., Reno, NV). The laser was brought into the chamber through a UV-fused silica window that was at a 60˚ angle relative to the target surface. For preparation of most of the samples, the target was placed 5.1 cm from the temperature-controlled substrate. However, for one set of the specimens, the target -to-substrate distance was increased to 12.3 cm in order to decrease the deposition rate without changing the other process conditions. Films were deposited onto sapphire (0001) substrates that were first degreased with acetone and methanol in an ultrasonic bath and then were heated to 900ºC in vacuum for 45 min. prior to deposition. Depositions were carried out at different ambient pressures ranging from 1.0×10^{-8} Torr to 4.5×10^{-4} Torr and substrate temperatures ranging from 100 to 900ºC for either 25 min or 50 min. Nitrogen with purity of 99.9% was used to control the gas pressure.

A KrF excimer laser (Lumonics PM-848), λ = 248 nm, PRF = 30 Hz, and τ = 14 ns, was used to ablate the target. The laser was focused to a 30 mm by 10 mm rectangle using a 32 cm focal-length lens. The eccentric lens was rastered over a 1.5 mm by 3 mm oval path to minimize the creation of a crater. However, this motion resulted in a non-uniform laser fluence because the size of the focus varied by a factor of approximately three, depending on position. Thus, the fluence is reported as a range in two regimes, low fluence with a range of 1-3 J/cm^2 and high fluence with a range from 4-12 J/cm^2.

A second factor that influences the laser fluence during PLD but which has not been considered previously is the gradual reduction in laser fluence that inevitably occurs as deposition occurs on the window to the chamber. To test the significance this effect in our chamber, we made a series of samples at fixed fluence, ambient pressure, and deposition time. We found that the transmission through the window decreased by 5-10% during a single deposition. Subsequently, to account for this effect, we calculated the on-target laser fluence after each deposition by measuring the transmission through the chamber window using UV-VIS spectroscopy and then adjusting the reported fluence values accordingly.

4.2.2 Characterization of the films

Mechanical profilometry was used to measure film thickness. The surface roughness was measured using atomic force microscopy (AFM). The cross sections of the films were also examined using scanning electron microscopy (SEM) to verify thickness and thickness variation. To measure film composition electron dispersive spectroscopy (EDS) was carried out. X-ray diffraction (θ-2θ) and rocking curve analyses were performed to determine the crystal structure and crystal texture of the films.

Optical transmission spectra of the films were acquired over wavelengths from 200 nm to 1000 nm (1.2 to 6.2 eV) using UV-VIS spectroscopy. Optical properties, including extinction coefficient, refractive index, and film thickness, were obtained from the spectra using a novel numerical method (OPE method) which accommodates variations in film thickness. The direct bandgaps of the AlN films were also determined from the optical data.

4.3 Results

Three sets of data are shown: 1) low fluence at high deposition rate, LFHD (1-3 J/cm^2, d =5.1 cm), high fluence at high deposition rate, HFHD (4-12 J/cm^2,d = 5.1 cm), and high fluence at low deposition rates, HFLD (4-12 J/cm^2, d = 12.3 cm).

4.3.1 Influence of pressure

The deposition chamber was evacuated to a pressure of 1×10^{-8} Torr and then back filled with N_2 to reach the final base pressure for deposition. Films were prepared at pressures of 1×10^{-8}, 4.5×10^{-7}, 4.5×10^{-6}, 4.5×10^{-5} and 4.5×10^{-4} Torr under both low and high fluence conditions. The substrate temperature for these experiments ranged from 300 to 900˚C.

Results from UV-Vis spectroscopy showed that the films deposited at low pressures (less than 4.5 x10^{-5} Torr) exhibited poor transmission (less than 50% at a wavelength of 633 nm), independent of the laser fluence and substrate temperature. In contrast all films produced at higher pressure (4.5×10^{-4} Torr) had good transmission (greater than 70%) independent of laser fluece intensity. The poor transmission for films deposited at low pressures has previously been attributed to decomposition of the AlN during PLD. [28, 29, 30,, 31] Decomposition results in the incorporation of excess Al or deficiency N in the films that is responsible for the dark grey coloration and poor transmission. The presence of metallic Al was verified by x-ray diffraction in our films produced at high fluence and at a base pressure of 1×10^{-8} Torr. Because of the poor transmission of all of the films produced at low pressure, further detailed analysis on these films was not performed and all of the remaining experiments were conducted on films produced at a nitrogen pressure of 4.5×10^{-4} Torr.

4.3.2 Influence of temperature, fluence and deposition rate

Since the on-target fluence could not be held constant as a result of deposition onto the chamber window and the associated absorption in the window, the influence of temperature, fluence and deposition rate could not be analyzed independently. Thus, to determine the influence of each of these variables, the data were analyzed using independent linear regression with temperature, fluence and deposition rate as the independent variables or using multiple linear regression[32] to simultaneously fit two parameters (temperature and fluence or temperature and deposition rate) as independent variables.

Multiple linear regression was applied when more than one processing parameter was varied. Since it allows the relative influence of each variable to be determined even when individual variables have different measurement scales through standardized regression, coefficient, “beta (β)”. Beta (β) is the regression coefficients of the same variables when they are converted to same scale. It is useful to compare the relative explanatory power of different independent variables especially when individual variables have different measurement scales.

The F statistic or the F-observed value was used to determine whether the observed relationship between the dependent and independent variables occurs by chance. The result of the F-test is indicated by “F” value and "significance F". If the F-observed value is substantially greater than the F-critical value, the regression equation is useful in predicting the assessed value. The value of "Significance F" displayed depends on the results of the regression analysis and the confidence level chosen in the regression analysis dialog box. Normally, for a confidence level of 95%, if "Significance F" is <0.05, then the null hypothesis is rejected (there is a statistically significant association between the dependent and independent variables). Conversely, if "Significance F" is >0.05, then the null hypothesis is accepted (there is no statistically significant association between X and Y).

T-test is another useful hypothesis test that will determine whether each slope coefficient is useful in estimating the assessed value of the dependant variables. If the absolute value of t is greater than t-critical value, the corresponding variable is an important variable when estimating the assessed value of the dependant variables. Each of the other independent variables can be tested for statistical significance. The t-observed values and the associated P value also were acquired for each of the independent variables.

4.3.2.1 Composition of films

The composition of the films at high pressure (4.5 x10^{-5} Torr) was measured using SEM EDS. However, because the substrates in our experiments were Al_2O_3, the absolute concentration of the films could not be determined quantitatively from this measurement in either plan view or cross sections because the electron beam penetrated through the film into the substrate and thus the signal for Al came from both the film and substrate.

4.3.2.2 Crystal structure

In Fig 4.1, x-ray diffractions patterns (θ-2θ) are shown as a function of temperature and nominal fluence. For the films deposited at high fluence (Fig 4.1 (a)), the patterns show a single peak that is attributed to AlN along with a peak associated with the sapphire substrate at $2\theta = 41.8^\circ$. At low deposition temperatures, the AlN peak corresponds to (100) but as the temperature is increased, there is a transition to an (002) texture. Similarly, for films deposited at low fluence (Fig 4.1 (b)), there is also only one peak present that is attributed to AlN. However, all of the films deposited at low fluence exhibit an (002) texture, independent of the deposition temperature. No other peaks were present in the films deposited at either high or low fluence, confirming the absence of metallic Al in the films.

Although the intensity of the diffraction peaks has been used previously as a measure of the degree of crystalline texture present in AlN films, direct comparisons should not be ascertained from a (θ-2θ) patterns alone because the intensity of the peaks may be affected by 1). film thickness, 2). crystallite size, and 3). misorientation of the film relative to the substrate. All of these factors likely occur as a result of variations in laser fluence, substrate temperature and deposition rate that occur during deposition by PLD.

(a)

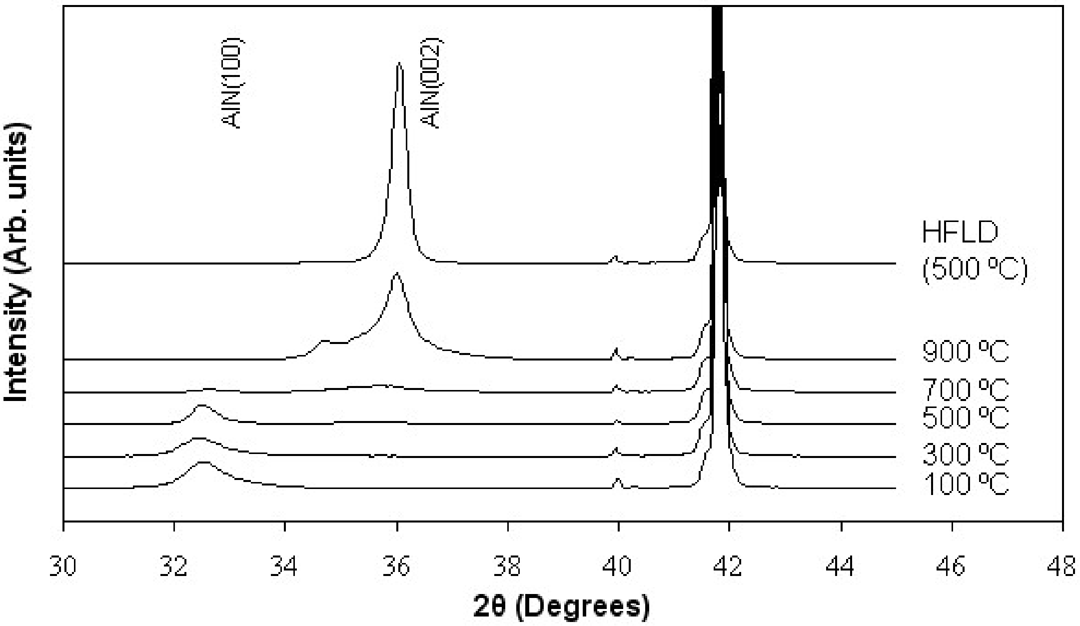

(b)

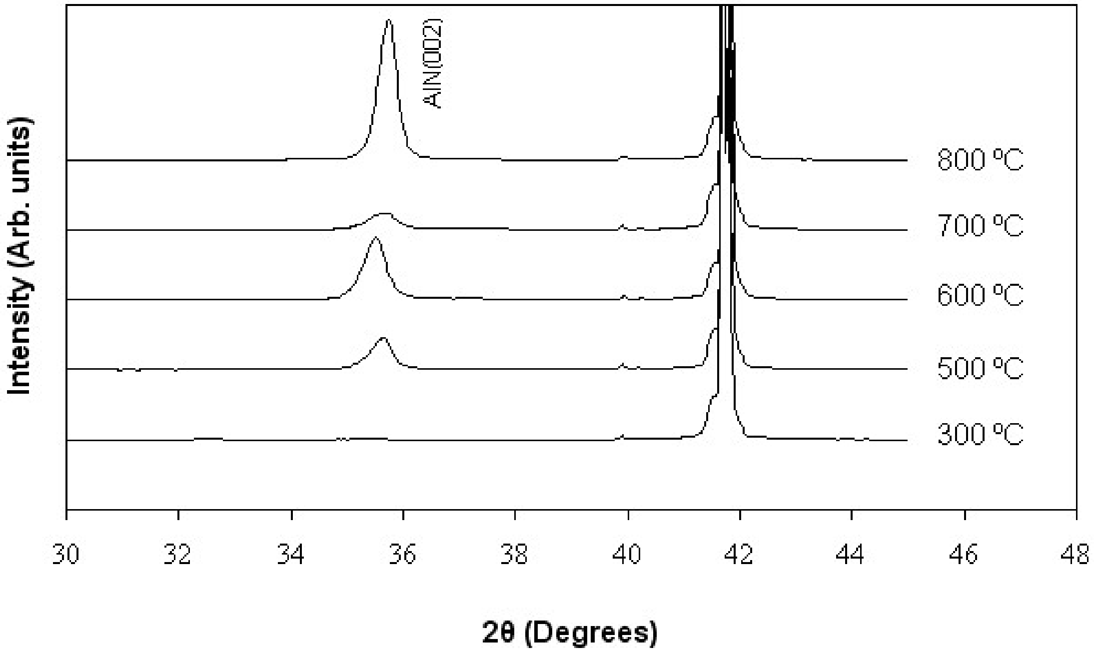

Figure 4.1. X-ray scans obtained from AlN films deposited at various temperatures, (a) high fluence and (b) low fluence

4.3.2.3 Crystallographic texture

The degree of texture in the films was measured using a rocking curve analysis. In Fig 4.2 (a), the (002) rocking curves are shown for films deposited at high fluence at temperatures between 500-900˚C. Similarly, the rocking curves for the films deposited at low fluence are shown in Fig 4.2 (b). There are no obvious systematic trends in the data when performing either independent and multiple regression. We found little correlation between FWHM (a full-width half maximum) values and the processing parameters.

The rocking curves have a full-width half maximum (FWHM) of 1-14˚ and are shifted slightly from the origin. From the breadth of the rocking curves it is clear that all of our films are polycrystalline but are strongly textured with a preferred crystallographic orientation with respect to the substrate. The shift from the origin indicates that the growth orientations of the grains in some of the films are tilted slightly (up to ±5˚) with respect to the substrate.

Previously, it has been reported that single crystal AlN can be deposited at low temperatures by PLD [33,34]. However, an examination of the rocking curves reported for these films deposited onto sapphire and silicon shows that they exhibit FWHM of several tenths of a degree to several degrees, depending on deposition temperature. Since the experimentally measured FWHM for a single crystal with a smooth flat surface is typically of order 0.03˚ [35], the previous results are not consistent with single crystal AlN; based on these results we believe that these films were likely polycrystalline for samples produced at temperatures of 800˚C or below. At a deposition temperature of 850˚C, the FWHM was reduced to 0.07˚ which indicates that single crystals may be possible at high deposition temperatures. In a subsequent study, where the crystal orientation was examined by a combination of x-ray diffraction, TEM, and AFM, showed that AlN deposited on sapphire at 920˚C may be single crystal but that at lower temperatures the films are polycrystalline and textured[36]. Our results appear to be consistent with this finding for AlN films produced under similar processing conditions.

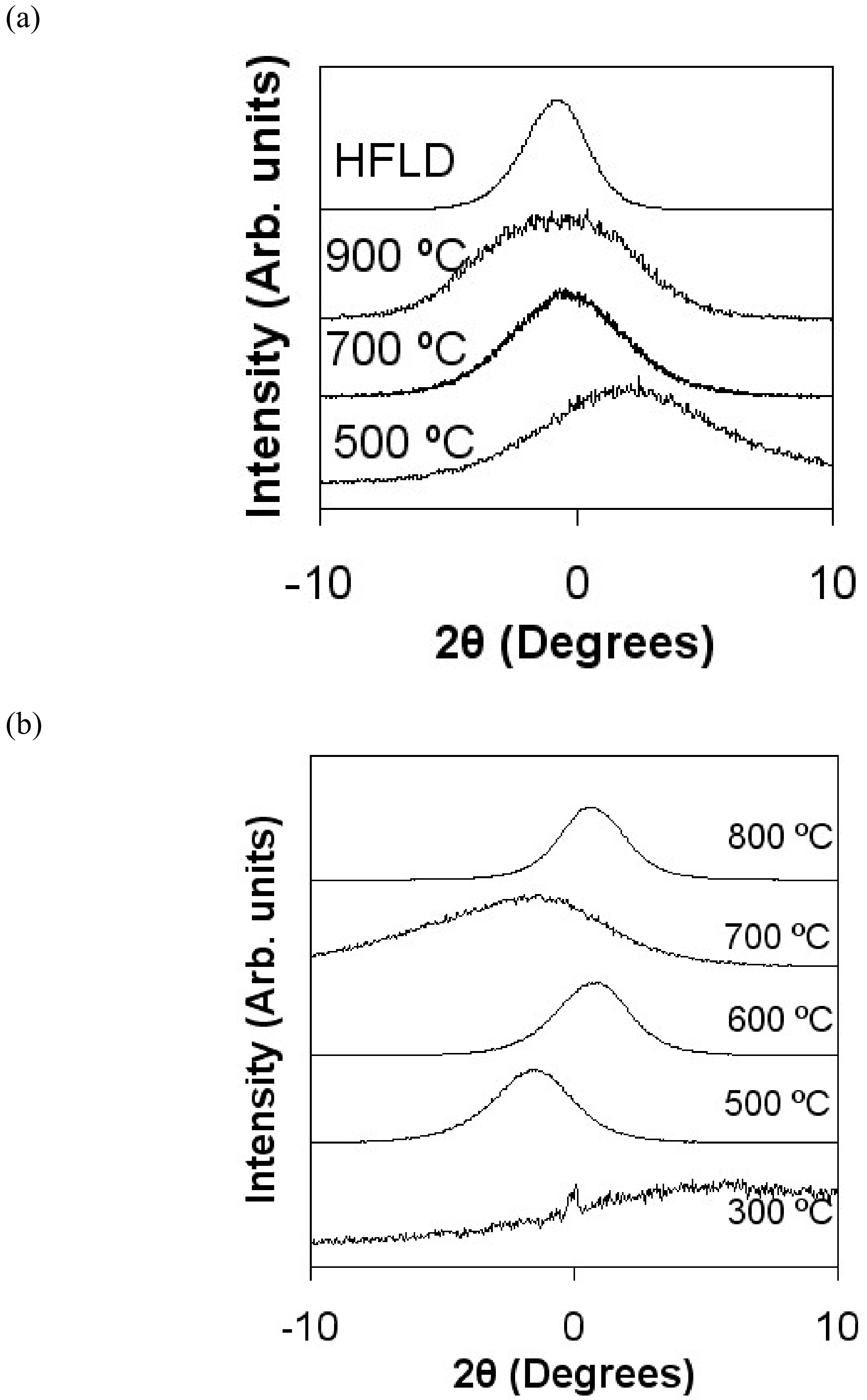

Figure 4.2. X-ray rocking curves obtained from AlN films deposited at various temperatures, (a) high fluence and (b) low fluence

4.3.2.4 Surface roughness

The surface roughness was analyzed over a 2 μm × 2 μm area using atomic force microcopy (AFM); results are shown in Table 4.1 (a), (b) and Fig. 4.3. As is typical for PLD-produced films, the RMS roughness values are quite small (< 3nm, compared to the substrate RMS < 0.3nm). Performing both independent and multiple regressions, we found little correlation between the RMS roughness values and the deposition temperature or fluence. However, from Table 4.1 (a), (b), it is apparent that the lowest values of surface roughness are consistently obtained in the thinnest samples. This correlation between deposition rate and surface roughness is also consistent with previous observations that show surface roughness increases with film thickness because the gain size is increased as the film thickness increases.[37,38,39,40]. Since deposition time was a fixed variable in each regime, this also implies that the surface roughness increases with deposition rate. Typical measurements of the film surface profile by an AFM image were shown in Fig 4.4.

(a)

High Laser Fluence (HF)						
Temperature (ºC)	100	300	500	700	900	HFLD (500)
Maximum Laser Fluence (J/cm^2)	12.2	10.5	7.8	9.6	8.7	10.5
Deposition rate (nm/min)	45	38	30	37	33	5
FWHM of <002> rocking curve	N/A	N/A	8.4	5.3	6.9	2.9
RMS Roughness (nm)	1.6	2.3	1.5	2.6	1.9	0.4
n at 633nm	2.06	2.08	2.09	2.07	N/A	2.07
k (×10^{-4}) at 633nm	6.4	4.6	4.8	8.2	N/A	19.9
t (nm)	2264	1881	1499	1849	1667	261
Δt (nm)	73	68	45	46	N/A	2
Bandgap (ev)	4.4	5.1	5.2	5.2	5.4	5.9

(b)

Low Laser Fluence (LF)					
Temperature (ºC)	300	500	600	700	800
Maximum Laser Fluence (J/cm^2)	2.0	2.4	1.8	2.8	2.2
Deposition rate (nm/min)	20	23	16	31	22
FWHM of <002> rocking curve	13.9	3.7	3.4	8.2	3.0
RMS Roughness (nm)	0.5	2.5	1.0	2.1	2.4
n at 633nm	2.22	2.15	2.15	2.10	2.18
k ($\times 10^{-4}$) at 633nm	9.9	15.0	17.9	20.0	22.6
t (nm)	492	575	392	786	553
Δt (nm)	13	20	8	27	15
Bandgap (ev)	5.6	5.8	5.9	5.6	5.8

Table 4.1. (a) the properties of HFHD and HFLD (b) the properties of LFHD

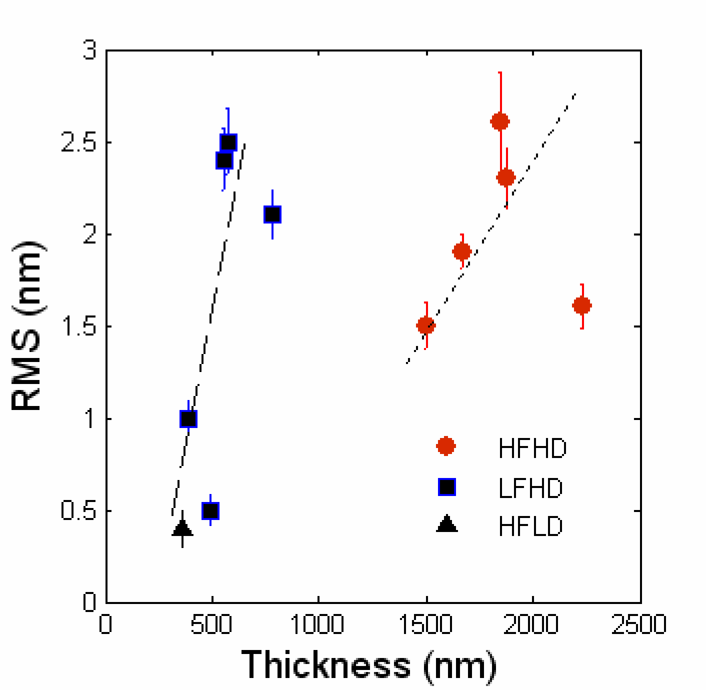

Figure 4.3 RMS surface roughness of AlN films versus film thickness measured from 2 × 2 µm atomic force microcopy (AFM) scans.

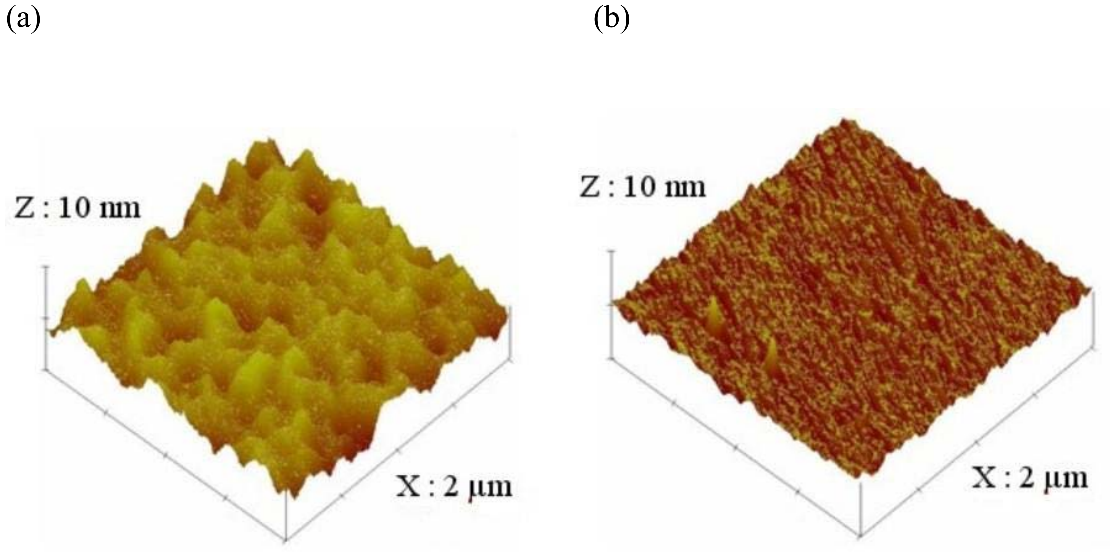

Figure 4.4 Measurements of the film surface profile by an AFM image of (a)AlN deposited at high fluence with a substrate temperature of 500ºC and (b) AlN deposited at low fluence with a substrate temperature of 300ºC.

4.3.2.5 Optical properties

To accurately determine optical properties for films with thickness variations, we have recently developed a numerical method that can be applied successfully to extract films properties from UV-Vis transmission spectra, even when the films are wedge-shaped and somewhat absorbing. The following is a brief description of the optimum parameter extraction (OPE) method. We begin with a realistic dispersion model for refractive index and extinction coefficient. We then use a numerical fitting technique where we attempt to minimize the difference between the experimental and numerically-derived transmission spectra by adjusting the variables considering the effect of thickness variation.

Typical results are presented in Fig. 4.5 for representative films produced at high fluence and low fluence showing the best fit, numerically derived transmittance spectra using the OPE method overlaid over the experimental data (Fig. 4.5 (a)), and the numerically determined refractive index (Fig. 4.5 (b).) and extinction coefficient (Fig. 4.5 (c)). The sample prepared at 900 ºC and at high fluence was excluded from optical analysis because it was strongly absorbing and the OPE method could not be used in this case.

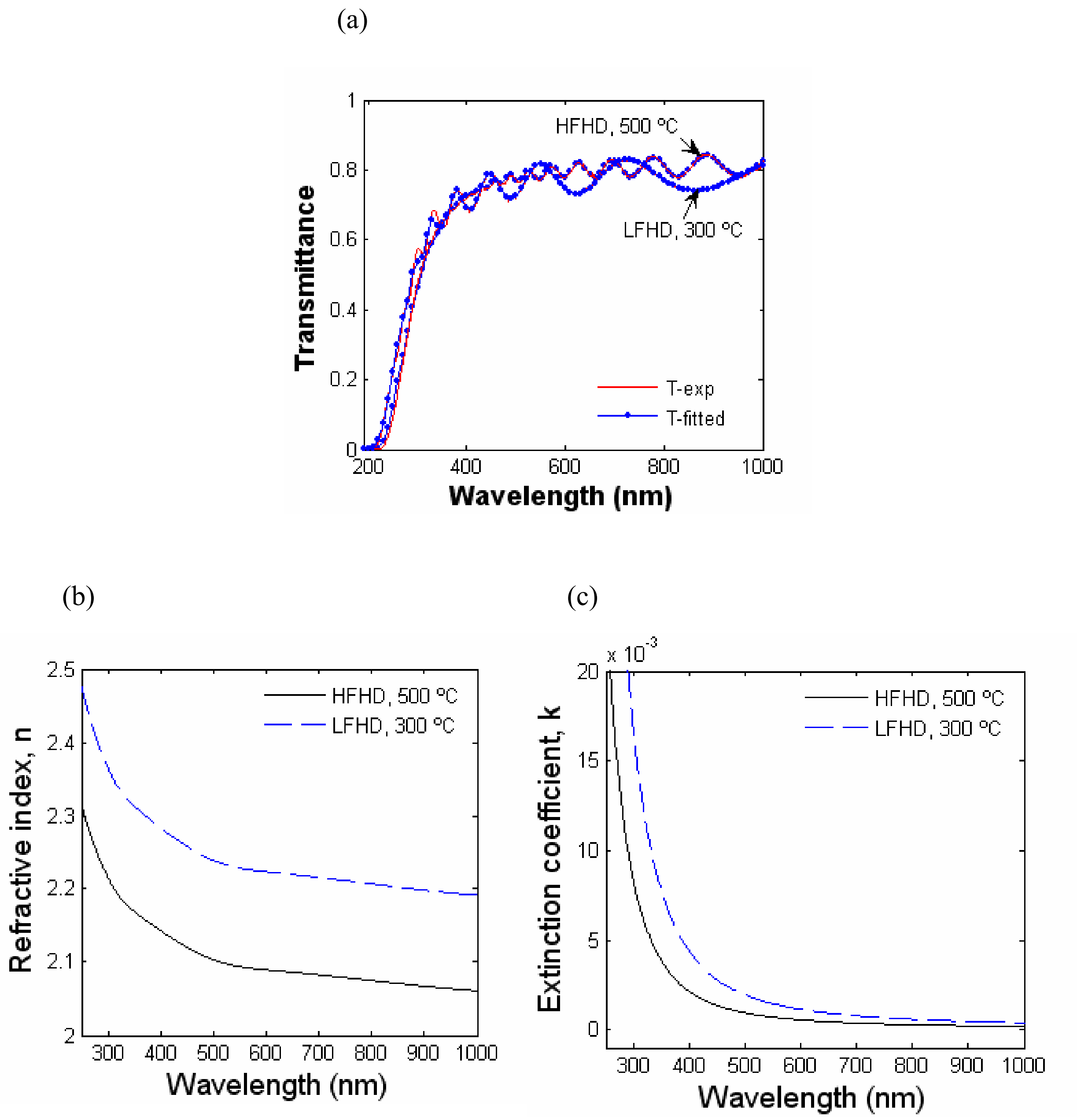

Figure 4.5 Optical properties versus wavelength for AlN films deposited at high fluence, 500ºC substrate temperature and at low fluence, 300ºC substrate temperature: (a) transmittance; experimental (T-exp) and fitted by the OPE method (T-fitted), (b) refractive index, and (c) extinction coefficient.

4.3.2.5.1 Refractive index

The OPE method was used to extract the optical properties from the spectra; Fig. 4.6 shows the refractive indexes at a wavelength of 633 nm versus substrate deposition temperatures. The refractive indexes are 2.074 ±0.011 (0.5 %) for the samples produced at high fluence and 2.160 ±0.044 (2%) for samples produced at low fluence. The films produced at low fluence consistently have a higher refractive index than those produced at high fluence. The sample produced at high fluence but low deposition rate (HFLD) exhibit a refractive index similar to that produced at high fluence but high deposition rate (HFHD). This confirms that the refractive index depends on laser fluence rather than simply deposition rate and substrate temperature. There does not appear to be a systematic trend between substrate temperature and the refractive index within the resolution of the OPE method (2%). This result is consistent with the findings of other studies with similar resolution limitations [41, 42].

4.3.2.5.2 Extinction coefficient

Fig. 4.7 shows the extinction coefficient, k, versus temperature. From this plot, it is clear that films deposited at high fluence and low substrate temperatures have a lower extinction coefficient (i.e. are more transmissive) than those deposited at low fluence and high substrate temperature. Contrary to previous suggestions[41,42], we did not find a correlation between extinction coefficient and crystalline texture. In fact, the samples that had the lowest extinction coefficient were produced at low substrate temperatures and were polycrystalline with relatively poor alignment of the grains to the substrate.

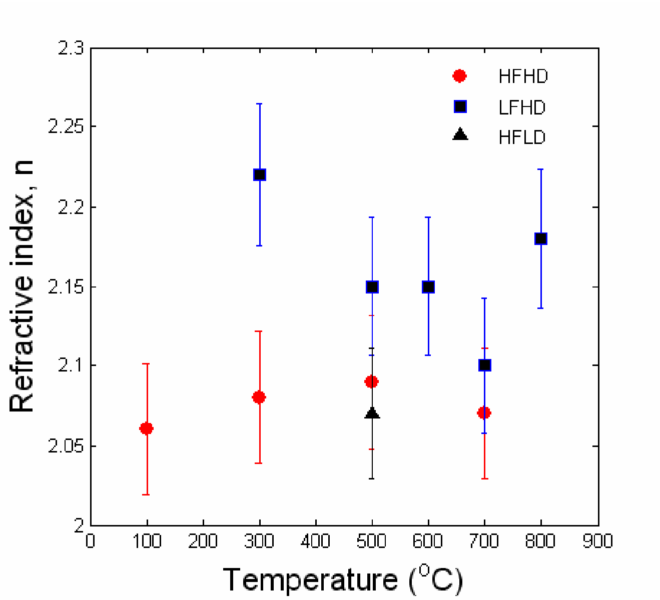

Figure 4.6 Refractive index (n) versus temperature for AlN films deposited at high and low fluence.

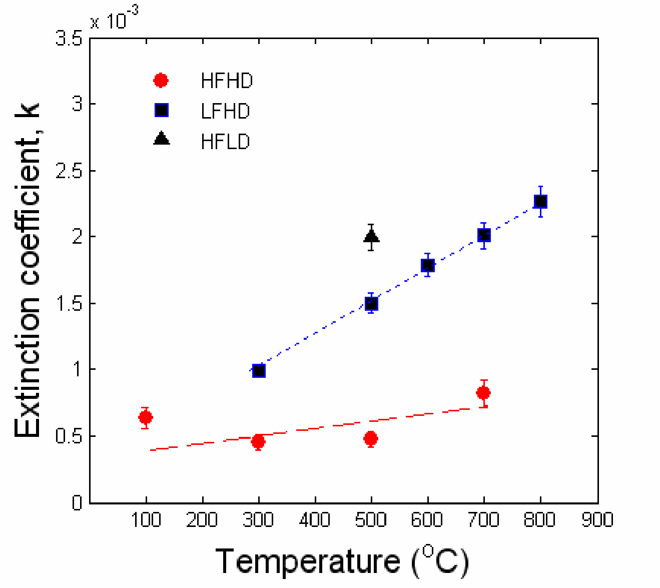

Figure 4.7. Extinction coefficient (k) versus temperature for AlN films deposited at high and low fluence.

4.3.2.5.3 Bandgap

The direct bandgap, E_g, of the films was determined by fitting the absorption coefficient, α, to the well- known relation

$$\alpha h\nu = A(h\nu - E_g)^{1/2} \tag{4.1}$$

where α is related to k by $k = \alpha\lambda / 4\pi$, A = arbitrary proportionality factor, h = Planck's constant (6.62607×10^{-34}, J.s) and ν = frequency . Figure 4.8 (a) and 4.8 (b) are plots of E_g versus temperature and deposition rate, respectively. Figure 4.8 clearly shows that E_g increases with temperature and decreases with deposition rate, although for samples deposited at low fluence the dependence of both parameters on temperature is rather weak. The maximum values of E_g for our films approached 6.0 eV, which is close to the bulk value (6.2 eV).

Multiple regression was initially performed with the independent variables of temperature and fluence. However an even stronger correlation was observed when temperature and deposition rate were used as the independent variables. The results of the multiple linear regression are shown in Table 4.2. The adjusted R^2 value for samples deposited at high fluence was very high (0.92) but was low for samples deposited at low fluence (0.28). Although a low value of adjusted R^2 could indicate E_g is not strongly dependent on temperature and deposition rate for the samples deposited at low fluence, low values of adjusted R^2 could also result if E_g varies non-linearly with temperature and/or deposition rate. This is possible in this case because the bandgap at low fluence is very close to the value for bulk AlN (6.2 eV). Thus, for samples deposited at high fluence, when E_g is far from bulk value, E_g may vary linearly with temperature and deposition rate and accordingly exhibit very high adjusted R^2 values (high fluence) whereas at low fluence the bandgap may begin to plateau near the bulk value and therefore exhibit a low value of adjusted R^2. Based on the beta values shown in Table 4.2, bandgap depends more strongly (with a negative correlation) on deposition rate and less strongly (with a positive correlation) on temperature.

(a)

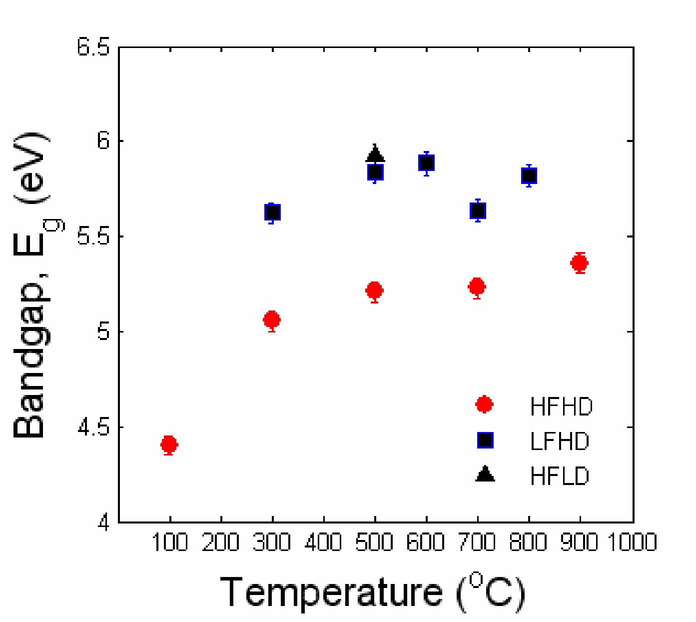

(b)

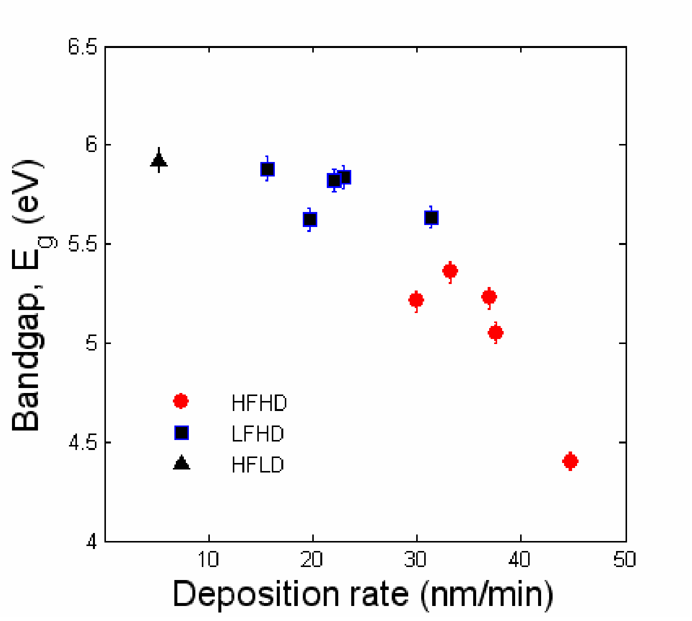

Figure 4.8. Bandgap (Eg) versus (a) temperature and (b) deposition rate for AlN films deposited at low and high fluence.

	HFHD + HFLD			LFHD			All Samples Grouped		
Adjusted R square, N samples	0.92, 6			0.28, 5			0.82, 11		
F stat, Significance F	31.06, 0.01			1.76, 0.36			31.06, 0.01		
	β	t stat	P-value	β	t stat	P-value	β	t stat	P-value
Temp.	0.41	3.20	0.05	0.57	1.38	0.30	0.37	3.01	0.02
Deposition rate	-0.81	-6.21	0.01	-0.66	-1.69	0.23	-0.79	-6.43	0.0002

Table 4.2. Results of multiple linear regression for bandgap

4.4 Summary and discussion

Aluminum nitride films were grown using PLD onto sapphire (0001) substrates using varying processing conditions (temperature, nitrogen pressure, and laser fluence). As our objective was to produce films with good optical properties, they will be discussed first and then crystal structure and their relationships will follow.

The films deposited at low nitrogen pressures (less than 4.5×10^{-5} Torr) exhibited, without exception, poor optical transmission, independent of the laser fluence and substrate temperature. In contrast, all films produced at higher nitrogen pressure (4.5×10^{-4} Torr) exhibited high transmission ($k = 0.5 - 2.5 \times 10^{-3}$). We can speculate that a critical pressure exists between 4.5×10^{-5} Torr and 4.5×10^{-4} Torr, above which the film transparency becomes high.

All of our films were deposited using nitrogen of 99.9% purity. Of the films deposited at the higher nitrogen pressure, those deposited at low substrate temperatures had a lower extinction coefficient than those deposited at higher substrate temperature (up to 800°C). Our results show unambiguously that high quality films with high optical transmission can be deposited by PLD without resorting to high temperatures or UHP (ultra-high purity) processing conditions. Although all of our films were polycrystalline, we found that, contrary to previous reports[43] this did not significantly effect transmission because of the fine grain size in the films. In fact, the samples that had the lowest extinction coefficient were produced at low substrate temperatures and had relatively poor alignment of the grains to the substrate.

When analyzing the variation of extinction coefficient, k, versus temperature and fluence shown in Fig. 4.7, one notices that k is larger for the thinner films (i.e., all those deposited at lower laser fluence). These films deposited at lower fluence had a stronger dependence on temperature but generally about the same physical thickness. This behavior is inconsistent with bulk absorption in the AlN film. However, it is consistent with absorption arising from a thin absorbing layer whose absorption increases with temperature but is independent of AlN film thickness. The possibility of a very thin surface oxide layer contributing to the measured absorption will be discussed later.

The bandgap was derived from these absorption measurements. We found that bandgap increased with both temperature and deposition rate. In multiple regression analysis, deposition rate was found to have a stronger influence on bandgap than temperature. This would imply that high substrate temperature and low deposition rate favor fewer band-edge defects in the film, but that these defects do not correlate with absorption at visible wavelengths.

Refractive index, on the other hand, showed little systematic dependence on processing parameters except for the observation of higher index values (nearer the bulk value) for deposition at low fluence. This result is consistent with previous reports for AlN films deposited by r.f magnetron sputtering.[44] It is possible that small systematic variations in refractive index may occur, but if these variations are less than the measurement error of 2%, they would not be observed.

Our extensive X-ray diffraction measurements of the films' structure showed that at high fluence and low deposition temperatures, the grains were of (100) orientation, but as the temperature was increased, there was a transition to a (002) texture. All the films deposited at low fluence exhibited a (002) texture. Although the grains exhibited a preferred texture, grain orientations were broadly distributed in angle (up to 14° FWHM) and the mean orientations of the preferred axes were tilted with respect to the substrate by up to ±5°, depending on sample processing conditions. We observed no correlation between the degree of texture and the optical properties. However, the variation in the texture orientation observed across a sample might make a weak dependence impossible to observe. This variation in texture orientation measured across a sample deposited at 900°C was observed to correlate with the visible variation in its brownish color (opacity).

Finally, we consider the possibility of an oxide layer on the films' surface and how it might contribute to the observed extinction coefficient behavior that is inconsistent with bulk absorption in the film. Such a thin oxide layer, ~10 nm, would be invisible to optical diagnostics (except for its overall absorption) and its thickness could not be obtained from other surface spectroscopies. Its thickness would depend mainly on substrate temperature and oxidation time. Thus, the samples deposited at the same temperature probably have oxide layers of similar thickness and therefore similar optical absorption irrespective of fluence. As a result, the extinction coefficient extracted by the OPE method for thicker films is relatively less affected by the oxidation layer absorption. All of the low fluence (thinner) samples had higher extracted extinction coefficients than the high fluence (thicker) samples at same substrate temperature and thus were more affected by the oxide thickness (increasing with deposition temperature). The brownish color of the samples prepared at 900 ºC can be attributed to more severe surface oxidation as the oxidation kinetics accelerate rapidly at this temperature. This result appears to be consistent with the oxidation of AlN films observed by many other authors (Lee et al[45] and Kolodzey et al[46]). Yue et al[47] reported finding that there was already a very thin oxidation layer in the surface region of AlN at room temperature, and Chowdhury et al[48] showed that below 1000ºC, the rate of oxidation was relatively slow but increasing above this temperature. We can conclude that the surface oxidation rate of our AlN films increased dramatically between 800 and 900 ºC and begin to show its brown color in the samples deposited at 900ºC. Any subtle correlation between AlN film extinction coefficient and crystal properties was probably not found due to the dominant absorption of the surface oxidation layer. Localization of the majority of the absorption in the oxidation layer does place an upper limit on the AlN film absorption, and indicates that the extinction coefficient in the AlN films was remarkably low ($< 5\text{x}10^{-4}$ at 633 nm).

In conclusion, we report that low optical absorption, textured polycrystalline AlN films can be produced by PLD on sapphire substrates at both low and high laser fluence using a background nitrogen pressure of 4.5×10^{-4} Torr at 99.9% purity.

Further investigation of the AlN film's optical absorption for deposition at high temperatures would require the use of UHP gas in order to prevent film surface oxidation during the cool-down time following deposition.

---

[1] S. Strite and H. Morkoc, J. Vac. Sci. Technol) **B10**, 1237 (1992).

[2] H. Morkoc, S. Strite, G.B.Gao, M.E. Lin,B. Sverdlov and M. Burns, J. appl. Phys. **76**, 1363 (1994). And references therein.

[3] R.F Davis, Porc. IEEE, 702, (1991).

[4] M.T Duffy, C.C. Wang, G.D. O'Clock, Jr. S.H. MacFarlance III, and P.J. Zanzucchi, J. Electron. Mater **2**, 359 (1973).

[5] L.M. sheppard, Am. Ceram. Soc. Bull. **71**, 1801 (1990).

[6] T.Y. Sheng, Z.Q. Yu, and G.J. Collins, Appl. Phys. Lett. **52**, 576 (1988).

[7] Y.X. Wang, Y.A. Li, and W. Feng W.Q. Lia, C.H. Zhao,L.H. Liu, K.C. Feng, Y.N. Zhao, Applied Surface Science **243**, 394-400 (2005).

[8] P. Kung, A. Saxler, X. Zhang, D. Walker, T.C. wang,, I. Furguson, and M. Razeghi, Appl. Phys. Lett **66**, 2958 (1995).

[9] K. S. Stevens, A. Ohtani, M. Kinniburgh, and R. Beresford, Appl. Phys. Lett. **65**, 321 (1994).

[10] W. J. Meng, J. Heremans, and Y.T. Chang, Appl. Phys. Lett. **59**, 2097 (1991).

[11] R. D. Vispute, J. Narayan, H. Wu, and K. Jangannadham, J. Appl. Phys. **77**, 4724 (1995).

[12] G.K. Hubler, in *Pulsed Laser Deposition of Thin Films*, edited by D.B. Chrisey and G.K. Hubler (Wiley-interscience, New York, 1994), and references therein.

[13] R.D Vispute, J. Narayan, Hong Wu and K. Jagannadham, J. Appl. Phys. **77**, 4724 (1995).

---

[14] R.D Vispute, Hong Wu, and J. Narayan, Appl. Phys. Lett. **67**, 1549 (1995).

[15] Ravi Bathe, R.D Vispute, Dan Habersat, R.P. Sharma, T. Venkatesan, C.J. Scozzie, Matt Ervin, B.R. Geil, A.J. Lelis, S.J. Dikshit, and R. Bhattacharya, Thin Solid Films **398-399**, 575 (2001).

[16] J. Keckes, S Six, J.W. Gerlach, and B. Rauschenbach, Journal of Crystal Growth **262**, 119-23 (2004).

[17] Carmen Ristoscu, Ion N. Mihailescu, Michalis Velegrakis, Maria Massaouti, Argyro Klini, and Costas Fotakis, Jounal of Applied Physics **4**, 2244-2250 (2003).

[18] Eniko Gyorgy, Carmen Ristoscu, I. N. Mihailescua, Argyro Klini, N. Vainos, C. Fotakisc, C. Ghica, G. Schmerber, and J. Faerber, Jounal of Applied Physics **90**, 456-61 (2001).

[19] H. Esrom, J. Y. Zhang, and A. J. Pedraza, Mater. Res. Soc. Symp. Proc. **236**, 383, (1992).

[20] M. J. DeSilva, A. J. Pedraza, and D. H. Lowndes, J. Mater. Res. **9**, 1019 (1994).

[21] S. Cao, A. J. Pedraza,, and L. F. Allard, J. Mater. Res. **10**, 54 (1995).

[22] R.D. Vispute, V. Talyansky, R.P. Sharma, S. Choopun, M. Downers, T. Venkatesan, Y.X. Li, L.G. Salamanca-Riba, A.A. Iliadia, K.A. Jones, and J. McGarrity, Applied Surface Science **127-129**, 431 (1998).

[23] S. Six, J.W. Gerlach, and B. Rauschenbach, Thin Solid Film **370**, 1-4 (2000).

[24] M. Tabbal, P. Merel, M. Chaker, and H. Pepin, Eur. Phys. J. AP **14**, 115-9 (2001).

[25] R. K. Singh, O. W. Holland, and J. Narayan, J. Appl. Phys. **68**, 233 (1990)

---

[26] R. J. Swanepoel, *Phys. E: Sci. Instrum.* **17**, 896 (1984).

[27] Jonghoon Baek, Desiderio Kovar, John W. Keto, and Michael F. Becker, Applied Optics **45**, 1627 (2006). .

[28] Carmen Ristoscu, Ion N. Mihailescu, Michalis Velegrakis, Maria Massaouti, Argyro Klini, and Costas Fotakis, Jounal of Applied Physics **4**, 2244-2250 (2003).

[29] Eniko Gyorgy, Carmen Ristoscu, I. N. Mihailescua, Argyro Klini, N. Vainos, C. Fotakisc, C. Ghica, G. Schmerber, and J. Faerber, J. OF Applied Physics **90**, 456-61 (2001).

[30] H. Esrom, J. Y. Zhang, and A. J. Pedraza, Mater. Res. Soc. Symp. Proc., 236, 383, (1992).

[31] S. Cao, A. J. Pedraza,, and L. F. Allard, J. Mater. Res. **10**, 54 (1995).

[32] Edwards, Allen Louis, "Multiple regression and the analysis of variance and covariance"(San Francisco), (1979)

[33] R.D Vispute, J. Narayan, Hong Wu and K. Jagannadham, J. Appl. Phys. **77**, 4724-28 (1995).

[34] R.D Vispute, J. Narayan, J.D. Budai, Thin solid Films **299**, 94-103 (1997).

[35] Cullity, B. D.; Stock, S. R."Elements of X-Ray Diffraction, 3rd Edition", (Prentice Hall, Upper Saddle River, N. J.) 664 (2001).

[36] M. Tabbal, P. Merel, M. Chaker, and H. Pepin, Eur. Phys. J. AP **14**, 115 (2001).

[37] P. Tyagi and A.G. Vedeshwara, Eur. Phys. J. AP **19**, 313 (2002) :

---

[38] S. B. Ren, C. J. Lu, J. S. Liu, H. M. Shen, and Y. N. Wang, Physical review B **54**, 15 (1996).

[39] Y. Sakashita and H. Segawa, J. Appl. Phys. **73**, 7857 (1993)

[40] M. de Keijser, G.J.M. Dormens, P.J. VanVeldhoven, and D.M. de Leeuw, Appl. Phys. Lett. **59**, 3556 (1991)

[41] W.Y, Chiu, C.H. Wu, H. L. Kao, and Erik S.jeng. J. Vac. Sci. Technol. A **20** 843(2002)

[42] Li-peng wang, Dong S. Shim, Qing Ma, and valluri R. Rao. J. Vac. Sci. Technol. A **23** 1284 (2005)

[43] W. J. Meng, in *Properties of Group III Nitrides*, edited by J. H. Edgar (INSPEC Short Run Press Ltd., London, 1994), pp. 22–34.

[44] Han-Yong Joo, Hyeong Joon Kim, Sang Jung Kim, and Sang Youl Kim, J. Vac. Sci. Technol. A **17**, 862-70 (1999).

[45] J.W. Lee, I. Radu, M.Alexe, Journal of Electronic materials **13**, 131 (2002),

[46] J. Kolodzey, E. A. Chowdhury, G. Qui, and J. Olowolafe, Appl. Phys. Lett. **71**, 3802 (1997) ,

[47] Ruifeng Yue, Yan Wang, Youxiang Wang, Chunhua Chen, Applied Surface Science **148**, 73–78 (1999)

[48] Chowdhury, Enam Ahmed, Dashiell, M, Qiu, G, Olowolafe, J O, Journal of Electronic Materials **27,** 918 (1998)

5

Nanocomposite and their nonlinear optical properties

5.1 Motivation

Nonlinearity is important in various fields of science and technology, especially for optical communication. Faster and more sensitive optical devices are necessary to increase data communication speeds. A high-speed device has also been of interest as a sampling tool for measurement of various optical signals in such areas as time-resolved spectroscopy and characterization of high-speed optical components and systems. Further, because the time scale of interest becomes shorter than the limited response time of the fastest electro-optic devices, optical devices which rely on nonlinear optical phenomena are being actively pursued in a variety of systems such as organic and inorganic crystals, polymers and fullerenes[1,2,3.] In order for all optical techniques to find a wider application, it would be favorable to use the highly efficient nonlinearity of semiconductors and metals. Semiconductor and metal based devices are promising due to their compactness, robustness, and high compatibility with existing technology. However, they are not yet practical because of the limitations of existing nonlinear materials. Materials with large optical nonlinearity and fast response time are essential for future optical device application. Therefore, we need to find and develop materials that, at the same time, present large nonlinearities and satisfy various other technological and economical requirements.

Over the past decade, there has been much scientific activity in the synthesis and study of nanocomposites. Work to develop composites containing particles with diameters in the range of one to several tens nanometers, has became a major interdisciplinary research area. There have been many reports which have shown that when material dimensions are decreased to the nanometer scale, new phenomena occur that were not present on larger scales. In particular, the nonlinear optical response of nanoparticles and nanocomposites clearly distinguish themselves from the corresponding "bulk" material. The differences in properties are due not only to their atomic-like structure but also their interface and surface structures. [4] Consequently, intensive investigations on the nonlinearity of nanoparticles and nanocomposites recently have been carried out. Concurrently, nanocomposites formed by semiconductor or metal nanoparticles embedded in dielectric hosts have been intensively studied because the enclosing matrix (mostly thin films) imparts processability which benefits silicon-based technologies. Semiconductor fabrication processes will help create new ways to make highly sensitive, accurate and practical nono-composite devices for various applications. As such, nanocomposite are of practical interest as the final form of these novel materials.

In this chapter, we discuss the actual fabrication technique used to make semiconductor and metal nanocomposites. The theory for LAM (Laser Ablation of Microparticle) and PLD (Pulsed Laser Depostion) was previously discussed in chapter 2. In addition, the characterization of the second harmonic generation (SHG) and third harmonic generation (THG) is discussed.

It should be noted that all samples in chapter 5 were fabricated by the author, Jonghoon Baek and SHG and THG signal were measured by the coworker, David Stoker. Therefore, some of figures in chapter 5 were also used in David Stoker's thesis[5]. However, all interpretations were unique and made by the author, Jonghoon Baek.

5.2 Theoretical background

5.2.1 Nonlinear optical effect for high irradiance beam

The oscillating electromagnetic field of a light wave incident on a polarizable medium deflects the electrons from their equilibrium positions and leadsing to oscillating dipoles in the medium. These oscillating dipoles induce a macroscopic polarization P which leads to the refracted and reflected light wave. In the framework of linear optics, the deflection of electrons can be described as a harmonic oscillation becasuse the external field strength involved is much smaller than the intra-atomic field strength. In such a case, the polarization P is proportional to the incoming electric field E. The proportionality constant χ depends on the properties of the irradiated material and is called the susceptibility. For high irradiances, polarization responds nonlinearly to electric field.

$$\begin{aligned} P &= \chi^{(1)}E + \chi^{(2)}E^2 + \chi^{(3)}E^3 + \ldots \\ &= P^{(1)} + P^{(2)} + P^{(3)} + \ldots \end{aligned} \tag{5.1}$$

where P, E and $\chi^{(n)}$ denote induced polarization of medium, electric field and nth order nonlinear susceptibility respectively.

Therefore, in the framework of nonlinear optics, the induced polarization is written as a power expansion of the electric field. The nonlinear polarization terms in Eq. (5.1) serve as a source for the generation of new waves oscillating at frequencies 2ω, 3ω, 4ω, 5ω etc. They are called higher harmonic generation terms. For bulk solids, $\chi^{(1)}$ is of the order 1, $\chi^{(2)}$ is about eight orders of magnitude smaller ($\sim 10^{-8}$ esu) and $\chi^{(3)}$ is another seven orders of magnitude smaller ($\sim 10^{-15}$ esu). Therefore, to observe higher harmonic generation, the irradiance beam should be in the order of the intra-atomic field strength. It is possible today because ultrashort lasers with high power are readily available.

5.2.2 Second harmonic generation

Among the examples of $\chi^{(2)}$ processes, second harmonic generation (SHG) is the most typical phenomenon, illustrated schematically in Fig. 5.1. Here a laser beam whose electric filed strength is represented as

$$E(t) = E\exp^{-i\omega t} + c.c. \tag{5.2}$$

is incident upon a nonlinear media infor which the second-order susceptibility $\chi^{(2)}$ is nonzero. The second order polarization that is created in such a nonlinear media is given as

$$P^{(2)}(t) = 2\chi^{(2)}EE^{*} + (\chi^{(2)}E^{2}\exp^{-i2\omega t} + c.c) \tag{5.3}$$

We see a contribution at frequency 2ω. Therefore, this second order polarization can lead to the generation of radiation at the second-harmonic frequency. One common use of second harmonic generation is to convert the output of a fixed frequency laser to a different spectral region.

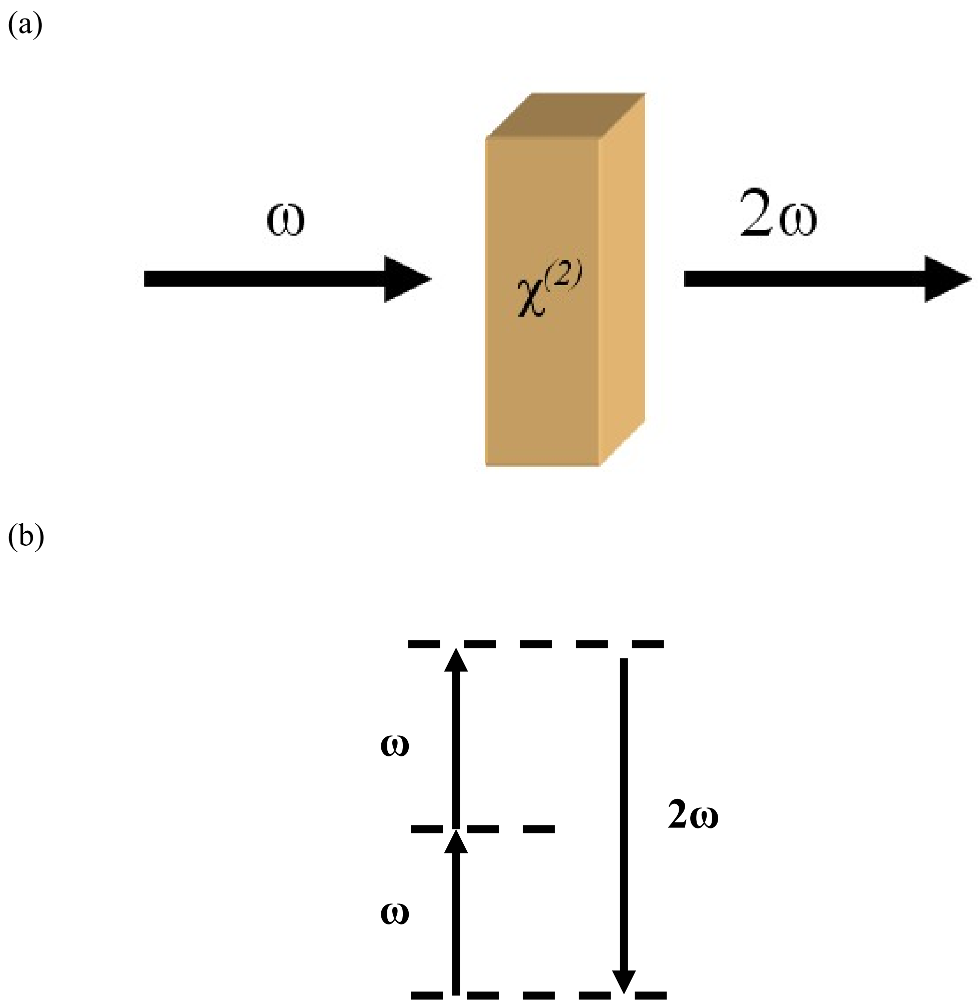

Figure 5.1 (a) Geometry of second-harmonic generation. (b) Energy-level diagram describing second harmonic generation.

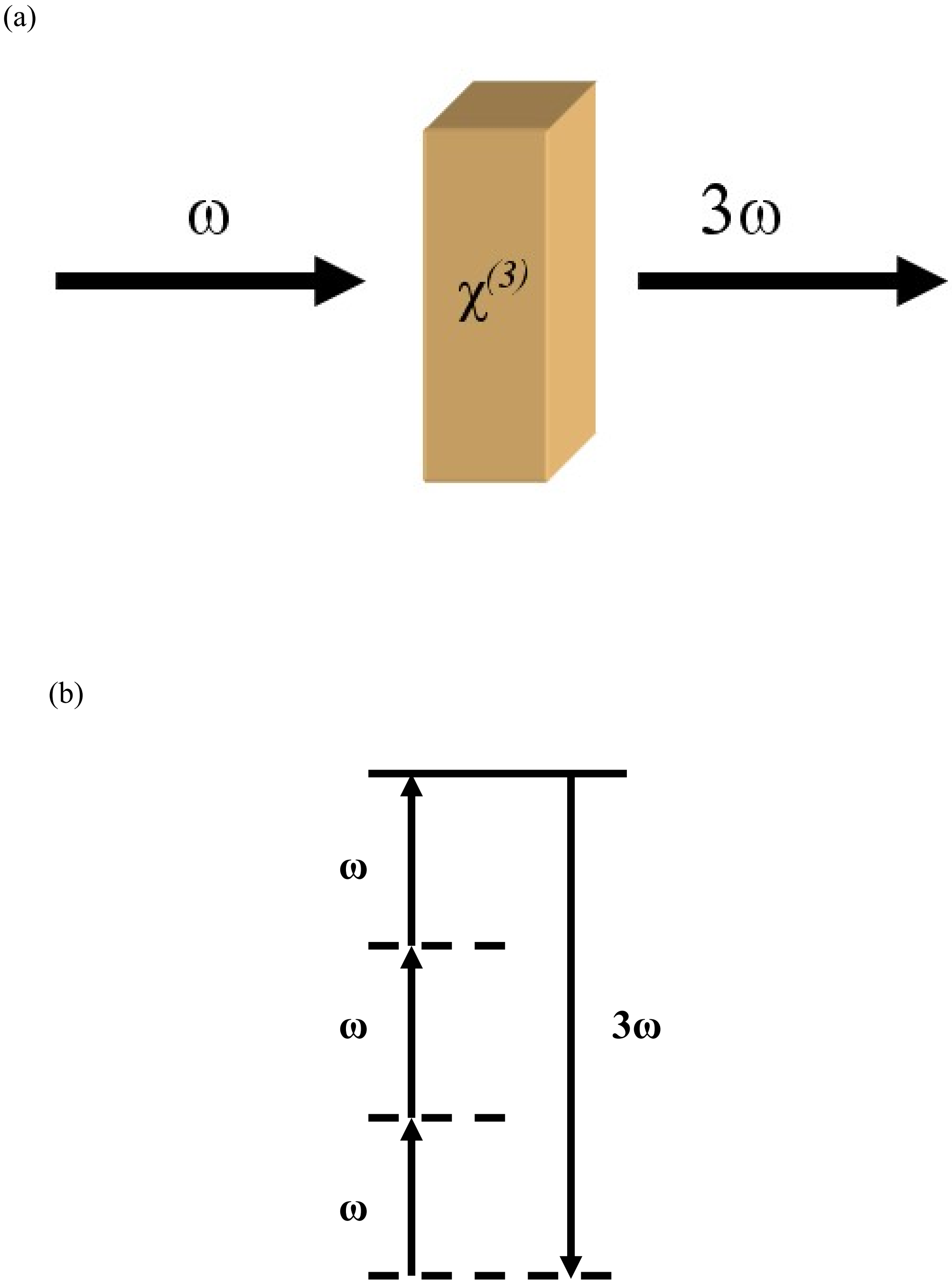

Figure 5.2 (a) Geometry of third harmonic generation. (b) Energy-level diagram describing third harmonic generation.

5.2.3 Third harmonic generation

Similarly, third harmonic generation (THG) is the simplest case among examples of $\chi^{(3)}$ processes, which is illustrated schematically in Fig. 5.2. The third order polarization that is created in a nonlinear media is given as

$$P^{(3)}(t) = \chi^{(3)} E^3 \exp^{-i3\omega t} + c.c \tag{5.4}$$

Eq (5.4) describes a response at frequency 3ω. This term leads to third harmonic generation, which is illustrated in Fig. 5.2 (a), (b). The photon description of this process is shown in Fig 5.2 (b). Three photons ω are destroyed and one photon of frequency 3ω is created in each elementary event.

5.2.4 Quantum confinement effect

An exciton is the term used to describe the electron-hole pair created when an electron leaves the valence band and enters the conduction band. Excitons have a natural physical separation between the electron and the hole that varies from material to material. The average separation is called the exciton Bohr radius. In a large semiconductor crystal, the exciton Bohr radius is small compared to the crystal, and the exciton is free to wander throughout the crystal. When crystal size (R) is smaller than exciton Bohr radius and exciton behavior is confined by its size, different linear and nonlinear properties change from bulk values. We call it a “quantum confinement effect” (QCE). Regimes of quantization of the exciton can be divided into two regions, such as weak confinement (R » R$_B$) and strong confinement(R « R$_B$). Here, R$_B$ is the exciton bohr radius. The exciton Bohr radius is given as

$$R_B = \frac{\hbar^2 \varepsilon}{\mu\, e^2} \tag{5.5}$$

where $\hbar, \varepsilon, \mu, e$ denote the reduced Planck constant, permittivity, reduced mass and electron charge.

It has been reported that a large enhancement of $\chi^{(3)}$ is observed in particles with sizes smaller than an exciton bohr radius.[6,7,8,9] However, the exact mechanism is not still clear.

5.2.5 Particle plasmons in metal and local field enhancement

The electron plasma in a metal can be geometrically constrained, the simplest example being small spherical particles, giving rise to quantized states. Such bound plasma oscillations are called localized surface plasmons or particle plasmons. For small particles in an applied electromagnetic field, the conduction electrons will move with the field creating a displacement compared to the positive ion background, which then acts as a restoring force. If the particle is spherical and its diameter is much smaller than the wavelength, it can be modeled as a dipole with the proportionality constant.[10]

$$\alpha(\omega) \propto \frac{\varepsilon(\omega) - \varepsilon_m}{\varepsilon(\omega) + 2\varepsilon_m} \tag{5.6}$$

where *ε(ω)* denotes the frequency dependent dielectric function of the nano particle, ε_m the dielectric constant of the surrounding medium. An applied static electric field induces a dipole moment *p* in a metal nanoparticle, which is proportional to the field strength E. Therefore, the proportionality constant is called electric polarization or polarizability.

$$p = \alpha(\omega)E(\omega) \propto \frac{\varepsilon(\omega) - \varepsilon_m}{\varepsilon(\omega) + 2\varepsilon_m} E(\omega) \tag{5.7}$$

The polarizability α(ω) shows a resonance behavior. Resonance is obtained whenever the real part of the denominator becomes zero.

$$\mathrm{Re}\{\, \varepsilon(\omega_{res}) + 2\varepsilon_m \,\} = 0 \tag{5.8}$$

where ω_{res} denotes the resonance frequency.

It shows resonance is achievable just for negative values of the real part of ε(ω). This is the reason for the exceptional role of the noble metals Ag, Au and Cu for particle plasmon excitation: their real part Re{ε(ω)} fulfills the resonance condition in Eq.(5.8) at specific light frequencies. The resonance frequency ω_{res} depends on the dielectric constant of the surrounding medium. Therefore, controlling ε(ω) allows in principle to tune the resonance frequency ω_{res} of the particle plasmon oscillation. An increasing ε_m leads to a red shift of the resonance wavelength.

In the near-field region of a metal particle, the electric field is significantly enhanced at the plasmon resonance frequency, which is called local field enhancement. The field enhancement f is defined as

$$f = \frac{|E|}{|E_0|} = f(r, \lambda) \qquad (5.9)$$

where E denotes the optical electric field at the observation point r and E_0 denotes the incoming field. The field enhancement f is a function of the position in the particle near-field *r* as well as the wavelength λ of the exciting light. In nanosized metal, f is mainly determined by polarizability in eq (5.8). Therefore, the field enhancement becomes

$$f \propto \alpha(\omega) \propto \frac{\varepsilon(\omega) - \varepsilon_m}{\varepsilon(\omega) - 2\varepsilon_m} \qquad (5.10)$$

As a consequence, a large enhancement of nonlinearity in metal nanoparticle is expected at the resonance wavelength.

Note also that, although Eq 5.6 is considered for only metallic nanoparticles, the derivation is valid in general, i.e. the constituents may be pure dielectrics as well. However, huge polarizability of pure dielectrics can not be achieved because the real part of the denominator never becomes zero in Eq 5.6 contrary to metal nanoparticles.

Field enhancement factor f with wavelength in silver nanoparticles and GaN nanoparticles is calculated and shown in Fig 5.3 (a) and (b) respectively. In bare Ag nanoparticles field enhancement factor f is enhanced resonantly at 350 (nm). In Ag nanoparticle coated by $NdAlO_3$ resonance frequency was redshifted by $NdAlO_3$ coating (see Fig 5.3(a)). Fig 5.3(b) shows field enhancement factor of GaN nanoparticles and GaN nanoparticles coated with AlN. It shows no resonant behavior. On the contrary to silver nanoparticles, it reduces local field due to similar dielectric constant ($\varepsilon_{GaN} / \varepsilon_{AlN}$ at 633 nm = 1.3). This simulation clearly shows that the resonance behavior of local field enchantment is possible only in some noble metal nanoparticles such as silver, gold and copper.

(a)

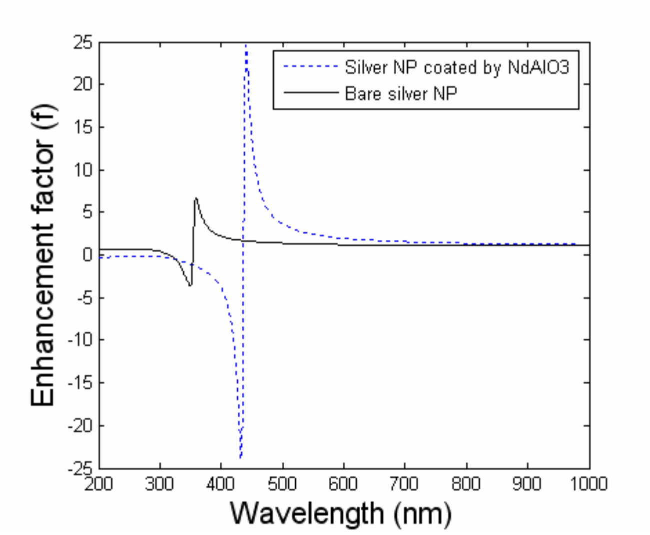

(b)

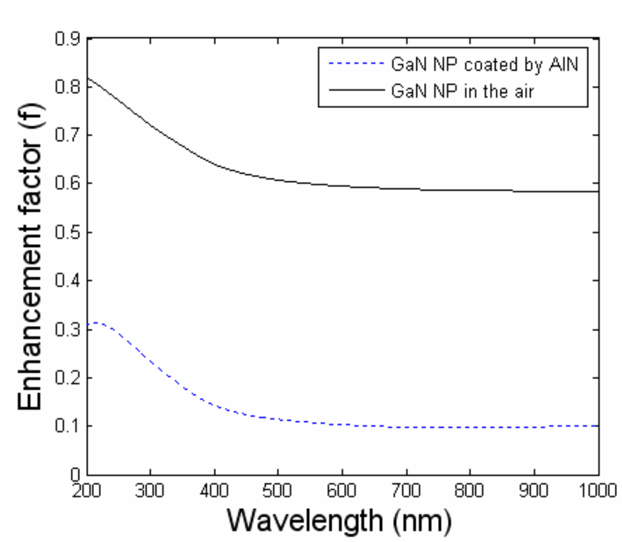

Fig 5.3 (a) Local field Enhancement factor versus wavelength of bare silver nanoparticles (solid) and silver nanoparticles coated by $NdAlO_3$ (dashed) (b) Local field Enhancement factor versus wavelength of bare GaN nanoparticles (solid) and GaN nanoparticles coated by AlN (dashed).

5.3 Experimental techniques for measuring of SHG and THG signal

The SHG and THG measurements of the materials were performed by direct measurement as shown in Figure 5.4. This is easy and simple method for measuring $\chi^{(2)}(-2\omega, \omega, \omega)$, $\chi^{(3)}(-3\omega, \omega, \omega, \omega)$. The laser pump source was an unamplified Ti:Sapphire oscillator (KMLabs), with 800 nm central frequency. The pulses are 40 fs, 30 nm FWHM, 7.5 nJ/pulse with an 85 MHz repetition rate. The laser was tightly focusd with a 2 cm f.l. lens. We measured the depth of focus, z_r, to be 75 μm in air, and calculated, assuming Gaussian beam profile, a waist radius of 4.4 μm. The sample is shot with a high intensity beam at the fundamental frequency and the transmitted power of the second harmonic signal (2ω) and third harmonic signal (3ω) was recorded using an Optical Multichannel Analyzer (Princeton Research Model 1420). The sample is mounted on a microstepper. Rso recording the harmonic signal as a function of microstepper position allowed for us to map the two dimensional harmonic response of the material. More detailed information of laser scanning apparatus is reported in David Stoker's dissertation.

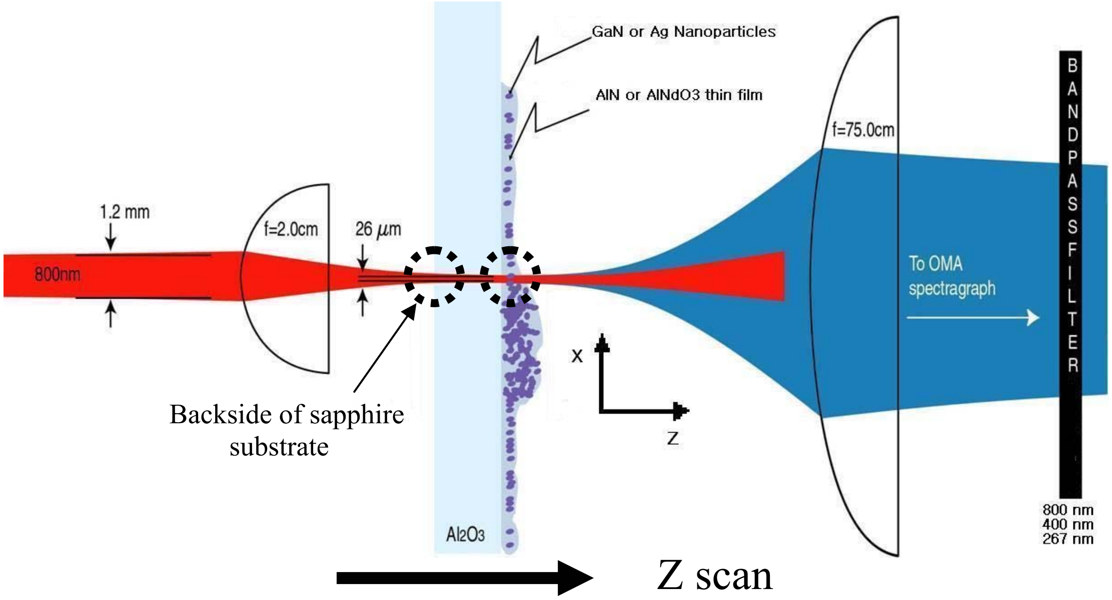

Figure 5.4 Schematic of setup for scanning second harmonic generation(SHG) and third harmonic generation(THG). The sample is mounted on a microstepper. Recording the harmonic signal as a function of microstepper position allowed us to map the harmonic response of the material. (Reproduced from Ref 5, by permission)

5.4 Fabrication of nanocomposites and experimental observations

Gallium nitride (GaN) semiconductor and silver (Ag) metal nanocomposites were deposited on sapphire substrates using electrostatic collection and supersonic collection processes which were described in detail in section 2.2. The LAM generator has been coupled to a high vacuum PLD chamber for in situ construction of nanocomposites. For nanocomposites, substrates are inserted into the load lock and moved under vacuum into the nanoparticle deposition chamber. Nanoparticles are produced in the flowing aerosol cell and deposited by inertial impaction. To overcoat the nanoparticles, the sample is moved under vacuum into the PLD (Pulsed Laser Deposition) chamber where a thin film is grown over the nanoparticles as described in detail in section 2.3. Therief process of nanocomposite fabrication is shown schematically in Fig 5.5 and the schematic of nanocomposite production chamber is shown in Fig 5.6.

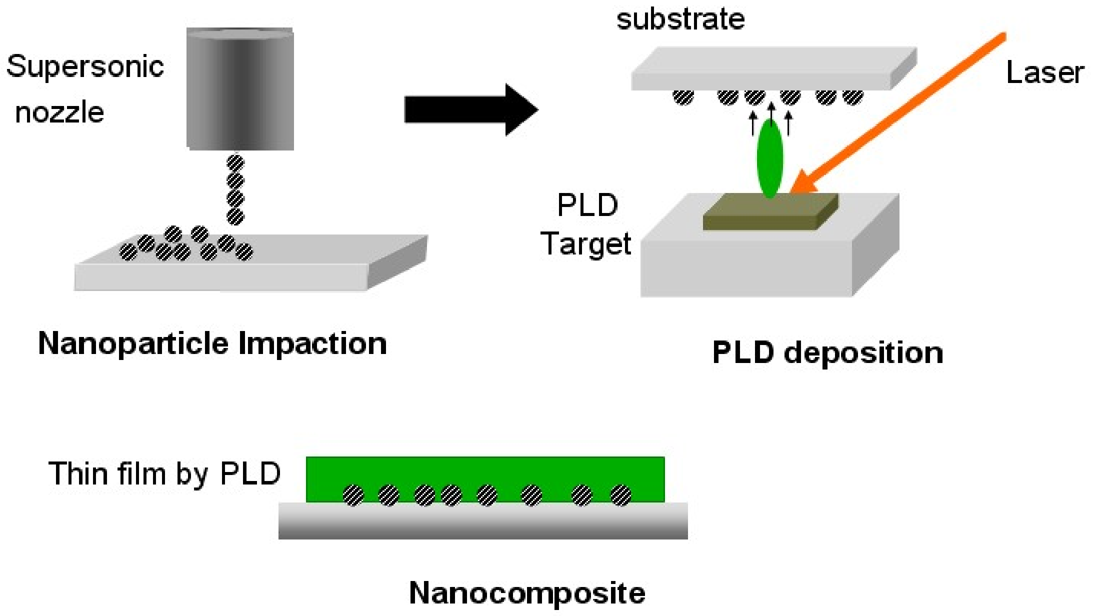

Figure 5.5 The process of nanocomposite fabrication.

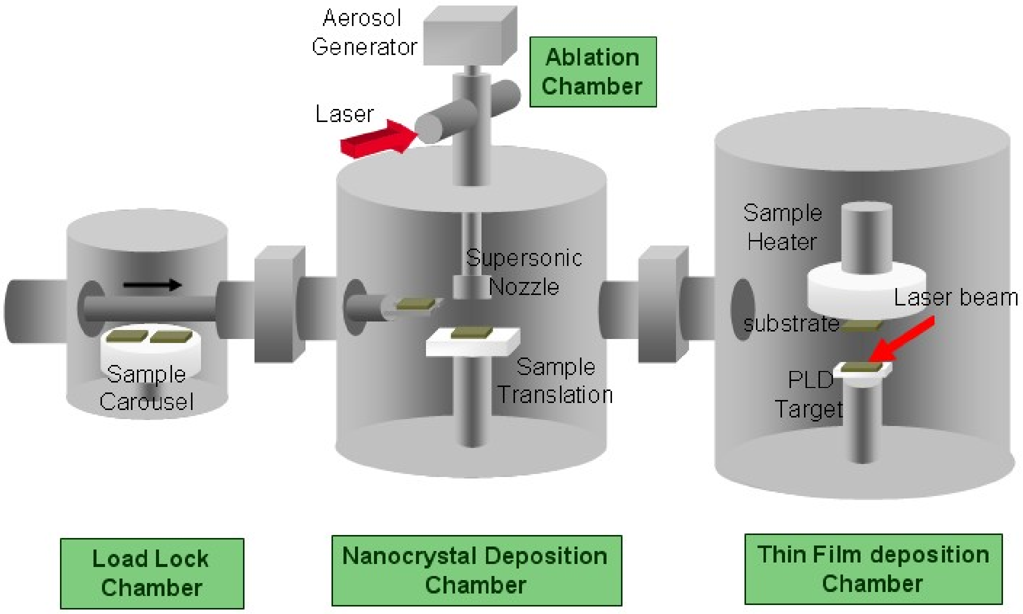

Figure 5.6 The schematic of nanocomposite production chamber.[11]

5.4.1 Gallium nitride nanocomposite

5.4.1.1 Deposition of gallium nitride nanoparticles

GaN nanoparticles are produced by laser ablation of GaN microparticles in the electrostatic cell as decribed in section 2.2.1. GaN microparticle feedstock was found to be between 2-5 microns in size and irregularly shaped. The SEM image and XRD pattern of the feeding GaN microparticles are shown in Fig 5.7(a), (b) respectively. XRD clearly shows that the GaN microparticles are crystalline have crystal structures. The feedstock is aerosolized in a fluidized bed generator and entrained in a slow helium gas flow of 110 SCCM corresponding to a 80-100 cm/s flow velocity. The number density of microparticles is controlled by the vibration frequency of the fluidized powder and was adjusted to be 10^5-10^7 cm^{-3}. Ablation of the microparticle jet is carried out with the excimer laser at a fluence of 2.5 J/cm^2. The flow rate of the aerosol shown above is set to match the 200 Hz laser repetition rate so that each microparticle iswas exposed to exactly one laser pulse. The optimum helium sheath flow is 1330 SCCM corresponding to 7.1 cm/s flow velocity. The length of the tube used was 20 cm and connected to long rubber pipe so that the discontinuity at the end of the tube did not cause turbulenceaffect the flow in the region of interest.

The nanoparticles are electrically charged due to a combination of thermionic and photoelectric ionization during the ablation process. As described in section 2.2.1 the highly charged, flowing aerosol of nanoparticles forms in a region with an electrostatic field of 0-1000 Volts applied transverse to the nanoparticle flow for collection.

Samples were examined for size distributions with a Phillips EM 208 TEM (80 keV operating voltage) to determine primary particle size, shape and aggregation state of these particles.

5.4.1.2 Deposition of aluminum nitride thin film

Following GaN nanoparticle deposition on sapphire substrate, GaN nanoparticles were coated with aluminum nitride (AlN) using pulsed laser deposition (PLD) described in section 2.3 and 3.3. Depositions were carried out at 4.5 $\times 10^{-4}$ Torr nitrogen pressure and 300ºC substrate temperature for 20 mins. fluences ranging from 4-12 J/cm^2 and 200 HZ repetition rate were used.

(a)

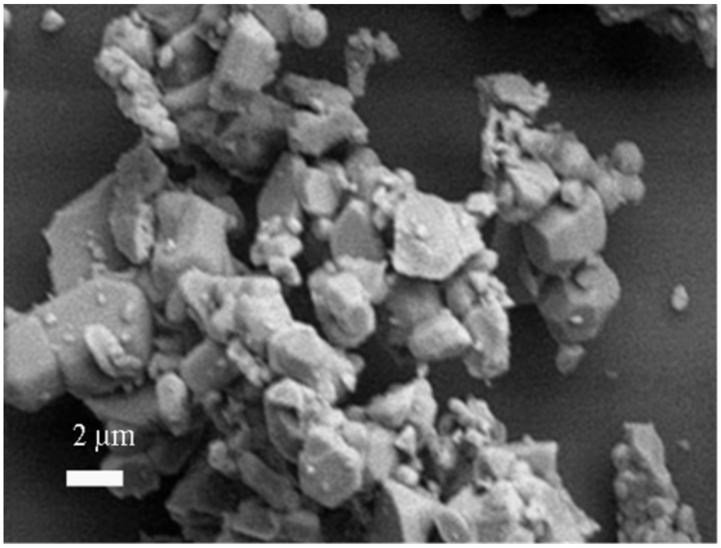

(b)

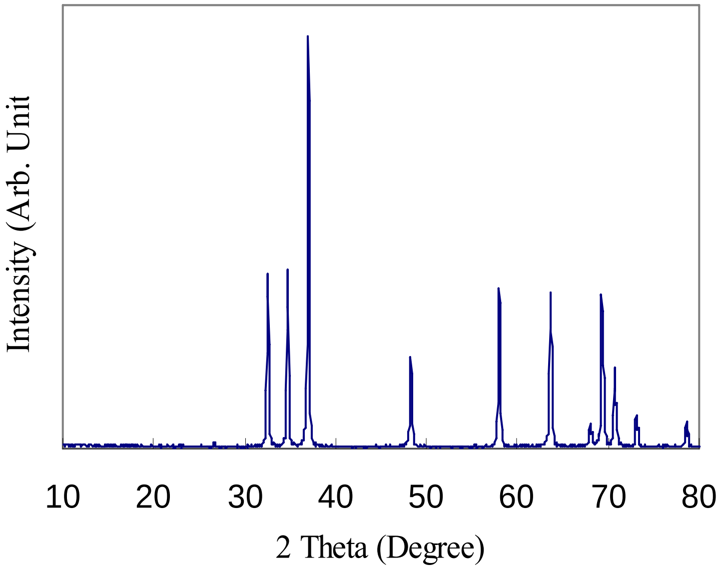

Figure 5.7 (a) SEM image of the feeding GaN microparticles. (b) XRD pattern of the feeding GaN microparticles.

5.4.1.3 Experimental observations of GaN nanocomposite

TEM images of particles collected on the ground electrode of the electrostatic cell in helium at high voltage show GaN nanoparticles were fabricated successfully (Fig. 5.8 (a)) even though agglomeration and/or chaining were observed in some samples. GaN nanoparticles were found to be spherical and 5.0±0.55 (nm) in size (Fig. 5.8 (b)). A typical XRD pattern of GaN nanoparticle prepared at V=300V in the electrostatic cell is shown in Fig. 5.8 (c). Amorphous glass substrates were used for the XRD measurement. XRD patterns show apparent peak broadening. The XRD peak broadening due to small particle size (Scherrer's formula[12]) is

$$B = \frac{K \cdot \lambda}{t \cdot \cos\theta_B} \qquad (5.11)$$

where B, K, λ, t, θ_B denote FWHM (Full width at half max), constant (0.89), X-ray wavelength (0.154 nm), thickness of crystallite (particle size) and Bragg angle. From Eq. 5.11, peak broadening (FWHM) of our GaN nanoparticles was calculated by substituting K=0.89, λ = 0.154 nm, t =5.0 nm , θ_B = 27 º. It resulted in B = 1.40 º. However, the FWHM in Fig. 5.8 (c) is 13 º, much wider than the calculated width. It clearly shows that XRD peak broadening is caused by another factor such as partly amorphous GaN structure rather than just by nano-size crystals. We can conclude crystalline GaN miroparticles were changed into semi-amorphous GaN nanoparticles through the LAM process.

The THG of GaN nanocomposite was measured by direct measurement along the z direction as described in section 5.3. The results were shown in Fig. 5.9. The first measurement was performed on a bare sapphire substrate. Subsequent measurements were repeated using bare AlN film on sapphire substrate, bare GaN nanoparticles on sapphire substrates and GaN nanoparitlces coated with AlN on sapphire substrates.

AlN thin film on sapphire showed the highest intensity. GaN coated with AlN on sapphire and bare GaN nanoparticles on sapphire substrate showed less THG intensity. Unexpectedly, the large enhancement of THG due to the quantum confinement effect of GaN nanoparticle did not occur in our fabricated samples.

We can speculate the cause from several observations. First, the LAM process would change crystalline GaN feedstock into semi-amorphous GaN nanoparticles as discussed above. Second, the agglomerations found in the GaN nanoparticles may degrade its unique properties.

Amorphous GaN nanoparticles coated with AlN showed less intensity than bare AlN thin film, probably due to local field effects described in section 5.2.5. For metal particles which have a negative real part of the dielectric constant, the local field can be enhanced resonantly at specific frequency. On the contrary, GaN nanoparticles and AlN thin film have similar dielectric constants ($\varepsilon_{GaN} / \varepsilon_{AlN}$ at 633 nm = 1.3) and the local field is reduced. Accordingly, THG signal is also reduced.

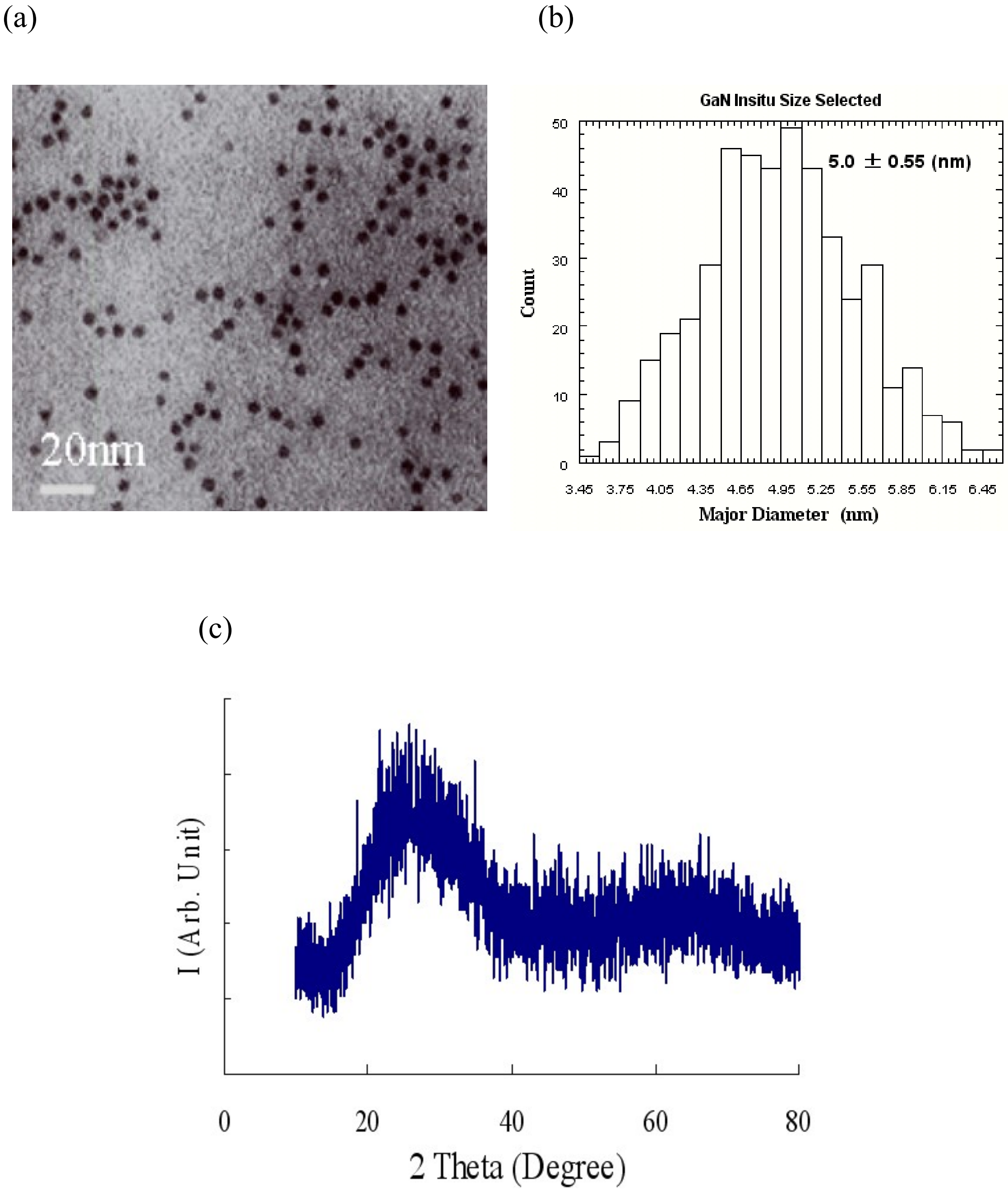

Figure 5.8 (a) TEM image of typical GaN nanoparticles. (b) Size distribution of GaN particles (c) XRD pattern of the GaN nanoparticles.

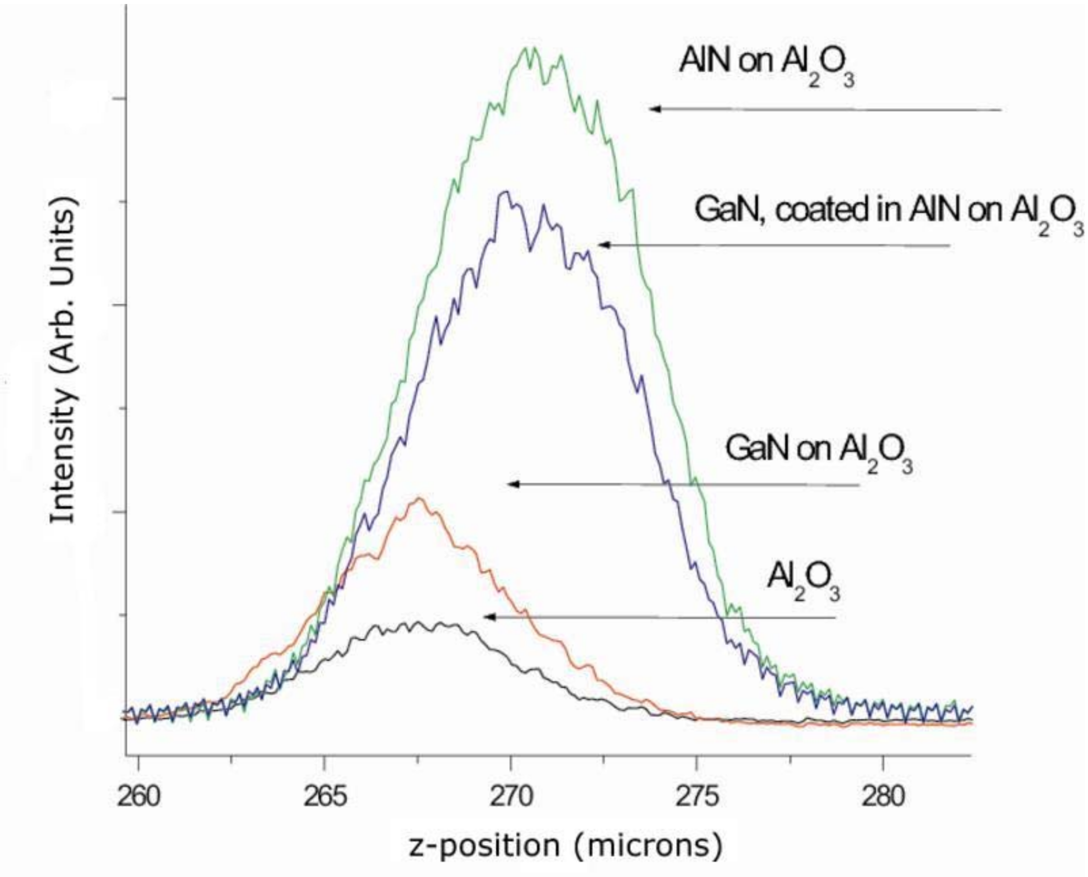

Figure 5.9 z directional scan of the THG intensity from sapphire substrate, GaN NP on sapphire substrate and GaN NP coated with AlN on sapphire substrate (Arb. Units)

5.4.2 Silver nanocomposite

5.4.2.1 Deposition of silver nanoparticles

Silver metal nanoparticles were produced by laser ablation of Ag microparticles and collected in the virtual impactor system as decribed in section 2.2.2. Silver microparticle feedstock (Dupont Electronics Materials division) was found to be spherical and between 1.5±0.2 micron in size. The SEM image and XRD pattern of the feeding silver microparticles are shown in Fig 5.10 (a). The feedstock is aerosolized in a fluidized bed generator and entrained in a slow gas flow corresponding to 0.5 m/s flow velocity. The number density of microparticles is controlled by the vibration frequency of the fluidized powder and was adjusted to be 10^5 cm^{-3}. Ablation of the microparticle jet is carried out with the excimer laser at a fluence of 2.5 J/cm^2. The flow rate of the aerosol was set to match the 200 Hz laser repetition rate so that each microparticle was exposed to exactly one laser pulse. As described in section 2.2.1 the ablated nanoparticles in the stream are drawn away from the flow axis into the collection chamber and were collected on sapphire substrate. Samples on TEM grid were examined for size distributions with a Phillips EM 208 TEM. Fig 5.10 (b) is a typical micrograph showing silver nanoparticles which are spherical and unnon-agglomerated with a mean size of 8nm.

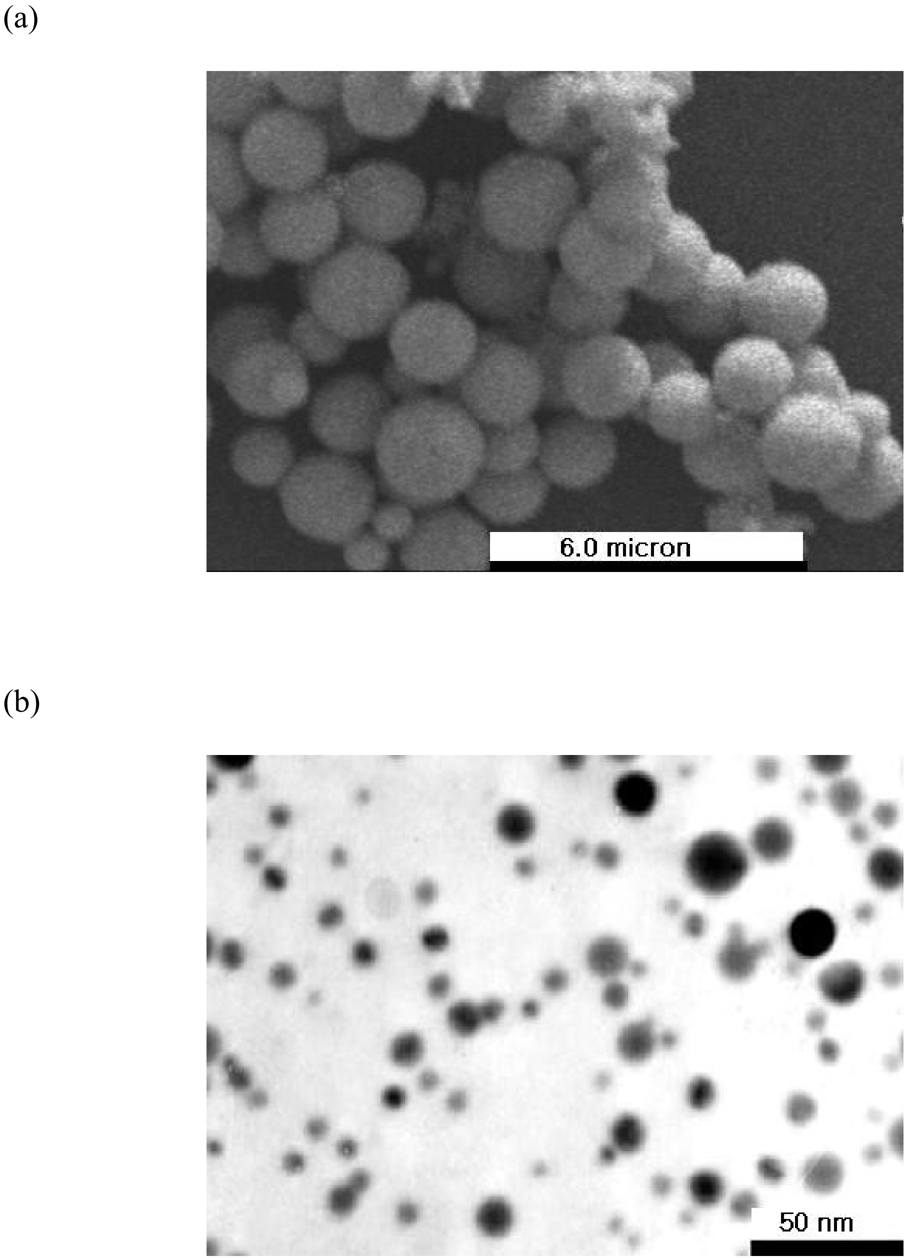

Figure 5.10 (a) Silver microparticles (b) TEM image of ablated silver nanoparticles.

5.4.2.2 Deposition of $NdAlO_3$ and Al_2O_3 thin films

Following silver nanoparticle deposition on sapphire substrate, two types of coatings, $NdAlO_3$ and Al_2O_3, were deposited for comparison using the pulsed laser deposition (PLD) technique. Depositions were carried out at 5 ×10^{-5} Torr oxygen pressure and a substrate temperature of 300ºC for 30 mins. The distance from target to substrate was 7.62 cm. High fluencences, 4-12 J/cm^2, and 200 HZ repetition rate were used.

5.4.2.3 Experimental observations of silver nanocomposite

The linear transmission of bare $NdAlO_3$ film (without silver nanoparticles) was measured by a UV-VIS spectroscopy and is shown in Fig 5.11. Many local absorptions were found due to Nd^{3+} ions in the film. There was no interference pattern because the refractive index of $NdAlO_3$ is similar to that of the sapphire substrate. To confirm this we deposited $NdAlO_3$ on a quartz substrate and applied OPE method, chapter 3. Fig 5.12 shows the result by OPE method. Even though there were some distortions of experimental transmittance due to the local absorption of Nd^{3+} ion, the OPE method was successfully applied and extracted the optical information. The result showed that the refractive index of $NdAlO_3$ film is similar to that of Al_2O_3 ($n_{NdAlO_3} / n_{sapphire}$ at 633 nm = 1.06± 0.01). The difference of the refractive index of $NdAlO_3$ film was less than 1% which is very small. The extinction coefficient was also extracted and turned out to be very small. It was $1.1\times10^{-3} \pm 0.05$ at 633 nm.

Figure 5.13 shows the transmittance spectra of bare Ag nanoparticles on a sapphire substrate. The spectra of bare $NdAlO_3$ film and Ag nanoparticles on a sapphire substrate coated with $NdAlO_3$ are also presented for comparison. The transmission of bare Ag nanoparticles shows broad plasmon resonance absorption centered at 442 nm. Ag nanopaticles coated with $NdAlO_3$ showed an interference pattern in addition to plasmon resonance because silver nanoparticles acted as another thin film sandwiched between the $NdAlO_3$ thin film and sapphire substrate. Accordingly, as the thickness of Ag nanoparticles increased, denser interference pattern were measured. In order to find the optical properties of Ag nanoporous film and $NdAlO_3$ coating, OPE method was applied in many ways. However, an appropriate model for the extinction of the silver film could not be found.

It is also interesting to note that the plasmon resonance wavelength of the nanocomposite shows a redshift compared to bare silver nanoparticles. Bare silver nanoparticles showed a plasmon resonance at 430 nm. However, Ag nanoparticles on a sapphire substrate coated with $NdAlO_3$ shows a plasmon resonance at 495 nm due to $NdAlO_3$ coating (redshift, see Fig 5.13).

This result agrees with simulation result in section 5.2.5. It shows that wavelength tuning for plasmon resonance is feasible using different dielectric layers on silver nanoparticles. G.Xu et al found that mediums, either covering or sandwiching the silver islands, can be tuned to the plasmon resonance wavelength.[13]

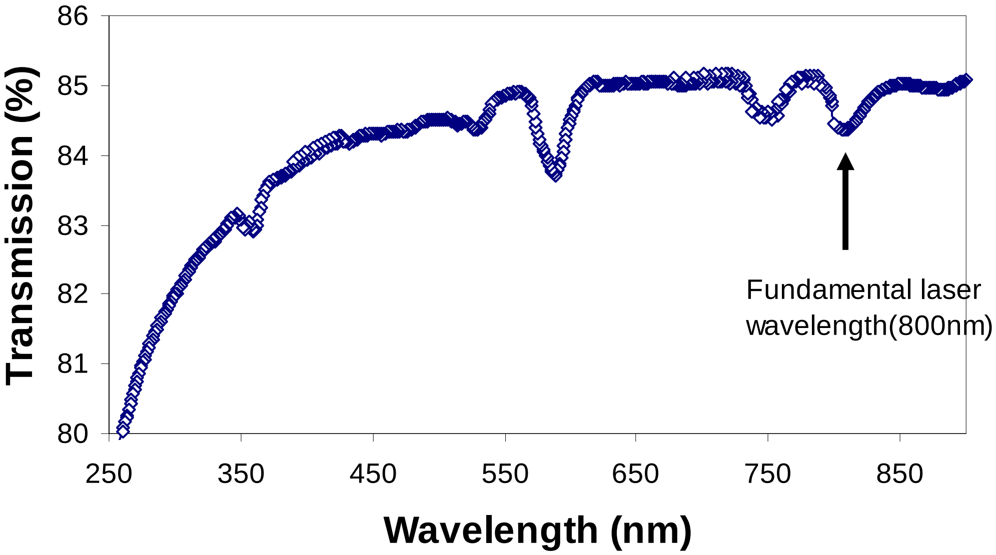

Figure 5.11 Spectral transmission of NdAlO3 film on sapphire substrate

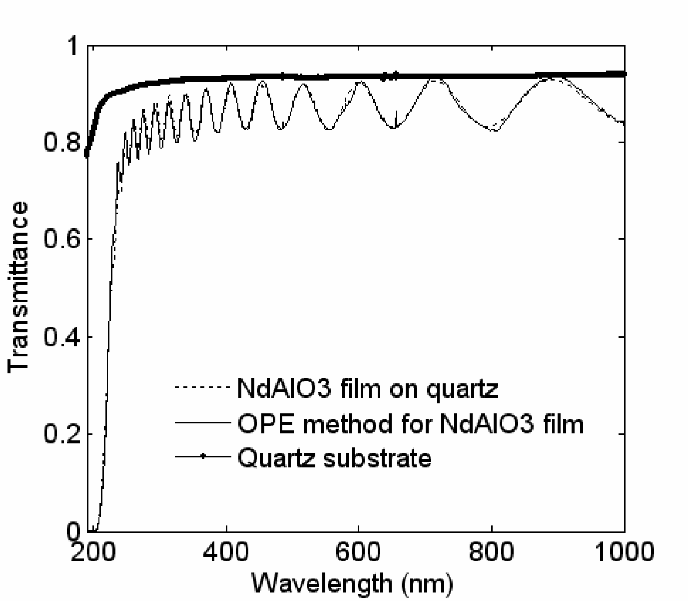

Figure 5.12 Spectral transmittance of $NdAlO_3$ film on quartz substrate and corresponding transmittance fit using OPE method.

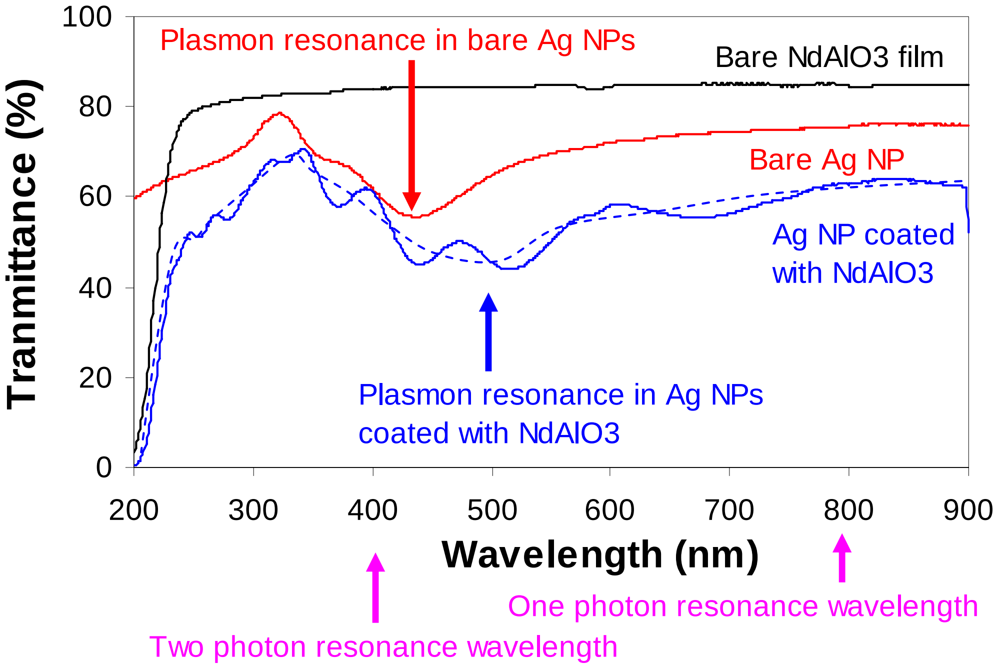

Figure 5.13 Transmittance spectra of $NdAlO_3$ film, bare Ag nanoparticles and Ag nanoparticles coated with $NdAlO_3$. (The dotted lines are a guide)

5.4.2.3.1 The THG and SHG of bare silver nanoparticles

The SHG and THG of bare silver nanoparticles and silver nanocomposite were measured by direct measurement. The measurement was performed along the z direction of samples with bare silver nanoparticles on sapphire substrate and the results were shown in Fig 5.14. The spectrum of sapphire substrate THG (dashed) is also present for comparison. The THG signal due to Ag nanoparticles begins to increase from 200 μm and disappears at 590 μm. The maximum intensity was increased by a factor of 2.5 compared to sapphire substrate THG at 400 μm. The maximum enhancement occurred at the center of the nanoparticle deposits. However, SHG signal saturated at the THG maximum peak.

The enhancement in bare silver nanoparticles can be explained by local field enhancement due to particle plasmon excitation in the submicroscopic surface structure. Two photon resonance (400 nm) is nearly coincident with plasmon resonance wavelength (430 nm) in our bare silver nanoparticles.

5.4.2.3.2 The THG and SHG of silver nanoparticles coated with $NdAlO_3$ film

The SHG and THG measurements of silver nanocomposite coated with $NdAlO_3$ were performed along z direction and x direction and results are shown in Fig 5.15 The THG spectrum of $NdAlO_3$ thin film on sapphire substrate(dashed) is also present for comparison. The THG signal due to Ag nanoparticles coated with $NdAlO_3$ was much less than those of bare Ag nanoparticles on sapphire substrates and $NdAlO_3$ thin films. Two photon resonance (400 nm) deviated further (redshifted) from plasmon resonance wavelength (430 nm) due to the $NdAlO_3$ coating as expected in simulation results of section of 5.2.5. On the other hands, SHG signal showed a Gaussian profile which is contrary to the samples with bare silver nanoparticles.

The SHG and THG measurements of silver nanocomposite coated with $NdAlO_3$ were performed along x direction and results are shown in Fig 5.16 for comparison. Unlike the z scan shown in Fig. 5.15 where the THG was a factor of ½ that of the bare $NdAlO_3$, the THG at $x = 530$ microns is a factor of x2 larger than that of the $NdAlO_3$ seen at $x = 0$ in Fig. 5.16. This indicates that the THG in $Ag:NdAlO_3$ is very sensitive to the density of silver. The z-scan in Fig. 5.15 was taken an x position leading to a much smaller third-harmonic intensity.

5.4.2.3.3 The THG and SHG of silver nanoparticles coated with Al_2O_3 film

The SHG and THG measurements of silver nanocomposite coated with Al_2O_3 were performed along z direction and results are shown here (Fig 5.17). The THG spectrum of bare sapphire substrate THG (dashed) is also present for comparison. The THG signal was similar to that of Ag nanoparticles coated with $NdAlO_3$ at the x position for Fig. 5.15, but significantly smaller (at least 5x) than that shown in Fig. 5.16. (The backside of bare sapphire substrate could be the reference). SHG signal also showed a similar Gaussian profile (unsaturated).

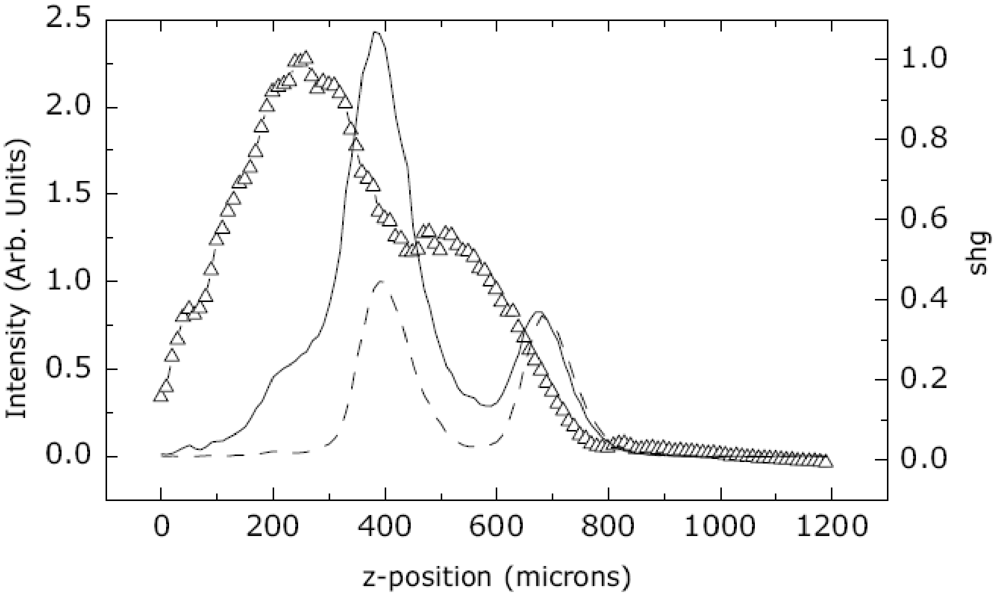

Figure 5.14 z directional scan of the SHG (Δ) and THG (Solid) from Bare Ag nonoparticles on sapphire substrate and the THG of sapphire substrate only (dashed). (Reproduced from Ref 5, by permission)

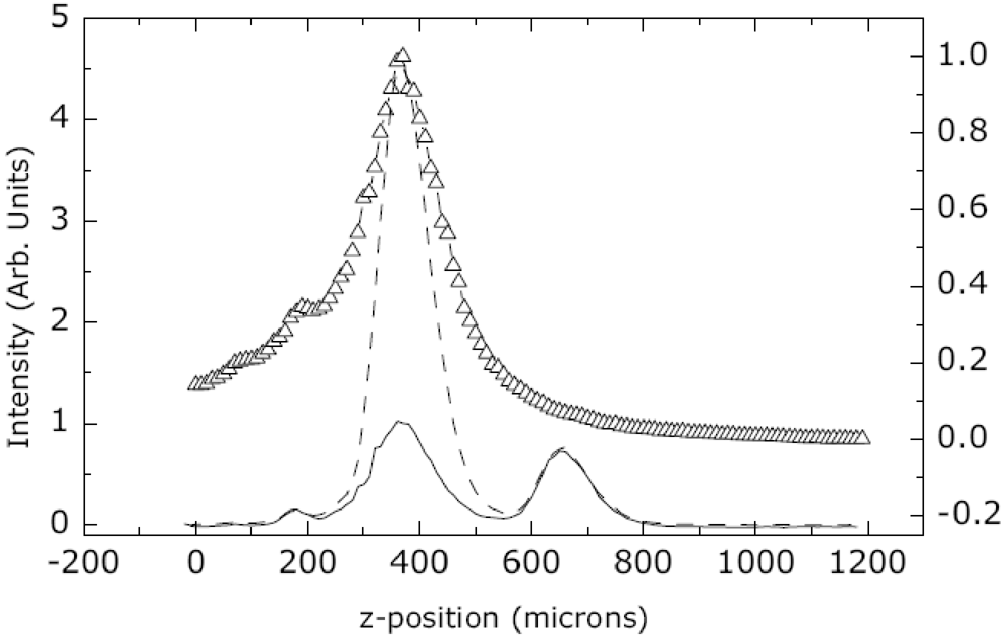

Figure 5.15 z directional scan of the SHG (Δ) and THG (Solid) from Ag nonoparticles coated $NdAlO_3$ film on sapphire substrate and the THG from a pure $NdAlO_3$ film on sapphire substrate (dashed). (Reproduced from Ref 5, by permission)

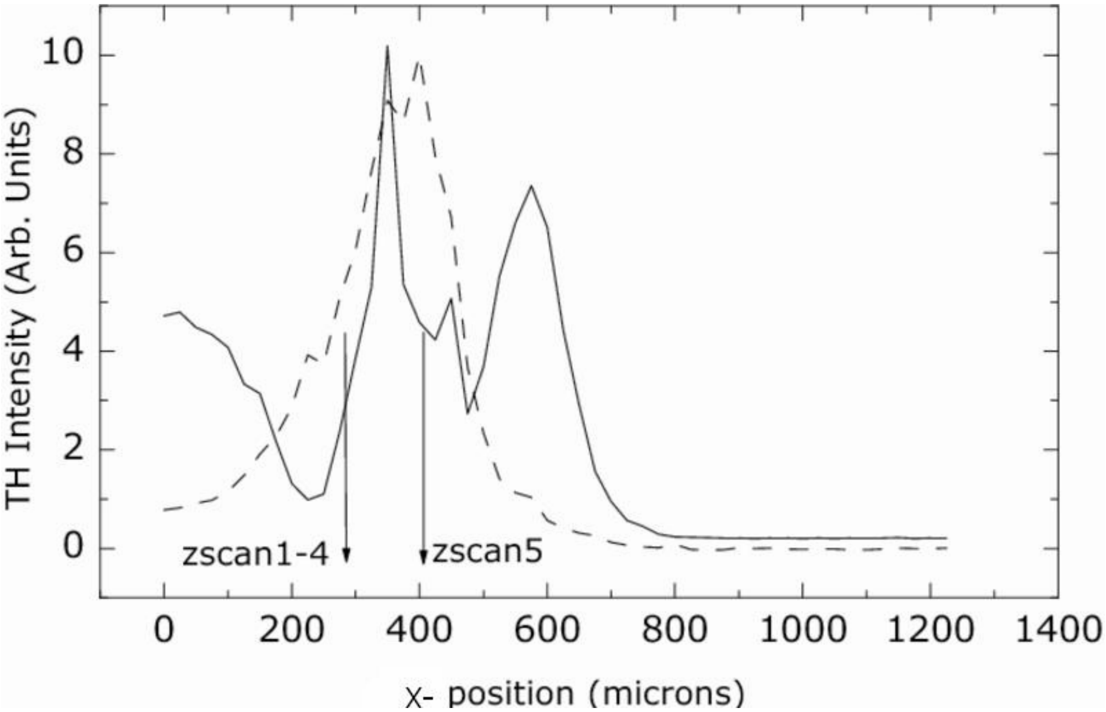

Figure 5.16 x directional scan of the SHG (dotted) and THG (Solid) from Ag nonoparticles coated $NdAlO_3$ film on sapphire substrate. (Reproduced from Ref 5, by permission)

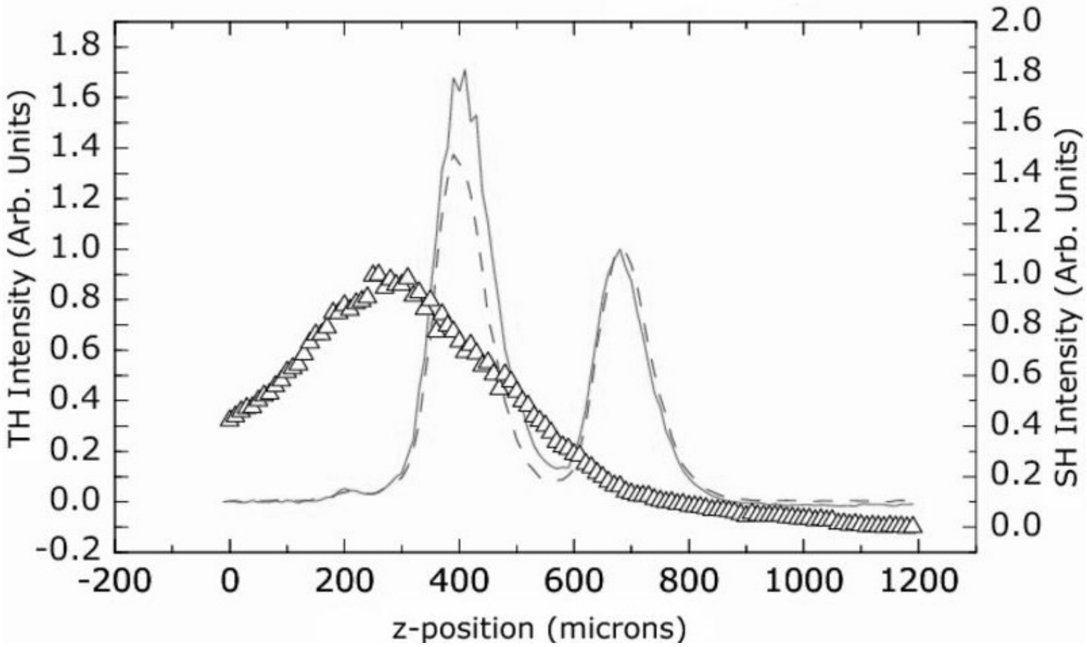

Figure 5.17 z directional scan of the SHG (Δ) and THG (Solid) from Ag nonoparticles coated Al_2O_3 film on sapphire substrate and the THG from bare sapphire substrate (dashed) (Reproduced from Ref 5, by permission)

5.4.2.3.4 Discussion

We expect it is possible to obtain very large values of the nonlinear susceptibility through resonance enhancement. If one of the real atomic levels is nearly coincident with one of the virtual levels of the indicated process, the coupling between the radiation and the atoms is particularly strong and the nonlinear optical susceptibility becomes large. For instance, three possible strategies for enhancing the efficiency of third-harmonic generation through the technique of resonance enhancement are possible; (a) the one-photon transition is nearly resonant (b) the two-photon transition is nearly resonant and (c) the three-photon transition is nearly resonant.

In the case of Ag NPs coated with $NdAlO_3$ film, the one-photon resonance (800nm) due to Nd^{3+} ion absorption and two-photon resonance (400nm) due to silver absorption (plasmon absorption) were expected (see Fig 5.18). Nd^{3+} ion has the real atomic level at 800 nm (see Fig 5.11) where the fundamental laser wavelength is tuned. Therefore, the one-photon resonance is possible since this energy level coincides with our laser wavelength (800 nm). The two-photon resonance (400nm) is also expected in Ag NPs coated with $NdAlO_3$ because silver NPs strongly absorb around 400 nm due to the plasmon resonance, and strong photoluminescence following two-photon absorption was observed at 800 nm.

To check the effect of one-photon resonance due to the Nd^{3+} ion, THG signals of Ag NPs coated with $NdAlO_3$ in Fig 5.15 (z directional scan), Fig 5.16 (x directional scan) and THG signals of Ag NPs coated with Al_2O_3 in Fig 5.17 (z directional scan) were compared. The THG of Ag NPs coated with $NdAlO_3$ (Fig 5.16) was two times that of the plain $NdAlO_3$ film which was 4 times that of sapphire (Fig 5.15). Thus at the appropriate x-position (eg, appropriate Ag NPs density) Ag NPs coated with $NdAlO_3$ generated eight times that the THG of Al_2O_3 (Fig 5.17). The lack of large THG enhancement may result from strong SHG for the Ag NPs coated with $NdAlO_3$.

Next comparison was made between bare silver NPs and silver NPs coated with $NdAlO_3$ (Fig 5.14, Fig 5.15). The THG signal was enhanced in bare silver nanopaprticles due to the plasmon resonance (see Fig 5.14). However, in the case of Ag NPs coated with $NdAlO_3$ the THG intensity was decreased by 40% at intermediate laser intensities compared to bare Ag NPs but increase by a factor of 50% at higher fields because of saturation in the bare Ag samples. Enhancement due to both a tw-photon plasmon resonance and a single photon resonance in the THG did not seem to occur. Second harmonic generation in the Ag:$NdAlO_3$ samples was 50 % larger than for the bare Ag samples and may contribute to the lack of THG for these samples.

We can speculate the cause from Fig 5.13. Bare silver nanoparticles has an absorption band at 430 nm due to plasmon resonance and it is close to the two-photon resonance frequency (400nm) of our laser wavelength. Therefore, two-photon resonance due to plasmon resonance was possible and THG signal was increased. However, in the case of Ag NPs coated with $NdAlO_3$ the plasmon resonance was redshifted and moved off the two photon resonance wavelength when silver NPs were coated with $NdAlO_3$ (see Fig 5.13). In other words, plasmon resonance is tuned from 430 nm to 490nm due to $NdAlO_3$ film and it is too far from two-photon resonance frequency of our laser wavelength (400 nm). As a consequence the enhancement effect due to two-photon resonance was turned off or reduced. Though it is not certain that the two-photon resonance shifts identically to the one-photon plasmon resonance for the NdAlO3 this may explain the lack or the expected large enhancement when the Nd ions were added to resonate with the one photon transition.

To enhance the THG signal, varying the incident laser frequency or tuning the plasmon resonance frequency of silver nanocomposite is necessary to make the second harmonic frequency of the laser coincide with plasmon resonance frequency.

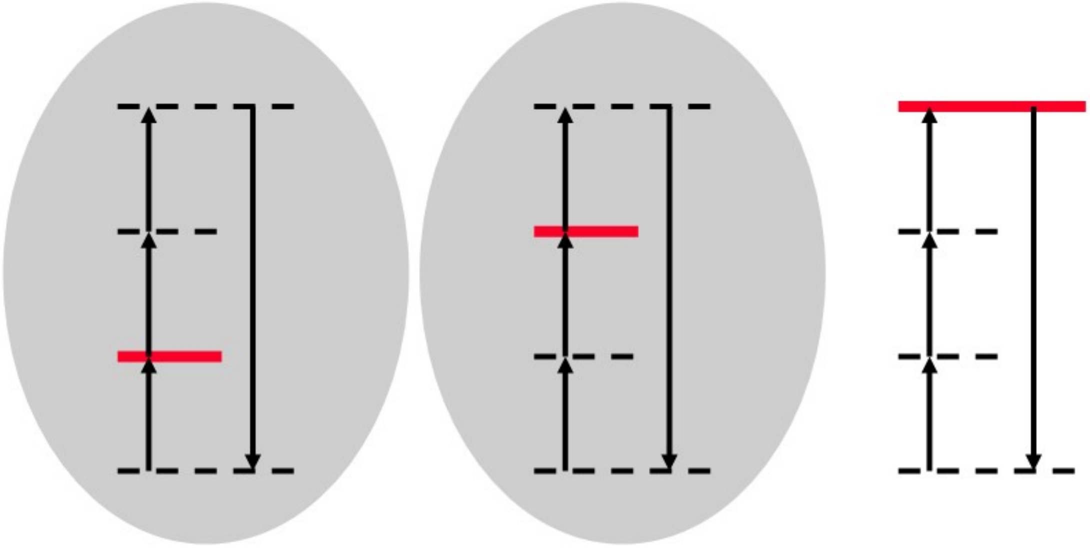

Figure 5.18 Three strategies for enhancing the process of third-harmonic generation. (a) One photon resonance (b) Two photon resonance (c) Three photon resonance ; one photon and two photon resonance were expected in silver nanoparticles coated with $NdAlO_3$ due to Nd^{3+} ion and silver NPs plasmon absorption respectively.

5.5 Summary

GaN nanocomposites with AlN thin films and Ag nanocomposites with $NdAlO_3$ films were synthesized by LAM process and PLD deposition. The enhancement of THG in GaN nanocomposite did not occur due to its amorphousness, oxidation and agglomerations.

Ag nanocomposites with $NdAlO_3$ films were synthesized. The plasmon resonance of Ag nanocomposites with $NdAlO_3$ films showed a red-shift when compared to bare silver nanoparticles. It showed that wavelength tuning of plasmon resonance using different thin film layer on silver nanoparticles is feasible.

The THG signal was enhanced in bare silver nanopaprticles due to the plasmon resonance. On the contrary, in the case of Ag NPs coated with $NdAlO_3$ the THG intensity was decreased by 40% at intermediate fields because the plasmon resonance wavelength was redshifted and moved off the two-photon resonance wavelength of the laser. To enhance the THG signal, varying the incident laser frequency or tuning the plasmon resonance frequency of silver nanocomposite is necessary to make the second harmonic frequency of the laser coincide with plasmon resonance frequency.

---

[1] Ch. Bosshar, K. Sutter, Ph. Pretre, J. Hulliger, Florsheimer, P. Kaatz, P. Gunter, Organic Nonlinear Optical Materials, in: A.F. Gario (Ed.), Advances Nonlinear Optics, vol. 1, Gordon and Breach, New York, 1995.

[2] H. Kalt, V.G. Lyssenko, R. Renner, C. Klingshirn, J. Opt. Soc. Am. B **2** , 1188. (1985)

[3] R. Vijaya, Y.V.G.S. Murti, G. Sundararajan, T.A. Prasada Rao, Opt. Commun. **76**, 256. (1990)

[4] N.Herron and D.L. Thorn. Adv. Mater. 10,1173 (1998)

[5] David S. Stoker " Ultrafast third-harmonic generation from nanostuructured optical thin films and interfaces" (2006)

[6] P. Roussgnol, D. Ricard, C. Flytzanis, Appl. Phys. B 437 (1990).

[7] Nasu, Hiroyuki; Tanaka, Akimasa; Kamada, Kenji; Yamamoto, Yoshitsugu; Matsuzaki, Yasuhiro; Hashimoto, Tadanori. Journal of the Ceramic Society of Japan , **110,** 921 (2002)

[8] Prakash, G. Vijaya; Cazzanelli, M.; Gaburro, Z.; Pavesi, L.; Iacona, F.; Priolo, Materials Research Society Symposium Proceedings, **722**, 219 (2002)

[9] Yao, Weiguo; Shi, Wangzhou; Lin, Kuixun; Qi, Zhenzhong; He, Yizhen. Science in China, Series A: Mathematics, Physics, Astronomy, **39**, 991 (1996)

[10] C. Bohren and D. Huffmann, *Absorption and Scattering of Light by Small Particles* (John Wiley, New-York, 1983).

---

[11] W. T. Nichols, "Production and controlled collection of nanoparticles; toward manufacturing of nanostructured materials" Dissertation, The University of Texas at Austin (2002)

[12] P. Scherrer. Gottinger Nachrichten (1918); cf. also. R.Zsigmondy, Kolloidchemie (3rd Ed, 1920), p. 394

[13] G. Xu, M. Tazawa, P. Jin, S. Nakao and Yoshmura, Applied Physics Letters, 82, 3811 (2003)

6
Conclusions

Aluminum nitride thin films were fabricated using Pulsed Laser Deposition with varying processing conditions in order to exploit the feasibility for encapsulating matrix of nonlinear nanocomposites. In order to accurately extract optical properties of non-uniform films, We have developed a new method for extracting properties of wedged and absorbing thin films, including refractive index, extinction coefficient, and thickness, based only on a measurement of the transmission (or reflection) spectrum. This Optimum Parameter Extraction (OPE) method utilizes a combination of numerical optimization, efficient models of dispersive film parameters, and film transmission equations derived for wedged, non-uniformly thick, and absorbing films (having 2-D non-uniformity) measured through a rectangular aperture. We also introduced a one-parameter, packing-density model for refractive index that requires measurement of the refractive index dispersion of the same or similar material. The Sellmeier equation was also shown to work, but with the disadvantage of having more parameters to fit. The OPE method was found to accurately predict the values of optical constants for test cases that produced large errors when determined using previous methods. We showed that the OPE method could incorporate only 1-D non-uniformity in thickness and still converge rapidly and predict the values of optical constants accurately when a rectangular illumination area was used to record the transmission spectrum. Using our OPE method, optical properties of AlN thin films with thickness variation were accurately determined, whereas the presence of absorption and thickness non-uniformity in the films resulted in large errors when other methods were used.

Aluminum nitride films were grown using PLD onto sapphire (0001) substrates using varying processing conditions (temperature, nitrogen pressure, and laser fluence). The films deposited at low nitrogen pressures (less than 4.5×10^{-5} Torr) exhibited, without exception, poor optical transmission, independent of the laser fluence and substrate temperature. In contrast, all films produced at higher nitrogen pressure (4.5×10^{-4} Torr) exhibited high transmission ($k = 0.5 - 2.5 \times 10^{-3}$). We can speculate that a critical pressure exists between 4.5×10^{-5} Torr and 4.5×10^{-4} Torr, above which the film transparency becomes high. Of the films deposited at the higher nitrogen pressure, those deposited at low substrate temperatures had a lower extinction coefficient than those deposited at higher substrate temperature (up to 800°C). Our results show unambiguously that high quality films with high optical transmission can be deposited by PLD without resorting to high temperatures or UHP (ultra-high purity) processing conditions. In fact, the samples that had the lowest extinction coefficient were produced at low substrate temperatures and had relatively poor alignment of the grains to the substrate. The bandgap was derived from these absorption measurements. We found that bandgap increased with both temperature and deposition rate. In multiple regression analysis, deposition rate was found to have a stronger influence on bandgap than temperature. This would imply that high substrate temperature and low deposition rate favor fewer band-edge defects in the film, but that these defects do not correlate with absorption at visible wavelengths. Refractive index, on the other hand, showed little systematic dependence on processing parameters. It is possible that small systematic variations in refractive index may occur, but if these variations are less than the measurement error of 2%, they would not be observed. We observed no correlation between the degree of texture and the optical properties. However, the variation in the texture orientation observed across a sample might make a weak dependence impossible to observe. This variation in texture orientation measured across a sample deposited at 900°C was observed to correlate with the visible variation in its brownish color (opacity). The brownish color of the samples prepared at 900 ºC can be attributed to more severe surface oxidation as the oxidation kinetics accelerate rapidly at this temperature. Any subtle correlation between AlN film extinction coefficient and crystal properties was probably not found due to the dominant absorption of the surface oxidation layer. Localization of the majority of the absorption in the oxidation layer does place an upper limit on the AlN film absorption, and indicates that the extinction coefficient in the AlN films was remarkably low (< $5x10^{-4}$ at 633 nm). we report that low optical absorption, textured polycrystalline AlN films can be produced by PLD on sapphire substrates at both low and high laser fluence using a background nitrogen pressure of 4.5×10^{-4} Torr at 99.9% purity.

Third harmonic generations from GaN nanocomposite coated with AlN film and silver nanocomposite coated with $NdAlO_3$ were investigated experimentally. The enhancement of THG in GaN nanocomposite did not occur because the LAM process would change crystalline GaN feedstock into semi-amorphous GaN nanoparticles.

The plasmon resonance of Ag nanocomposites with $NdAlO_3$ films showed a red-shift when compared to bare silver nanoparticles. The THG signal was enhanced in bare silver nanopaprticles due to the plasmon resonance. On the contrary, in the case of Ag NPs coated with $NdAlO_3$ the THG intensity was decreased by 40% at intermediate fields because the plasmon resonance wavelength was redshifted and moved off the two-photon resonance wavelength of the laser. To enhance the THG signal, varying the incident laser frequency or tuning the plasmon resonance frequency of silver nanocomposite is necessary to make the second harmonic frequency of the laser coincide with plasmon resonance frequency.

References

Chapter 1

A A Seraphin, E. Werwa and K. D. Kolenbrander , J. Mater. Res. **12,** 3386 (1997)

C. B. Murray, D. J. Norris and M. G. Bawendi , J. Am. Chem.Soc. **115,** 8706 (1993)

G.M. Whitesides, J.P. Mathias, C.T. Seto. Science **254**,1312 (1991)

M. Fujii,A. Mimura, S. Hayashi, K. Yamamoto. Appl. Phys.Lett., **75**, 184 (1999)

S.K. Bera, S. Chaudhuri, A. K. Pal, J. Phys. D: Appl. Phys., **33**, 2326 (2000)

J. Zhou; L. Li, Z. Gui, S. Buddhudu, Y. Zhou, Appl. Phys. Lett., **76**, 1540 (2000)

C.M Bender, J. M. Burtlich, D. Barber, C. Pollock, Chem. Mater., **12**, 1969 (2000)

C. Bohren and D. Huffmann, *Absorption and Scattering of Light by Small Particles* (John Wiley, New-York, 1983).

Chapter 2

J.C. Carls and J.R. Brock , Opt. Lett., **13**, 273 (1988).

J.C. Carls. and J.R. Brock, Opt. Lett., **13**, 919 (1988).

M. F. Becker, J.R. Brock & J.W. Keto, U.S. Patent No. 5,585,020. (1996).

W.T. Nichols , G. Malyavanatham, D.E. Henneke, J.R. Brock, M.F. Becker, J.W. Keto and H.D. Glicksman, J. Nanoparticle Res. **2**, 141 (2000).

W.T. Nichols, J.W. Keto, D.E. Henneke, J.R. Brock, G. Malyavanatham, M.F. Becker and H.D. Glicksman, Appl. Phys. Lett, **78**, 1128 (2001).

J. Lee, M. F. Becker, J. W. Keto, J. Appl. Phys., **89**, 8146 (2001).

W. T. Nichols, G. Malyavanatham, D. E. Henneke, J. R. Brock, M. F. Becker, J. W. Keto, J. Nanoparticle Research, **4**, 423 (2002).

L Banyai, Y. Z. Hu, M. Lindberg and S. W. Koch, Phys. Rev. B **38**, 8142 (1988)

D.E. Henneke. “Nanoparticles produced via laser ablation of microparticles” Dissertation, The University of Texas at Austin (2001).

W. T. Nichols, “Production and controlled collection of nanoparticles; toward manufacturing of nanostructured materials” Dissertation, The University of Texas at Austin (2002).

W. T. Nichols, “Production and controlled collection of nanoparticles; toward manufacturing of nanostructured materials” Dissertation, The University of Texas at Austin (2002).

Y. Hamanaka, K. Fukuta, and A. Nakamurab, Appl. phys. letter. **84**, 4938 (2004)

D. T. O’Brien, “Deposition and Characterization of Nanostructured Silver Thick Films”, Thesis, The University of Texas at Austin (2003).

C. Ristoscu, I. N. Mihailescu, M. Velegrakis, M. Massaouti, A. Klini, and C. Fotakis, J. Appl. Phys. **4**, 2244 (2003).

D. Dijkkamp, T. Venkatesan, X. D.Wu, S . A. S hareen, N. Jiswari, Y. H. Min-Lee, W. L. McLean, and M. Croft, Appl. Phys. Lett. **51**, 619 (1987).

S. Fahler and H. U. Krebs, Appl. Surf. Sci. **96–98**, 61 (1996).

R. Kelly, and J. E. Rothenberg, Nucl. Instrum. Methods Phys. Res. B **7/8**, 755 (1985).

C. R. Phipps, T. P. Turner, R. F. Harrison, G. W. York, W. S. Osborne, G. K. Anderson, X. F. Corlis,, L. C. Haynes, H. S. Steele, K. C. Spicochi, and T. R. King, J. Appl. Phys. **64**, 1083 (1988)

Chapter 3

Fujii, M.; Mimura, A.; Hayashi, S.; Yamamoto, K. Appl. Phys.Lett., **75**, 184 (1999)

Bera, S. K.; Chaudhuri, S.; Pal, A. K. J. Phys. D: Appl. Phys., **33**, 2326 (2000)

Zhou, J.; Li, L.; Gui, Z.; Buddhudu, S.; Zhou, Y. Appl. Phys. Lett., **76**, 1540 (2000)

Bender, C. M.; Burtlich, J. M.; Barber, D.; Pollock, C. Chem. Mater., **12**, 1969 (2000)

Russell J. Gehr, Robert W. Boy, Chem. Mater. **8**, 1807 (1996)

J.E. Sipe and Robert W. Boyd, Physical Review A, **46**(3), 46 (1992)

Robert W. Boy , Russell J. Gehr, Goerge L Fischert and J.E Sipe, Pure Appl. Opt. **5**, 505 (1996)

L.-P. Wang, D. S. Shim, Q. Ma, V.R. Rao, E. Ginsburg, A. Talalyevsky, J. Vac, Sci. Technol. A **23**, 1284 (2005).

Sancho-Parramon, J.; Modreanu, M.; Bassas, J. Proceedings of SPIE-The International Society for Optical Engineering, **5826**, 371(2005)

Tigau, N.; Ciupina, V.; Prodan, G., Journal of Crystal Growth **277**, 529 (2005)

R. J. Swanepoel, Phys. E: Sci. Instrum. **16**, 1214 (1983).

D. E. Aspnes, “The Accurate Determination of Optical Properties by Ellipsometry,” in *Handbook of Optical Constants of Solids*, edited by Palik E D (Academic, Orlando, 1985), p.89.

E. A. Irene, Thin Solid Films **233**, 96 (1993).

R. J. Swanepoel, Phys. E: Sci. Instrum. **17**, 896 (1984).

E. Marquez, J.B. Ramirez-Malo., J. Fernandez-Pena, P.Villares, R . Jimenez-Garay, P.J.S. Ewen, and A.E. Owen, J. Non-Crystalline Solids **164-166**, 1223 (1993).

E. Marquez, J.B. Ramirez-Malo., J. Fernandez-Pena, P.Villares, R . Jimenez-Garay, P.J.S. Ewen, and A.E. Owen, Optical Materials **2**, 143 (1993).

R. M. A. Azzam and N. M. Bashara, “Ellipsometry and polarized light”(North-Holland Publsighing Co., 1977)

Hai Lu, William J. Schaff, Jeonghyun Hwang, Hong Wu, Goutam Koley, and Lester F. Eastman, Applied Physics Letters, Vol. 79, No. 10, pp. 1489–1491

F. Hamdani, A. E. Botchkarev, H. Tang, W. Kim, and H. Morkoc, Appl. Phys. Lett. **71** (21), 311.

Filmetrics Inc., San Diego, CA, USA, www.filmetrics.com.

J. M. Gonzalez-Leal, R. Prieto-Alcon, M. Stuchlik. M. Vlcek. S.R. Elliott, E. Marquez, Optical Materials **27**, 147 (2004).

TFCalc, software Spectra Inc., Portland, OR, USA (2003), www.sspectra.com

[1] Filmwizard, Scientific Computing Inc., Encinitas, CA, USA, www.sci-soft.com

F. A. Jenkins and H. E. White, *Fundamentals of Optics* (McGraw-Hill, Auckland, 1981), p.482-6.

B. Titan, Appl. Opt. **23**, 4477-85 (1984).

A. R. Forouhi and I. Bloomer, Phys. Rev. B **34**, 7018 (1986).

N. W. Ashcroft and N. D. Mermin, "The Drude theory of Metals," in *Solid State Physics* (Saunders, Fort worth, 1976), p.16.

S. Cabuk and A. Mamedov, J. Opt. A: Pure Appl. Opt. **1**, 424 (1999).

C. Rincon, S. M. Wasim, and G. Marin, J. Phys.: Condens. Matter **14**, 997 (2002).

D. Brunner, H. Angerer, E. Bustarret, F. Freudenberg, R. Hopler, R. Dimitrov, O. Amvacher, and M. Stutzmann, J. Appl. Phys. **82**, 5090 (1997).

J. I. Pankove, *Optical Process in semiconductors* (Prentice- Hall, Elgewood Cliffs, NJ, 1971), Chap. 3.

R. Fletcher, and M. J. D. Powell, Computer J. **6**, 163 (1963).

D. Goldfarb, Mathematics of Computing, **24**, 23 (1970).

E. Marquez, J. B. Ramirez-Malo, P. Villares, R. Jimenez-Garay, and R. Swanepoel, Thin Solid Films **254**, 83 (1995).

J.B. Ramirez-Malo, E. Marquez, C. Corrales, J. Fernandez-Pena, J. Reyes, P. Villares, and R. Jimenez-Garay, Materials Chem. and Phys.s **44**, 186 (1996).

E. Marquez, J. M. Gonzalez-Leal, R. Jimenez-Garay, S. R. Lukic, and D.M. Perovic, J. Phys. D: Appl. Phys. **30**, 690 (1997).

E. Marquez, A.M. Bernal-Oliva, J.M Gonzalez-Leal, R. Prieto-Alcon, A. Ledesma, R. Jimenez-Garay, and I. Martil, Materials Chem. and Phys. **60**, 231 (1999).

M. McClain, A. Feldman, D. Kahaner, and X. Ying, Computers in Phys. **5**, 45 (1991).

Filmetrics Inc., San Diego, CA, USA, www.filmetrics.com.

R. D. Vispute, J. Narayan, H. Wu, and K. Jangannadham, J. Appl. Phys. **77**, 4724 (1995).

Chapter 4

S. Strite and H. Morkoc, J. Vac. Sci. Technol) **B10**, 1237 (1992).

H. Morkoc, S. Strite, G.B.Gao, M.E. Lin,B. Sverdlov and M. Burns, J. appl. Phys. **76**, 1363 (1994). And references therein.

R.F Davis, Porc. IEEE, 702, (1991).

M.T Duffy, C.C. Wang, G.D. O'Clock, Jr. S.H. MacFarlance III, and P.J. Zanzucchi, J. Electron. Mater **2**, 359 (1973).

L.M. sheppard, Am. Ceram. Soc. Bull. **71**, 1801 (1990).

T.Y. Sheng, Z.Q. Yu, and G.J. Collins, Appl. Phys. Lett. **52**, 576 (1988).

Y.X. Wang, Y.A. Li, and W. Feng W.Q. Lia, C.H. Zhao,L.H. Liu, K.C. Feng, Y.N. Zhao, Applied Surface Science **243**, 394-400 (2005).

P. Kung, A. Saxler, X. Zhang, D. Walker, T.C. wang,, I. Furguson, and M. Razeghi, Appl. Phys. Lett **66**, 2958 (1995).

K. S. Stevens, A. Ohtani, M. Kinniburgh, and R. Beresford, Appl. Phys. Lett. **65**, 321 (1994).

W. J. Meng, J. Heremans, and Y.T. Chang, Appl. Phys. Lett. **59**, 2097 (1991).

R. D. Vispute, J. Narayan, H. Wu, and K. Jangannadham, J. Appl. Phys. **77**, 4724 (1995).

G.K. Hubler, in *Pulsed Laser Deposition of Thin Films*, edited by D.B. Chrisey and G.K. Hubler (Wiley-interscience, New York, 1994), and references therein.

R.D Vispute, J. Narayan, Hong Wu and K. Jagannadham, J. Appl. Phys. **77**, 4724 (1995).

R.D Vispute, Hong Wu, and J. Narayan, Appl. Phys. Lett. **67**, 1549 (1995).

Ravi Bathe, R.D Vispute, Dan Habersat, R.P. Sharma, T. Venkatesan, C.J. Scozzie, Matt Ervin, B.R. Geil, A.J. Lelis, S.J. Dikshit, and R. Bhattacharya, Thin Solid Films **398-399**, 575 (2001).

J. Keckes, S Six, J.W. Gerlach, and B. Rauschenbach, Journal of Crystal Growth **262**, 119-23 (2004).

Carmen Ristoscu, Ion N. Mihailescu, Michalis Velegrakis, Maria Massaouti, Argyro Klini, and Costas Fotakis, Jounal of Applied Physics **4**, 2244-2250 (2003).

Eniko Gyorgy, Carmen Ristoscu, I. N. Mihailescua, Argyro Klini, N. Vainos, C. Fotakisc, C. Ghica, G. Schmerber, and J. Faerber, Jounal of Applied Physics **90**, 456-61 (2001).

H. Esrom, J. Y. Zhang, and A. J. Pedraza, Mater. Res. Soc. Symp. Proc. **236**, 383, (1992).

M. J. DeSilva, A. J. Pedraza, and D. H. Lowndes, J. Mater. Res. **9**, 1019 (1994).

S. Cao, A. J. Pedraza,, and L. F. Allard, J. Mater. Res. **10**, 54 (1995).

R.D. Vispute, V. Talyansky, R.P. Sharma, S. Choopun, M. Downers, T. Venkatesan, Y.X. Li, L.G. Salamanca-Riba, A.A. Iliadia, K.A. Jones, and J. McGarrity, Applied Surface Science **127-129**, 431 (1998).

S. Six, J.W. Gerlach, and B. Rauschenbach, Thin Solid Film **370**, 1-4 (2000).

M. Tabbal, P. Merel, M. Chaker, and H. Pepin, Eur. Phys. J. AP **14**, 115-9 (2001).

R. K. Singh, O. W. Holland, and J. Narayan, J. Appl. Phys. **68**, 233 (1990)

R. J. Swanepoel, *Phys. E: Sci. Instrum.* **17**, 896 (1984).

Jonghoon Baek, Desiderio Kovar, John W. Keto, and Michael F. Becker, Applied Optics **45**, 1627 (2006). .

Carmen Ristoscu, Ion N. Mihailescu, Michalis Velegrakis, Maria Massaouti, Argyro Klini, and Costas Fotakis, Jounal of Applied Physics **4**, 2244-2250 (2003).

Eniko Gyorgy, Carmen Ristoscu, I. N. Mihailescua, Argyro Klini, N. Vainos, C. Fotakisc, C. Ghica, G. Schmerber, and J. Faerber, J. OF Applied Physics **90**, 456-61 (2001).

H. Esrom, J. Y. Zhang, and A. J. Pedraza, Mater. Res. Soc. Symp. Proc., 236, 383, (1992).

S. Cao, A. J. Pedraza,, and L. F. Allard, J. Mater. Res. **10**, 54 (1995).

Edwards, Allen Louis, "Multiple regression and the analysis of variance and covariance"(San Francisco), (1979)

R.D Vispute, J. Narayan, Hong Wu and K. Jagannadham, J. Appl. Phys. **77**, 4724-28 (1995).

R.D Vispute, J. Narayan, J.D. Budai, Thin solid Films **299**, 94-103 (1997).

Cullity, B. D.; Stock, S. R."Elements of X-Ray Diffraction, 3rd Edition", (Prentice Hall, Upper Saddle River, N. J.) 664 (2001).

M. Tabbal, P. Merel, M. Chaker, and H. Pepin, Eur. Phys. J. AP **14**, 115 (2001).

P. Tyagi and A.G. Vedeshwara, Eur. Phys. J. AP **19**, 313 (2002) :

S. B. Ren, C. J. Lu, J. S. Liu, H. M. Shen, and Y. N. Wang, Physical review B **54**, 15 (1996).

Y. Sakashita and H. Segawa, J. Appl. Phys. **73**, 7857 (1993)

M. de Keijser, G.J.M. Dormens, P.J. VanVeldhoven, and D.M. de Leeuw, Appl. Phys. Lett. **59**, 3556 (1991)

W.Y, Chiu, C.H. Wu, H. L. Kao, and Erik S.jeng. J. Vac. Sci. Technol. A **20** 843(2002)

Li-peng wang, Dong S. Shim, Qing Ma, and valluri R. Rao. J. Vac. Sci. Technol. A **23** 1284 (2005)

W. J. Meng, in *Properties of Group III Nitrides*, edited by J. H. Edgar (INSPEC Short Run Press Ltd., London, 1994), pp. 22–34.

Han-Yong Joo, Hyeong Joon Kim, Sang Jung Kim, and Sang Youl Kim, J. Vac. Sci. Technol. A **17**, 862-70 (1999).

J.W. Lee, I. Radu, M.Alexe, Journal of Electronic materials **13**, 131 (2002),

J. Kolodzey, E. A. Chowdhury, G. Qui, and J. Olowolafe, Appl. Phys. Lett. **71**, 3802 (1997) ,

Ruifeng Yue, Yan Wang, Youxiang Wang, Chunhua Chen, Applied Surface Science **148**, 73–78 (1999)

Chowdhury, Enam Ahmed, Dashiell, M, Qiu, G, Olowolafe, J O, Journal of Electronic Materials **27,** 918 (1998)

Chapter 5

Ch. Bosshar, K. Sutter, Ph. Pretre, J. Hulliger, Florsheimer, P. Kaatz, P. Gunter, Organic Nonlinear Optical Materials, in: A.F. Gario (Ed.), Advances Nonlinear Optics, vol. 1, Gordon and Breach, New York, 1995.

H. Kalt, V.G. Lyssenko, R. Renner, C. Klingshirn, J. Opt. Soc. Am. B **2** , 1188. (1985)

R. Vijaya, Y.V.G.S. Murti, G. Sundararajan, T.A. Prasada Rao, Opt. Commun. **76**, 256. (1990)

N.Herron and D.L. Thorn. Adv. Mater. 10,1173 (1998)

David S. Stoker " Ultrafast third-harmonic generation from nanostuructured optical thin films and interfaces" (2006)

P. Roussgnol, D. Ricard, C. Flytzanis, Appl. Phys. B 437 (1990).

Nasu, Hiroyuki; Tanaka, Akimasa; Kamada, Kenji; Yamamoto, Yoshitsugu; Matsuzaki, Yasuhiro; Hashimoto, Tadanori. Journal of the Ceramic Society of Japan , **110,** 921 (2002)

Prakash, G. Vijaya; Cazzanelli, M.; Gaburro, Z.; Pavesi, L.; Iacona, F.; Priolo, Materials Research Society Symposium Proceedings, **722**, 219 (2002)

Yao, Weiguo; Shi, Wangzhou; Lin, Kuixun; Qi, Zhenzhong; He, Yizhen. Science in China, Series A: Mathematics, Physics, Astronomy, **39**, 991 (1996)

C. Bohren and D. Huffmann, *Absorption and Scattering of Light by Small Particles* (John Wiley, New-York, 1983).

W. T. Nichols, "Production and controlled collection of nanoparticles; toward manufacturing of nanostructured materials" Dissertation, The University of Texas at Austin (2002)

P. Scherrer. Gottinger Nachrichten (1918); cf. also. R.Zsigmondy, Kolloidchemie (3rd Ed, 1920), p. 394

G. Xu, M. Tazawa, P. Jin, S. Nakao and Yoshmura, Applied Physics Letters, 82, 3811 (2003)

Vita

Jonghoon Baek was born in Seoul, Korea on August 20, 1970, the son of Kyungsam Baek and Chohye Choi. In March 1990 he began his study of physics at Yonsei University. In February 1994, he graduated with a Bachelor of Science degree in Physics. He started his graduate study at Yonse National University, in March 1994 with his advisor professor Ung Kim and graduated with a Master of Science in February 1996. From February 1996 to August 2001 he worked for Korean Electric Power Corporation (KEPCO) where he has been engaged in the development of the over current protection relay by using bulk type and fiber type optical sensor. In August 2001 He entered the doctoral program in the department of Electrical and Computer Engineering at The University of Texas at Austin with his advisor professor Michael F. Becker.

Permanent address: Seocho-gu Seocho-dong 1444-7, GS Seocho Xi APT,
102-dong 1005-ho, Seoul , South Korea

This dissertation was typed by Jonghoon Baek